THE ROLE OF PARTICLE SIZE AND CONCENTRATION IN DEFINING THE FLOW STRUCTURE OF TURBIDITY CURRENTS AND THE MORPHOLOGY OF THEIR DEPOSITS: INSIGHTS FROM COMPUTED TOMOGRAPHY

Michael Christopher Tilston

A thesis submitted to the Faculty of Graduate and Postdoctoral Studies
in partial fulfillment of the requirements for the degree of

DOCTOR OF PHILOSOPHY

in Earth Sciences

University of Ottawa
Ottawa, Canada

April 2016

ABSTRACT

Turbidity currents are turbulent particle suspensions that are the primary mechanism for transporting terrestrial sediments to the deep marine, and generate some of the largest depositional features on Earth. However the fluid-particle interactions that sustain these currents are poorly understood, principally due to the technical challenges posed by obtaining accurate velocity and density measurements, which are critical for describing flow behavior and depositional characteristics. Numerous studies have bypassed these issues by using saline density currents, but this negates the ability to link flow processes with depositional features, and it is unclear whether their density structures are representative of particle gravity flows. Consequently, numerous questions remain over the flow conditions that build up a significant part of the deep-marine geologic record.

In this thesis I reports on the flow processes and depositional features of sediment-gravity currents across a broad range of particle sizes and concentrations. The technical challenges of obtaining reliable density data are overcome by running the experimental flows through a medical grade computed tomography (CT) scanner, and pair this data with three-dimensional velocity measurements using an ultrasonic Doppler velocity profiler (UDVP-3D) to get one of the first glimpses of the internal structure of turbidity currents. Unlike previous studies where flow processes are described in terms of the velocity field, this thesis demonstrates that fluid-particle interactions are controlled by momentum characteristics, and that the velocity field is determined largely by the current’s density structure. Moreover, the density structure also exerts a first order control on the morphology of their deposits.

ACKNOWLEDGEMENTS

Invariably this list will be incomplete as I've been lucky enough to have a wide range of people that are wholly responsible for this entire adventure, from those that initially encouraged me down this road (I won't hold it against you), to the support along the way (to whom I can never express the depth of my gratitude), to those that gave this work the final "thumbs up" (I could kiss you). I'm sure I'll forget some names along the way, but I figure if you've spoken to me over the years you hopefully know me well enough to know I'll probably feel more embarrassed over the omission than you'll be upset.

As for the proverbial "kick off the ledge" that got this project going, I'd like to that my undergraduate and master's advisor, Prof. Pascale Biron, where despite having been out of academia for a few years working at a consulting gig, kept her eye out and notified me when this opportunity first started circulating through the academic avenues. I'd also like to thank my family for being so supportive of this whole endeavor, specifically my mother, Jacquelyn, and my sister, Megan, and my uncle's Steve and Dave for all there encouragement along the way whenever things hit a rough patch.

In terms of bringing me onboard for this project on the flow mechanics of experimental turbidity currents, for their eternal patience and the plethora of insightful conversations over the years that have proved crucial in molding our collective understanding of these unique geophysical flows, I'm forever indebted to you Prof.'s Bill Arnott and Colin Rennie - like it or not you're probably stuck with me for many years to come, and I'm certainly looking forward to continuing these conversations over the years; you've both been wonderful mentors. I would also like to thank all the members of the Windermere consortium that provided the funding to make this research possible along with all the past and present students that have been part of the research group over the years for the spirited conversations over the years. Specifically, Dr. Viktor Terlaky for the late night conversations over everything from science, to art and music, but also serving as a mutual crutch for the inevitable personal hardships that come up over the length of time we have known each other. Of course there is another unsung hero in all this, the late Prof. Bernard Long at the Institut National de la Recherche Scientifique (INRS) in Québec City; I seriously doubt there was anyone else on the planet crazy enough to let us run these currents through a medical grade CT scanner. You will be missed.

Aside from all support staff at University of Ottawa and the dear friends I`ve made during my tenure in Ottawa (I`m looking at you Jeff Fennel and Matt Sympson), I would like to thank the reviewers of this thesis, Prof.’s Glen Cummings, Ioan Nistor, Glenn Milne and Sean Bennett. All of your insightful comments have invariably made the final version of this manuscript far more coherent than it would have otherwise been.

DEDICATION

I was debating about whether to create this section, but I figured that between the number of people which might actually read this, it can't hurt...beside, it might help shed some light on the reasons why I found myself on this (admittedly) long journey. A certain person deeply involved in seeing this project through has a quote posted above his desk by Calvin Coolidge that said "Nothing in the world can take the place of persistence. Talent will not; nothing is more common than unsuccessful men with talent. Genius will not; unrewarded genius is almost a proverb. Education will not; the world is full of educated derelicts. Persistence and determination alone are omnipotent". I can't help but wonder whether he regrets pointing this out to me after all these years, and while the sentiment sums it up nicely, the duration of this degree cannot be attributed to that one quote. After all, and unbeknownst to him at the time, I am the byproduct of two people who are, by all accounts, the most stubborn people to have walked the planet; they would probably deny this vehemently …but deep down, they'd have to concede it's true.

So this one's for the folks, but more so for my Dad; the parallels in our academic trajectories is uncanny, which has led to my Mom consistently saying "you are your Father's son"… I'm still not sure if that's one of her loving back-handed compliments (always said with a genuine smile – "no sass" means "no love"), but allow me to elaborate. After his first year in engineering at University of Toronto, my dad got the boot due to poor grades and was told to never come back. At the time he was sitting around with a high-school friend, trying to figure out how to make a living. Together they decided to skip the academic route, and his friend came up with the most brilliant way to make bank: move to the parries to work deep underground in the coal mines. They went through the job application process, to which "friend" failed and Dad passed, so off he went alone. The problem was Dad was broke, and being deep underground necessitates (though not required by the company at the time) proper dress, which resulted in him quickly developing pneumonia. So the story goes he had to leave the deep, dank coal-mines in Thompson, Manitoba, and return to southern-Ontario where his dad (who had a Ph.D. in Applied Mathematics from U of T) promptly marched him back to the university and demanded they let him back in; they did and he went on to get his Ph.D. in Electrical Engineering from the same institution. That's how my sister and I had the luck of growing up on the corner of a highly subsidized residence unit on the corner of Young and Bloor in downtown Toronto, surrounded by families that also followed the academic route.

With that in mind, I can't help but chuckle about how surreal it must have been for him when I got the boot from the Physics department from Concordia University after my first year, and after an equally disastrous summer, he found himself walking me back to the department and demanding that I was let back in just as his Dad did for him. Much like him, I now also find myself submitting my own doctorate, although a few decades later. Sadly, his Dad viewed him getting his doctorate as some form of questioning parental dominance, but mine did not... His last coherent words to me before succumbing to brain cancer just two months prior to starting this adventure were: "Did you get in?" I can still remember hearing the sigh of relief and pride over the phone when I said "Yup".

So there's a secluded nook in Ruckle Park on Salt Spring Island (British Columbia) where the waves crash onto the shore, and in that nook there's a lonely bench overlooking the ocean with a plaque that reads "Mark – Your quirky grin, red wine, quiet chuckle. Forever make us smile". As much as I'm looking forward to going to the Netherlands, I hope I get a chance to sit on that bench with you for a bit, and tell you "I did it, and I did it the way you told me to –never compromise your work for the sake of getting it done, and if it ain't worth doing right, it ain't worth doing at all… I think I did it right, and I think you'd be proud". It's comforting to think that as I'm lacing up your beat-up old hiking boots for this new adventure, in some way you'll still be with me. XO

TABLE OF CONTENTS

LIST OF FIGURES

LIST OF TABLES

CHAPTER 1

1.1. **Introduction**

The processes governing the entrainment, transport and deposition of sediments are key tenants underpinning our ability to interpreting the Earth's present morphology, its geologic record and predict its evolution. Indeed these basic relationships are so universal that they are now being widely applied to interpret the history of our nearest celestial neighbors (Burr et al., 2015), and while there is definite appeal in applying these simple principles to explain morphologic processes on other planets, it is easy to forget an equally unexplored region located much closer to home: the ocean floor.

Covering approximately 60% of the earth's surface, deep marine environments represent one of the most poorly understood systems in earth sciences, and up until the beginning of the 20th century was widely regarded as a passive system where sedimentation was dominated by the gentle settling of mud. But this view was literally shook up in 1929 when an earthquake hit the Grand Banks off the southwestern coast of Newfoundland, Canada. Here, trans-Atlantic telegraph cables went dead in a sequential order shortly thereafter, giving us the first indication that the ocean floor was anything but a passive system. Through a numerical reconstruction Piper et al. (1999) deduced that the breakages in the submarine cables were the result of a massive geophysical flow event: a turbidity current. Subsequently, deep marine environments have become the subject of major research initiatives by geomorphologists and sedimentary geologists alike.

Commonly originating on the upper part of the continental slope, these flows can be triggered by diverse means, from extreme events like earthquake induced slope failures, to direct suspended sediment input from flooding rivers and littoral transport systems (e.g. Droz et al., 1996), and once initiated form turbulent particle suspensions that are the primary vehicle for transporting sediments to the ocean floor (Khripounoff et al., 2003). Importantly, turbidity currents differ from most other geophysical flows by gravity acting directly on suspended solids that then entrain neutrally buoyant ambient fluid, which forms the passive component of the flow. These currents then accelerate down slope before reaching the basin floor, where they can continue to run under their own momentum for thousands of kilometers before eventually coming to rest (e.g. Middleton, 1993) (Figure 1-1). As such, there are two end-member states to describe the life-cycle of turbidity currents: 1) gravity driven, where flow is accelerating and deposition is nominal, and 2) momentum driven, where flow energy wanes and deposition is substantial. The latter of the two flow states obviously makes the most voluminous contribution to the geologic record.

The deposits from these flows build up a variety of stratal elements that collectively form geomorphic features termed submarine fans (Terlaky et al., 2016), which represent the largest depositional features on the planet (Curray et al., 2002). From a morphodynamics perspective then, turbidity currents are the largest sediment transporting agents on the planet. For example it has been estimated that a single flow event, typically lasting from a matter of hours to days, can transport more sediment that the net annual flux of all the worlds rivers combined (Talling et al., 2007). While the fluid-particle processes controlling these flows and their related deposits are of great importance to the petroleum industry, they may have even greater ramification for the Earth's climate. For example the Bengal fan, which is the largest active modern submarine fan system, is estimated to capture10-20% of the total annual organic carbon that becomes buried in oceanic sediment (Galy et al., 2007). Therefore we can safely conclude that turbidity currents are not only one of the major agents driving the morphology of the planet, but also controlling its climate. Consequently, there is a strong need to develop conceptual models to describe the behavior of these systems that, for numerous reasons, has remained elusive.

Due to the extreme nature of deep marine environments, *in situ* study is challenging at best, and more often than not, financially and technologically prohibitive. As a result most of our understanding of deep oceanic sedimentary systems has been derived from seismic imaging and observations in the ancient sedimentary record. It has become known that the planform and cross-sectional characteristics of many of the depositional elements seen on the ocean floor are similar to those in terrestrial fluvial systems (Klaucke & Hesse, 1996). For example, channel geometries in these environments can be broadly classified as straight, meandering and braided patterns, much like fluvial systems (Hagen et al., 1994), and show evidence of similar processes at the macro (e.g. bend cut-offs (Kolla, 2007)), meso (e.g. point bars (Arnott, 2007)) and micro (bedform (Bouma, 1962) scales. These similarities are especially noticeable in the proximal zone of turbidite systems where, much like fluvial systems, channels are deeply incised (Peakall et al.,

2000) and as a result, Leeder (1999) concluded that fluvial systems serve as good analogues for processes operating in turbidity currents. However it has been suggested more recently that there are in fact some fundamental differences between fluvial and sub-marine systems, and therefore the notion of dynamic similarity is a source of ongoing debate.

For a physical model to accurately demonstrate linkages between flow structure and bed morphology, it must meet two criteria: 1) the excess density must be derived from suspended solids; 2) both velocity and density fields must be sampled as the product of the two (momentum) defines the flow structure. Unfortunately meeting these two criteria, specifically measuring the density characteristics of particle gravity currents, is exceedingly difficult using conventional instrumentation. Most sampling devices rely on acoustic or optic backscatter to measure these parameters, where suspended solids act as the reflection media for the emitted wave (e.g. Pinkel, 1980). Note that these kinds of analyses require calibration, which may introduce a source of error in the accuracy of the end value. Moreover at high particle concentrations, like those in turbidity currents, the signal is attenuated preventing their velocity and density structure, the exact threshold being dependent on the ratio between the wavelength of the acoustic pulse to the particle diameter (e.g., Urick, 1948). To circumvent these problems many researchers have relied on saline generated density currents (e.g. Britter & Linden, 1980), and justified their use on scaling arguments (Peakall et al., 1996). However it is unclear how well the density structure can be mimicked by a saline solution, nor is it possible to investigate the links between flow structure and channel or bed morphology.

In the present work it is hypothesized that instead of the conventional view where flow structure is defined by the velocity field, it is density structure that acts as a first order control on flow characteristics and deposit morphology -- density structure being a byproduct of particle size and concentration. Consequently, we begin by reviewing the links between turbulent boundary layers, specifically wall-bounded shear flows, in relation to sediment transport and bedform development and speculate on how these relations might change in the presence of high suspended sediment loads. This is followed by a brief literature review of the velocity and density structure of turbidity currents, and ends with the thesis objectives.

1.2. **Turbulent boundary layers, sediment transport and bedform development**

Since the seminal observations of Reynolds (1883) on the behavior of incompressible, viscous fluids, it is widely accepted that they are characterized by two distinct states: laminar, where the fluid acts like a series of thin, non-interactive layers, and turbulent, where substantial mixing occurs across the layers. In searching for a mechanism to explain this phenomenon, Reynolds (1895) began simplifying the Navier-Stokes equations and demonstrated that flow state is determined by the ratio of fluid momentum to viscosity, as defined by the Reynolds number (Re)

$$Re = \rho \frac{\bar{u}\delta}{\mu} \ , \qquad 1.1$$

where ρ, $\bar{u}$, δ and μ are the density, mean velocity, thickness and dynamic viscosity of the fluid. It's important to note that this is a simplified, depth-averaged parameter, and the true source of mixing, and therefore production of turbulent motion is, in fact, the strength of fluid shear, defined by the momentum gradient ($\partial p/\partial z$, or $\partial(\rho\bar{u})/\partial z$) (Nezu & Nakagawa, 1993).

During the intervening years, our view on turbulence has been progressively refined. Initially thought of as a disorganized, stochastic process, it was first noticed that the near-boundary region, where shear is the highest, was actually characterized by a series of coherent, organized fluid motions associated with the development of hairpin vortices (Kline et al., 1967). Here, the leading loop of the hairpin is uplifted, moving low velocity fluid away from the bed, and due to continuity, replaced by an inrush of faster overlying fluid, which represents the physical manifestation of the Reynolds stress (Figure 1-2). This analysis is conducted using Reynolds decomposition, which assumes that the velocity at any given time (t) can be divided into time-averaged ($\bar{u}$) and fluctuating ($u'(t)$) parts

$$u(t) = \bar{u} + u'(t), \qquad w(t) = \bar{w} + w'(t) \qquad 1.2$$

where u and w are the components of the flow acting parallel (positive downstream) and parallel (positive away from the bed), respectively. Accordingly, the Reynolds stress ($\tau = -\rho \cdot u' \cdot w'$) is the product of downstream (u') and vertically (w') oriented velocity fluctuations. The aforementioned hairpin uplift ($u' < 0, w' > 0$) and ensuing high speed inrush ($u' > 0, w' < 0$), referred to as bursts and sweeps respectively, make positive contributions to the Reynolds stress and turbulent mixing in an attempt to minimize fluid shear. Importantly, Reynolds never explicitly referred to $u'(t)$ as being associated with turbulence, perhaps recognizing that discharges fluctuate over time. The astute reader will recognize that the above decomposition is certainly not a useful datum for unsteady surge-like flows like turbidity currents, a point discussed at length in **Chapter 2**.

The discovery of hairpin vortices was followed in quick succession by two other key studies on fluid-boundary interactions. First, while studying the effects of boundary characteristics on turbulence properties, Grass (1971) discovered that increasing the bed's hydraulic roughness, the drag exerted on the flow by progressively larger particles to the bed, caused an associated increase in the intensities of w' and τ, which, respectively, are responsible for suspended and bedload transport, and therein the ability of particle resistance to modify flow structure. During the same year while studying the initiation of ripples from a flat bed, Williams and Kemp (1971) showed that under incipient transport conditions, the elevated bed stresses linked with the high speed inrush of fluid following hairpin uplift described by Kline et al. (1967) were sufficient to cause spatially and temporally localized particle motion, and that the ensuing depositional mound was the precursor to ripple formation; this established the link between turbulent motions, sediment transport and bedform development.

Since then, it now seems that turbulence should be viewed at a continuum of coherent fluid motions occurring over a broad range of spatial scales (e.g. Falco, 1977) and, if we accept the energy cascade theory (Kolmogorov, 1991), then the largest structures are the most important as they contain the most energy, and transfer their energy to progressively smaller structures before eventually being dissipated by viscosity (Robinson, 1991). This in turn modifies the spatial distribution of shear stress on the bed, which alters local sediment transport rates allowing for the development of angular bedforms like ripples (Best, 1992) and dunes (Bennett & Best, 1995) that further organize the near-bed turbulent boundary layer characteristics. Concurrently, it has also been recognized that sediment transport rates are not just determined by the ratio of boundary to critical shear stress, but also the duration of excess shear forces (Diplas et al., 2008), which is ultimately dictated by the size of the passing turbulent structure (Figure 1-3). This highlights the need to properly characterize and subsequently isolate individual coherent fluid structures to accurately describe fluid-particle interactions.

While there are still some unknowns regarding fluid-boundary interactions in wall bounded shear flows, specifically the source of coherent fluid structures much larger than those associated with turbulence (Marusic et al. (2010), Figure 1-4) and whether they are linked to macro-scale morphologic features like meander wavelength (Marquis & Roy, 2011), a synthesis of the above observations has led to a highly detailed conceptual model describing the feedbacks between turbulent boundary layers, sediment transport and bedform development (Best, 1993) (Figure 1-5). Indeed, similar large scale coherent structures have been observed in natural particle gravity currents (Best et al., 2005), and so like open channel flow where the velocity profile increases logarithmically from the near-bed region (Hosseini et al., 2006), the resulting morphologies should also be similar.

Despite these similarities, these there are some noticeable differences between the flow structure of rivers and turbidity currents (Figure 1-5). As will be discussed in the following section, turbidity currents are marked by a longitudinal and vertical anatomy that is quite different from open channel flows. Second, they possess substantially higher particle concentrations, and the manner in which they are distributed vertically through the flow suggest that gravitational forces do not act uniformly through the water-column. Third is the apparent paradox between the need of suspended sediment to generate turbidity currents and the damping effect this sediment has on turbulence that keep these sediments aloft (Baas & Best, 2002). Linked with turbulence suppression is the issue of capacity verses competency driven deposition. In the case of competency related deposition, where there is sufficient shear to transport the sediment (Komar, 1970), it is reasonable to expect tractive structures similar to those seen in rivers. However the mechanisms associated with capacity related deposition beyond Bagnold (1956) concentration criterion remain poorly understood.

1.3. **Turbidity Currents: Flow Structure**

Compared to open channels, the flow structure of turbidity currents is fundamentally different for two basic reasons. As opposed to the relatively continuous and quasi-steady flows of fluvial systems, turbidity currents are highly episodic and display surge-like flow characteristics, and therefore have a distinct longitudinal anatomy (McCaffrey et al., 2003). Second, the low density contrast between the current and ambient fluid means that in addition to bed resistance, they also experience substantial resistance along their upper interface from the ubiquitous chain of Kelvin-Helmholtz instabilities that results in extensive mixing with the ambient fluid (Middleton 1966b).

The longitudinal structure of a turbidity current, as viewed from the side as the current passes by, is composed of three discrete parts: head, body and tail (Figure 1-6). The head is defined as a thick zone between the arrival of the current nose and the point where flow thickness begins to equilibrate. Ambient fluid displacement and therefore resistance is maximum at the nose and then decreases rearward, which leads to rearward acceleration of the head. Due to instrumental limitations, the earliest work on turbidity currents focused on the behavior of the head, and while measurements were crude, Middleton (1966) demonstrated that its velocity can be effectively approximated by

$$u = 0.75 \cdot \sqrt{|(\Delta\rho/\rho)g\delta|} \qquad 1.3$$

where $\Delta\rho$ is the density difference between the current and the overlying ambient fluid. It should be noted that current thickness (δ) is defined by the visible trace between the current and the ambient fluid, and will be defined in a more objective manner in the ensuing discussion on the vertical structure of turbidity currents. Intriguingly, this formula, which is reliable on slopes up to 4% (Middleton, 1966) lacks a slope parameter in the derivation, suggesting that the forward motion may be propelled by internal normal forces associated with gravitational settling rather than gravity pulling the fluid down the slope like in open channel flow.

More revealing, in terms of flow dynamics of the head, were the results from the high-speed photography analysis. Here, Middleton (1966) showed compelling evidence that flow in the head, at least in the region above the nose, is characterized by a distinctive upward motion due to shearing with the ambient fluid. This results in sediment being lofted upward and rearward, causing the head to thicken, a process that is also is enhanced by ambient fluid mixing (Allen, 1971; Britter & Linden, 1980).

Owing to the unsteadiness and relatively short duration of the head, most quantitative work subsequent to (Middleton, 1966) focused on the turbidity current body, which is quasi-steady and therefore allows for more sustained sampling. In the context of developing flow-morphology relationships, this is the most important portion of the current as it represents the majority of the current's longitudinal anatomy, so the deposition from the head, where stresses are generally higher (Cantero et al., 2008; Kneller et al., 1997), are negligible. In general, the flow structure of turbidity currents is split vertically into two zones based on the primary source of flow resistance, the (lower) inner and the (upper) outer regions separated by the velocity maxima (u_{max}). In keeping with the terminology used to describe wall-bounded jet flows (Launder & Rodi, 1983), current thickness (δ) as used here is defined as the height above the bed within the outer region where $u(z) = 0.5 \cdot u_{max}$, and the height of the velocity maxima above the bed is typically $z(u_{max}) \sim 0.2 \cdot \delta$ (Kneller et al., 1999). In terms of the relationship between near-bed velocity structure and bedform development, Hosseini et al. (2006) ran a series of particle driven density currents and found that the inner region displays a logarithmic velocity profile and, recalling that turbidity currents can be hundreds of meters thick (e.g. Gordon et al., 2009), suggests that the lower 10 m of the flow should behave much like an open channel flow, and therefore fluvial models linking flow structure and bed response should be valid.

More recently Sequeiros et al. (2010) generated a series of saline and particle driven density currents using low-density plastic beads to investigate the effects of flow criticality on flow structure, and found a distinct Froude number (Fr) control. This parameter defines the ratio of flow inertia to gravitational forces, and is defined as

$$Fr = u/\sqrt{g'\delta} \qquad 1.4$$

where $g' = g\,(\Delta\rho)/\rho$ is the reduced gravity related to buoyancy effects between the current and the ambient fluid. In supercritical flow ($Fr > 1$), the position of $z(u_{max})$ is in agreement with previous work in both the saline and particle runs, yet in the subcritical currents ($Fr < 1$), $z(u_{max})$ was $\sim 0.7 \cdot \delta$ and $\sim 0.4 \cdot \delta$ for the particle and saline runs, respectively. The reason for this was related to the Froude-Richardson (Ri) number relation ($Ri = 1/Fr^2$), which will be elaborated on in the following section. Importantly, the values of g' are approximately an order of magnitude less than open channel flow, which allows supercritical conditions to exist at substantially lower values of u and attendant shear. Consequently, because shear is required to maintain sediment suspension, it is not clear whether subcritical conditions can be achieved in natural turbidity currents where suspended particles are denser (e.g., $2650\ kg/m^3$ for quartz sand) than those used in the above experiments (1530 kg/m^3 for plastic beads), or if subcritical flows are largely an artifact of laboratory scaling parameters.

Not discussed by Sequeiros et al. (2010), however, it the significance of this finding. The higher position of u_{max} indicates not only a reduction in bed resistance (i.e. shear), but also reduced resistance from, and therefore mixing with, the surrounding ambient fluid. Since flow resistance and mixing is equated with energy loss, then the bedward depression of u_{max} for saline currents results from larger Kelvin-Helmholtz instabilities and presumably also would yield shorter run-out distances. This, then, suggests criticality and energy loss are intimately related, but it is important to note that these findings consider only the current's velocity structure. However since natural turbidity currents are driven by gravity acting on suspended particles, it would seem intuitive that the distribution of those particles might also need to be considered – in fact it is shown below that it is the density structure that controls the velocity field.

1.4. **Turbidity Currents: Density Structure**

Compared to the velocity structure, reports on their density structures are rare and have relied mostly on the use of salinity-generated density currents (e.g. Kneller et al. (1997)). While it can be argued that this is justified on the basis of scaling arguments, where the (reduced) size of the particles needed to match the reduced size of the experimental flow with respect to those in a natural turbidity current (see sclaing discussion in Kneller and Buckee (2000)), the argument suffers on two fronts. First, the assumption that the suspension dynamics and density structure of flows driven by suspended solids, which that are prone to particle settling and particle-to-particle interactions, can be accurately represented by a saline solution is a matter of debate (see discussion in **Chapter 3** and **Chapter 4**). Second, it precludes the ability to link flow processes with depositional features, which does little to help with interpreting the stratigraphic record. However, there is an overwhelming amount of theoretical evidence (e.g., Venditti et al., 2006) to suggest that density structure effects may serve to explain not just the differences in architecture of some meso- and macro-scale morphological elements in sub-marine and fluvial systems, but also the apparent grain size control on the run-out distance of turbidity currents.

In terms of the variations in levee height, or the vertical extent of lateral confinement between turbidity currents and open channel flows, consider how flow thickness is affected by stratification stability between the current and the overlying ambient fluid. The stability at the interface of the two fluids is controlled by the ratio of buoyancy, which provides resistance to mixing, to turbulent shearing forces, which promote mixing, as defined by the Richardson gradient number (Ri)

$$Ri = -\frac{g'}{\rho} \cdot \frac{\partial\rho/\partial z}{(\partial u/\partial z)^2} \qquad 1.5$$

where ρ is the density, u is the velocity and $g' = g\,(\rho_1 - \rho_2)/\rho$ is the reduced gravity. Here, the flow is unstably stratified and turbulent mixing dominates the flow field when $Ri < \sim 0.25$, whereas stable stratification occurs when Ri is equal or greater than unity. Therefore in two non-stratified fluids of greatly different densities, the individual fluids would experience internal turbulent mixing ($\partial\rho/\partial z = 0$), but the interface would remain stable, with the "fixed lid" allowing them to behave as two independent fluids; this is the case for open channel flows. Now consider the case of turbidity current where the bulk density is very close to that of the ambient fluid. The interface between the two is highly unstable, allowing for free exchange of mass and energy between the two fluids. Therefore the variations in levee height between fluvial and submarine systems may simply result from sediments being lofted higher into the water column in the latter due to the instability of the interface.

Crucially, the above description on stratification stability is based on bulk density parameters that, by definition, assume the two fluids are uniform in density. Yet since the early work of García (1993) on the differences in velocity and density structure of saline currents on sloped and horizontal surfaces it has been established that concentration profiles are bound by two end-member states: those with densities that decrease exponentially away from the bed, and those with "plug-like" densities that remain uniform up to u_{max}, above which lies a sharp density gradient that quickly equilibrates with the ambient fluid on the horizontal surface (Figure 1-7). This is an important distinction since, according to Equation 1.3, energy loss through the entrainment of non-energetic ambient fluid is minimized in plug-like density structures, which should translate to longer run-out distances. Yet the transition from exponential to plug like density structures under reduced slopes appears counterintuitive for turbulent particle suspensions since flow deceleration, and therefore reduced shear and suspension potential and higher particle settling, should produce the opposite result.

To address variations in density stratification characteristics, Sequeiros (2012) ran a series of experimental saline currents over a fixed slope, and reproduced the same variations in density structure reported in García (1993) by reducing current discharge, the transition from exponential to plug-like density structures being linked with waning flow energy. They found that exponential and plug-like density profiles are associated with super- and subcritical flow, respectively. An analysis of the Richardson gradient number was used to show that subcritical flows had a stable upper boundary, which minimizes ambient fluid entrainment and current dilution, below which turbulent mixing allows for the development of a homogeneous density structure. This stable interface, or “lid”, is absent in the supercritical flows, allowing for the development of large Kelvin-Helmholtz instabilities with higher rates of ambient fluid entrainment and hence rapid dilution away from the bed. While the analysis and interpretation is scientifically sound, it begs the question of whether their findings are an artifact of using saline density solutions rather than sediment-propelled flows.

Many studies illustrate that particle gravity currents have a tendency to develop an exponential rather than plug-like density structure (Best, 2005; Cartigny et al., 2013; Felix, 2002; Sequeiros et al., 2009; Sequeiros et al., 2010). However, Baas et al. (2004) were able to induce a similar transition from a plug to an exponential density structure by decreasing particle concentration, and therefore flow energy. While no indication of flow criticality was provided, if we can accept that increased mass should translate to higher Froude numbers, then the transition from plug-like to exponential density profiles with waning flow conditions is opposite to the behavior exhibited by saline driven density currents. Instead, it suggests that the density stratification characteristics of particle gravity currents are more appropriately related to a Rousse rather than a Froude number criterion. According to the Rouse (R_o) criterion, the density stratification characteristics of particle suspensions are defined by the ratio of particle settling velocity (w_s) to turbulent suspension potential

$$R_o = w_s/\beta\kappa u_* \qquad 1.6$$

where $\beta \approx 1$ defines the coefficient between turbulence production and dissipation, κ is the von Karmen's constant (0.41), u_* is the shear velocity (e.g. Geyer, 1993) and w_s can be defined by the equation

$$w_s = \frac{g'd^2}{C_1\nu + (0.75C_2g'd^3)^{0.5}} \quad 1.7$$

where d is the particle diameter, ν is the kinematic viscosity of the fluid, C_1 is a theoretical constant with a value of 18, and C_2 is the constant asymptotic value of the drag coefficient ($C_D = 4g'\mathrm{d}/3{w_s}^2$) for $10^3 < Re < 10^5$, which numerous experiments have shown to result in $C_2 \approx 0.4$ and $C_2 \approx 1$ for smooth spheres and natural grains, respectively (see Ferguson and Church (2004) and associated references for further details). Noting that u_* is a depth averaged term use to describe shear stress ($\tau = \rho u_*^2$), one can easily derive local values of u_* by using the equation

$$u_* = \kappa\delta\, \partial u/\partial z \quad 1.8$$

to determine the Rouse parameter. Current density at a given height above the bed ($C(z)$) can be modelled in the following

$$C(z) = C_{\mathrm{ref}}\left(\frac{(\delta - z)z_{\mathrm{ref}}}{z(\delta - z_{\mathrm{ref}})}\right)^{R_o} \quad 1.9$$

where the subscripts denote a given reference height. However, I am unaware of any studies having applied the above to a particle rather than a fluid driven gravity flow and so this warrants further investigation. A remarkably similar parameter was derived by Leeder et al. (2005) to determine the conditions for the auto-suspension of particle gravity current, the criterion (Λ) for which is

$$\Lambda = \frac{\rho_f\left(\overline{u'^2_z}\right)_{max}}{m\left(\Delta\rho_{s-f}/\rho_s\right)g} > 1 \quad 1.10$$

where ρ_s is the density of the suspended solids and the term $\Delta\rho_{s-f}$ is the density difference between the suspended solids and the fluid, as denoted by the subscripts. However I cannot find examples of techniques for predicting density structure of turbidity currents in the literature.

1.5. **Thesis Novelty and Objectives**

The general hypothesis of this thesis is that a current's density structure exerts a first order control on the flow structure and depositional response of turbidity currents, which has proven a difficult question to address using experimental particle gravity currents. Admittedly this is a very broad question and coming up with a unified answer is more in keeping with an entire research career rather than a Ph.D. thesis. Nonetheless, here I attempt to take the first, preliminary steps in addressing this question by focusing on three key issues: 1) how to predict the density stratification characteristics of turbidity currents; 2) what are the effects of density stratification characteristics on bed response; 3) how does density stratification affect overall flow structure. The ability to address these questions in this thesis was made possible by the use of a medical grade CT scanner to accurately measure the three-dimensional density structure while simultaneously capturing velocity data (UDV-3D) in particle driven turbidity currents, thereby allowing for the first glimpses of their internal momentum structure.

I begin to address the first question in **Chapter 2**, working under the assumption that turbulent velocity fluctuations are responsible for driving sediment suspension. If this is the case, then it raises the question of how to identify turbulence in highly unsteady, surge-like flows? The central challenge here relates to the lack of a rigorous methodology for differentiating time-series velocity data for unsteady flows, where standard Reynolds decomposition (Reynolds, 1895) is inappropriate. The conventional solution is to use a combination of spectral analysis and frequency filtering. The premise is that turbulent flows are composed of a series of coherent fluid structures operating over a range of temporally and spatially dependent scales that can be identified through spectral analysis, a technique that decomposes the net velocity fluctuations on the basis of frequency (Figure 1-8). Smaller, spatially dependent scales of motion constitute fluid turbulence, and can be identified using the energy cascade theory, where energy is transferred from larger to progressively smaller coherent motions following a $-5/3$ slope before eventually being converted into heat (Kolmogorov, 1991). Once the frequency associated with the largest turbulent motions is identified, a low-pass filter can be applied to identify the non-turbulent term in Equation 1.2 to isolate turbulence. This technique has been widely applied in oceanographic studies where turbulent motions can be masked by wave action (e.g., Lumley & Terray, 1983). However, these "non-turbulent" motions are highly periodic, whereas the "non-turbulent" component in turbidity currents can be aperiodic, which poses a unique challenge. Recalling that the start of the energy cascade is defined by a spatially dependent scale, and the velocity measurements consist of temporal data, the aim is covert from the time to the space domain using a convection velocity (u_c). The only defined technique of achieving this is to invoke Taylor's frozen turbulence hypothesis (Taylor, 1938), which assumes that the convection velocity is equivalent to $\bar{u}$, which cannot be equated to u_c in unsteady flows.

In this chapter, we propose a technique using the continuous wavelet transform (CWT) to determine u_c for all each instantaneous velocity measurement, thus allowing us to convert eddies from the time to space domain, and subsequently de-couple turbulent and non-turbulent fluid motions; this is a fundamental precursory step to investigating the role of turbulence on defining the density structure of turbidity currents. Unlike most spectral analysis work, the CWT provides instantaneous rather than time-averaged spectra as in Figure 1-8. When interpreting the CWT figures in this chapter, it is important to recognize that the shape of the spectra in Figure 1-8 is now represented by colour (e.g., Figure 2-7). In this article, my contribution consisted of identifying the difficulties of identifying turbulence in unsteady flows. Professor Arnott and myself jointly performed the experimental work, though I was solely responsible developing the code to convert time-series data into a pseudo-spatial framework, and performing the sensitivity analysis to confirm that this technique is equivalent to Taylor's original hypothesis, but can also account for time-frequency variations in convection velocity (u_c). I was also the sole author in writing the accompanying text, with my advisors acting as content reviewers.

Knowing that certain aspects of flow structure and ultimately run-out distance are affected by boundary resistance, I begin to address this issue in **Chapter 3** by focusing on the bed. As previously mentioned, it has been recognized that angular bedforms, specifically dunes, and to a lesser degree ripples, are on average noticeably absent in turbidites versus fluvial deposits. Explaining these differences is compounded by the fact that there are two competing theories for the mechanisms leading to ripple formation, one rooted in turbulence (Williams & Kemp, 1971) and the other in the development of hydrodynamic instabilities from near-bed density gradients (Venditti et al., 2006) (Figure 1-9). Here, the objective is to run a series of experimental currents and observe the response of the bed; density structure is modulated by altering the grain size and sediment concentration of the initial slurries that form the experimental currents. These observations are used to determine if bed response is controlled by turbulent or density stratification related processes, and if the latter is the dominant mechanism, then what grain sizes and concentrations are associated with the development of angular bedforms. This chapter is published in Geology (Tilston et al., 2015) and a copy of the article is provided in **Appendix A**. In this article, both Professor Arnott and I collaborated in measuring the experimental currents and observing the correlation between particle size and concentration with bed response. We also jointly postulated that bed response was related to the presence/absence of hydro-dynamic instabilities resulting from near-bed density stratification characteristics. However, I was the only person involved in the coding to process the CT data, developing the techniques for removing image artifacts, and writing the manuscript.

Finally in **Chapter 4** we investigate the flow dynamics of turbidity currents themselves. Here I build on the idea that the velocity and density components of the flow field cannot be viewed in isolation, and instead need to be viewed in terms of their momentum characteristics, which effectively unifies the two parameters. Moreover, I question the commonly used Boussinesq density approximation, which assumes that density stratification characteristics are negligible in defining the flow behavior of particle gravity currents, as would be the case in saline generated density flows. Therefore the objective of this chapter is to use the experimental currents presented in **Chapter 3** to highlight the degree of variation between the velocity and momentum fields under different density stratification conditions, and develop a novel conceptual model that shifts the focus from a velocity-centric to a density-centric based framework to define the net flow characteristics of turbidity currents. At the time of submitting this thesis, this chapter is being prepared for submission to Science. In this article, my contribution consists of identifying that momentum, rather than velocity, as the key parameter in defining the flow structure of particle gravity currents. I was responsible for identifying the short-comings of the Boussinesq density approximation in the context of analyzing turbidity currents, the ensuing proof of concept, and writing the manuscript.

1.6. **References**

Allen, J. R. L. (1971). Mixing at Turbidity Current Heads, and Its Geological Implications. *Journal of Sedimentary Petrology, 41*(1), 97-&. doi: 10.1306/74d721f8-2b21-11d7-8648000102c1865d

Arnott, R. W. C. (2007). Stratal architecture and origin of lateral accretion deposits (LADs) and conterminuous inner-bank levee deposits in a base-of-slope sinuous channel, lower Isaac Formation (Neoproterozoic), East-Central British Columbia, Canada. *Marine and Petroleum Geology, 24*(6-9), 515-528. doi: 10.1016/j.marpetgeo.2007.01.006

Baas, J. H., & Best, J. L. (2002). Turbulence modulation in clay-rich sediment-laden flows and some implications for sediment deposition. *Journal of Sedimentary Research, 72*(3), 336-340. doi: 10.1306/120601720336

Baas, J. H., Van Kesteren, W., & Postma, G. (2004). Deposits of depletive high-density turbidity currents: a flume analogue of bed geometry, structure and texture. *Sedimentology, 51*(5), 1053-1088. doi: 10.1111/j.1365-3091.2004.00660.x

Bagnold, R. A. (1956). The Flow of Cohesionless Grains in Fluids. *Philosophical Transactions of the Royal Society A: Mathematical, Physical and Engineering Sciences, 249*(964), 235-297. doi: 10.1098/rsta.1956.0020

Bennett, S. J., & Best, J. L. (1995). Mean flow and turbulence structure over fixed, two-dimensional dunes: implications for sediment transport and bedform stability. *Sedimentology, 42*(3), 491-513. doi: 10.1111/j.1365-3091.1995.tb00386.x

Best, J. (1992). On the Entrainment of Sediment and Initiation of Bed Defects - Insights from Recent Developments within Turbulent Boundary-Layer Research. *Sedimentology, 39*(5), 797-811. doi: 10.1111/j.1365-3091.1992.tb02154.x

Best, J. (1993). On the interactions between turbulent flow structure, sediment transport and bedform development: some considerations from recent experimental research. In N. Clifford, J. R. French & J. Hardisty (Eds.), *Turbulence: Perspectives on flow and sediment transport.* (pp. 197-213). New York: Wiley and Sons Ltd.

Best, J. (2005). The fluid dynamics of river dunes: A review and some future research directions. *Journal of Geophysical Research-Earth Surface, 110*(F4). doi: 10.1029/2004jf000218

Best, J. L., Kostaschuk, R. A., Peakall, J., Villard, P. V., & Franklin, M. (2005). Whole flow field dynamics and velocity pulsing within natural sediment-laden underflows. *Geology, 33*(10), 765-768. doi: 10.1130/G21516.1

Bouma, A. H. (1962). *Sedimentology of some flysch deposits: a graphic approach to facies interpretation*. Amsterdam: Elsevier.

Britter, R. E., & Linden, P. F. (1980). The motion of the front of a gravity current travelling down an incline. *Journal of Fluid Mechanics*, *99*(03), 531. doi: 10.1017/s0022112080000754

Burr, D. M., Bridges, N. T., Marshall, J. R., Smith, J. K., White, B. R., & Emery, J. P. (2015). Higher-than-predicted saltation threshold wind speeds on Titan. *Nature, 517*(7532), 60-63. doi: 10.1038/nature14088

Cantero, M. I., Balachandar, S., Garcia, M. H., & Bock, D. (2008). Turbulent structures in planar gravity currents and their influence on the flow dynamics. *Journal of Geophysical Research-Oceans, 113*(C8). doi: 10.1029/2007jc004645

Cartigny, M. J. B., Eggenhuisen, J. T., Hansen, E. W. M., & Postma, G. (2013). Concentration-Dependent Flow Stratification in Experimental High-Density Turbidity Currents and Their Relevance to Turbidite Facies Models. *Journal of Sedimentary Research, 83*(11-12), 1047-1065. doi: 10.2110/Jsr.2013.71

Curray, J. R., Emmel, F. J., & Moore, D. G. (2002). The Bengal Fan: morphology, geometry, stratigraphy, history and processes. *Marine and Petroleum Geology, 19*(10), 1191-1223. doi: 10.1016/S0264-8172(03)00035-7

Diplas, P., Dancey, C. L., Celik, A. O., Valyrakis, M., Greer, K., & Akar, T. (2008). The role of impulse on the initiation of particle movement under turbulent flow conditions. *Science, 322*(5902), 717-720. doi: 10.1126/science.1158954

Droz, L., Rigaut, F., Cochonat, P., & Tofani, R. (1996). Morphology and recent evolution of the Zaire turbidite system (Gulf of Guinea). *Geological Society of America Bulletin, 108*(3), 253-269. doi: Doi 10.1130/0016-7606(1996)108<0253:Mareot>2.3.Co;2

Falco, R. E. (1977). Coherent motions in the outer region of turbulent boundary layers. *Physics of Fluids, 20*(10), S124. doi: 10.1063/1.861721

Felix, M. (2002). Flow structure of turbidity currents. *Sedimentology, 49*(3), 397-419. doi: 10.1046/j.1365-3091.2002.00449.x

Ferguson, R. I., & Church, M. (2004). A simple universal equation for grain settling velocity. *Journal of Sedimentary Research, 74*(6), 933-937. doi: Doi 10.1306/051204740933

Ferguson, R. I., Kirkbride, A. D., & Roy, A. G. (1996). Markov analysis of velocity fluctuations in gravel-bed rivers. In P. J. Ashworth, J. L. Best, S. J. Bennett & S. J. McLelland (Eds.), *Coherent Flow Structures in Open Channels* (pp. 165–183). New York: John Wiley.

Galy, V., France-Lanord, C., Beyssac, O., Faure, P., Kudrass, H., & Palhol, F. (2007). Efficient organic carbon burial in the Bengal fan sustained by the Himalayan erosional system. *Nature, 450*(7168), 407-410. doi: 10.1038/nature06273

García, M. H. (1993). Hydraulic Jumps in Sediment-Driven Bottom Currents. *Journal of Hydraulic Engineering, 119*(10), 1094-1117. doi: 10.1061/(asce)0733-9429(1993)119:10(1094)

Geyer, W. R. (1993). The Importance of Suppression of Turbulence by Stratification on the Estuarine Turbidity Maximum. *Estuaries, 16*(1), 113-125. doi: 10.2307/1352769

Gordon, A. L., Orsi, A. H., Muench, R., Huber, B. A., Zambianchi, E., & Visbeck, M. (2009). Western Ross Sea continental slope gravity currents. *Deep-Sea Research Part Ii-Topical Studies in Oceanography, 56*(13-14), 796-817. doi: 10.1016/j.dsr2.2008.10.037

Grass, A. J. (1971). Structural Features of Turbulent Flow over Smooth and Rough Boundaries. *Journal of Fluid Mechanics, 50*(2), 233-255. doi: 10.1017/S0022112071002556

Hagen, R. A., Bergersen, D. D., Moberly, R., & Coulbourn, W. T. (1994). Morphology of a large meandering submarine canyon system on the Peru-Chile forearc. *Marine Geology, 119*(1-2), 7-38. doi: 10.1016/0025-3227(94)90138-4

Hosseini, S. A., Shamsai, A., & Ataie-Ashtiani, B. (2006). Synchronous measurements of the velocity and concentration in low density turbidity currents using an Acoustic Doppler Velocimeter. *Flow Measurement and Instrumentation, 17*(1), 59-68. doi: 10.1016/j.flowmeasinst.2005.05.002

Khripounoff, A., Vangriesheim, A., Babonneau, N., Crassous, P., Dennielou, B., & Savoye, B. (2003). Direct observation of intense turbidity current activity in the Zaire submarine valley at 4000 m water depth. *Marine Geology, 194*(3-4), 151-158. doi: 10.1016/S0025-3227(02)00677-1

Klaucke, I., & Hesse, R. (1996). Fluvial features in the deep-sea: New insights from the glacigenic submarine drainage system of the Northwest Atlantic Mid-Ocean Channel in the Labrador Sea. *Sedimentary Geology, 106*(3-4), 223-234. doi: Doi 10.1016/S0037-0738(96)00008-5

Kline, S. J., Reynolds, W. C., Schraub, F. A., & Runstadler, P. W. (1967). The structure of turbulent boundary layers. *Journal of Fluid Mechanics, 30*(4), 741-773. doi: 10.1017/s0022112067001740

Kneller, B., & Buckee, C. (2000). The structure and fluid mechanics of turbidity currents: a review of some recent studies and their geological implications. *Sedimentology, 47*, 62-94. doi: 10.1046/j.1365-3091.2000.047s1062.x

Kneller, B. C., Bennett, S. J., & McCaffrey, W. D. (1997). Velocity and turbulence structure of density currents and internal solitary waves: potential sediment transport and the formation of wave ripples in deep water. *Sedimentary Geology, 112*(3-4), 235-250. doi: 10.1016/S0037-0738(97)00031-6

Kneller, B. C., Bennett, S. J., & McCaffrey, W. D. (1999). Velocity structure, turbulence and fluid stresses in experimental gravity currents. *Journal of Geophysical Research-Oceans, 104*(C3), 5381-5391. doi: Doi 10.1029/1998jc900077

Kolla, V. (2007). A review of sinuous channel avulsion patterns in some major deep-sea fans and factors controlling them. *Marine and Petroleum Geology, 24*(6-9), 450-469. doi: 10.1016/j.marpetgeo.2007.01.004

Kolmogorov, A. N. (1991). The Local-Structure of Turbulence in Incompressible Viscous-Fluid for Very Large Reynolds-Numbers. *Proceedings of the Royal Society of London Series a-Mathematical Physical and Engineering Sciences, 434*(1890), 9-13. doi: 10.1098/rspa.1991.0075

Komar, P. D. (1970). The Competence of Turbidity Current Flow. *Geological Society of America Bulletin, 81*(5), 1555. doi: 10.1130/0016-7606(1970)81[1555:tcotcf]2.0.co;2

Launder, B. E., & Rodi, W. (1983). The Turbulent Wall Jet Measurements and Modeling. *Annual Review of Fluid Mechanics, 15*(1), 429-459. doi: 10.1146/annurev.fl.15.010183.002241

Leeder, M. R., Gray, T. E., & Alexander, J. (2005). Sediment suspension dynamics and a new criterion for the maintenance of turbulent suspensions. *Sedimentology, 52*(4), 683-691. doi: 10.1111/j.1365-3091.2005.00720.x

Lumley, J. L., & Terray, E. A. (1983). Kinematics of Turbulence Convected by a Random Wave Field. *Journal of Physical Oceanography, 13*(11), 2000-2007. doi: 10.1175/1520-0485(1983)013<2000:Kotcba>2.0.Co;2

Marquis, G. A., & Roy, A. G. (2011). Bridging the gap between turbulence and larger scales of flow motions in rivers. *Earth Surface Processes and Landforms, 36*(4), 563-568. doi: 10.1002/Esp.2131

Marusic, I., Mathis, R., & Hutchins, N. (2010). Predictive model for wall-bounded turbulent flow. *Science, 329*(5988), 193-196. doi: 10.1126/science.1188765

McCaffrey, W. D., Choux, C. M., Baas, J. H., & Haughton, P. D. W. (2003). Spatio-temporal evolution of velocity structure, concentration and grain-size stratification within experimental particulate gravity currents. *Marine and Petroleum Geology, 20*(6-8), 851-860. doi: 10.1016/j.marpetgeo.2003.02.002

Middleton, G. V. (1966). Experiments on Density and Turbidity currents *Canadian Journal of Earth Sciences., 3*, 523-546.

Middleton, G. V. (1993). Sediment Deposition from Turbidity Currents. *Annual Review of Earth and Planetary Sciences, 21*(1), 89-114. doi: 10.1146/annurev.earth.21.1.89

Nezu, I., & Nakagawa, H. (1993). *Turbulence in Open-Channel Flows*: A.A. Balkema.

Nikora, V. (2007). 3 Hydrodynamics of gravel-bed rivers: scale issues. In H. Habersack, H. Piégay & R. Massimo (Eds.), *Developments in Earth Surface Processes: Gravel-bed Rivers VI, From Process Understanding to River Restoration* (pp. 61–81). Amsterdam: Elsevier.

Peakall, J., Ashworth, P., & Best, J. (1996). Physical Modelling in Fluvial Geomorphology: Principles, Applications and Unresolved Issues. In B. L. Rhoads & C. E. Thorne (Eds.), *The Scientific Nature of Geomorphology: Proceedings of the 27th Binghamton Symposium in Geomorphology, Held 27-29 September, 1996* (Vol. 27, pp. 221-253): John Wiley and Sons.

Peakall, J., McCaffrey, B., & Kneller, B. (2000). A process model for the evolution, morphology, and architecture of sinuous submarine channels. *Journal of Sedimentary Research, 70*(3), 434-448. doi: 10.1306/2dc4091c-0e47-11d7-8643000102c1865d

Picot, M., Droz, L., Marsset, T., Dennielou, B., & Bez, M. (2016). Controls on turbidite sedimentation: Insights from a quantitative approach of submarine channel and lobe architecture (Late Quaternary Congo Fan). *Marine and Petroleum Geology, 72*, 423-446. doi: 10.1016/j.marpetgeo.2016.02.004

Pinkel, R. (1980). Acoustic Doppler Techniques. In F. Dobson, L. Hasse & R. Davis (Eds.), *Air-Sea Interaction* (pp. 171-199). USA: Springer.

Piper, D. J. W., Cochonat, P., & Morrison, M. L. (1999). The sequence of events around the epicentre of the 1929 Grand Banks earthquake: initiation of debris flows and turbidity current inferred from sidescan sonar. *Sedimentology, 46*(1), 79-97. doi: 10.1046/j.1365-3091.1999.00204.x

Reynolds, O. (1883). An Experimental Investigation of the Circumstances Which Determine Whether the Motion of Water Shall Be Direct or Sinuous, and of the Law of Resistance in Parallel Channels. *Philosophical Transactions of the Royal Society of London, 174*(0), 935-982. doi: 10.1098/rstl.1883.0029

Reynolds, O. (1895). On the Dynamical Theory of Incompressible Viscous Fluids and the Determination of the Criterion. *Philosophical Transactions of the Royal Society A: Mathematical, Physical and Engineering Sciences, 186,* 123-164. doi: 10.1098/rsta.1895.0004

Robinson, S. K. (1991). Coherent Motions in the Turbulent Boundary-Layer. *Annual Review of Fluid Mechanics, 23*, 601-639. doi: 10.1146/annurev.fluid.23.1.601

Sequeiros, O. E. (2012). Estimating turbidity current conditions from channel morphology: A Froude number approach. *Journal of Geophysical Research-Oceans, 117*(C4). doi: 10.1029/2011jc007201

Sequeiros, O. E., Naruse, H., Endo, N., Garcia, M. H., & Parker, G. (2009). Experimental study on self-accelerating turbidity currents. *Journal of Geophysical Research-Oceans, 114*(C5). doi: 10.1029/2008jc005149

Sequeiros, O. E., Spinewine, B., Beaubouef, R. T., Sun, T., Garcia, M. H., & Parker, G. (2010). Characteristics of Velocity and Excess Density Profiles of Saline Underflows and Turbidity Currents Flowing over a Mobile Bed. *Journal of Hydraulic Engineering, 136*(7), 412-433. doi: 10.1061/(Asce)Hy.1943-7900.0000200

Talling, P. J., Wynn, R. B., Masson, D. G., Frenz, M., Cronin, B. T., Schiebel, R., . . . Amy, L. A. (2007). Onset of submarine debris flow deposition far from original giant landslide. *Nature, 450*(7169), 541-544. doi: 10.1038/nature06313

Taylor, G. I. (1938). The spectrum of turbulence. *Proceedings of the Royal Society of London Series a-Mathematical and Physical Sciences, 164*(A919), 0476-0490. doi: 10.1098/rspa.1938.0032

Terlaky, V., Rocheleau, J., & Arnott, R. W. C. (2016). Stratal composition and stratigraphic organization of stratal elements in an ancient deep-marine basin-floor succession, Neoproterozoic Windermere Supergroup, British Columbia, Canada. *Sedimentology, 63*(1), 136-175. doi: 10.1111/sed.12222

Tilston, M., Arnott, R. W. C., Rennie, C. D., & Long, B. (2015). The influence of grain size on the velocity and sediment concentration profiles and depositional record of turbidity currents. *Geology, 43*(9), 839-842. doi: 10.1130/g37069.1

Urick, R. J. (1948). The Absorption of Sound in Suspensions of Irregular Particles. *The Journal of the Acoustical Society of America, 20*(3), 283. doi: 10.1121/1.1906373

Venditti, J. G., Church, M., & Bennett, S. J. (2006). On interfacial instability as a cause of transverse subcritical bed forms. *Water Resources Research, 42*(7). doi:10.1029/2005wr004346

Williams, P. B., & Kemp, P. H. (1971). Initiation of ripples on a flat sediment bed. *Journal of Hydraulic Engineering, 97*(4), 502-522.

1.7. **List of Figures**

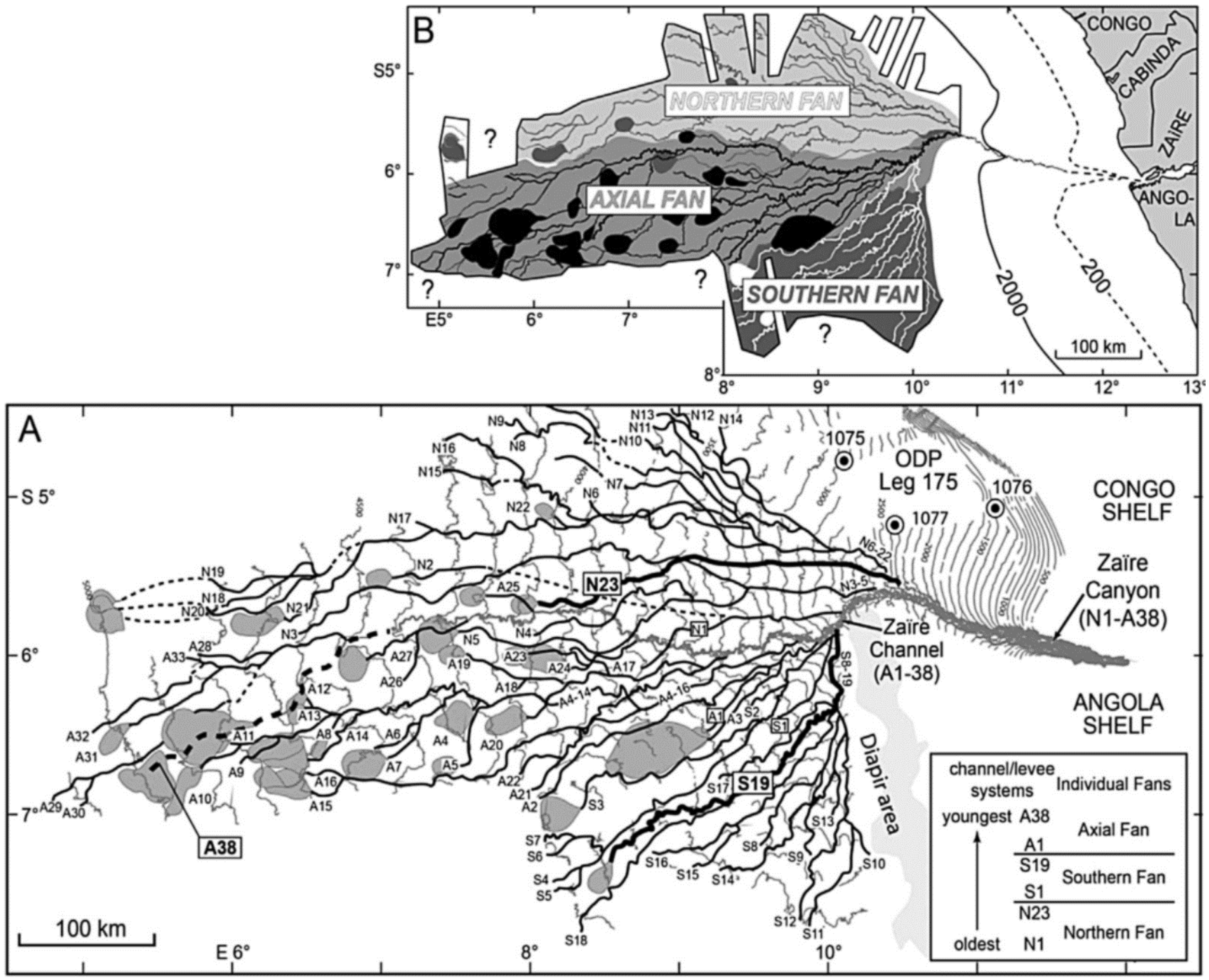

Figure 1-1: Example of a modern day submarine fan complex showing the connection in sediment transport from terrestrial to deep marine environments (Picot et al., 2016). Note the frequent shifting of the active channel in the distributary network leading complex depositional feature consisting of a series of amalgamated lobes.

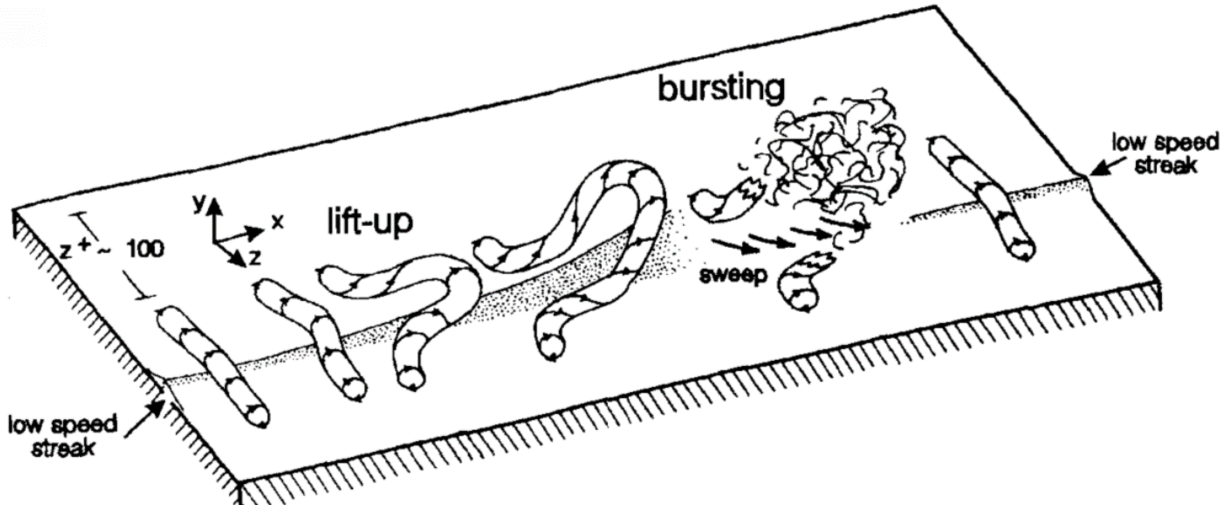

Figure 1-2:Schematic of hairpin vortex demonstrating the bursts (slow moving fluid directed away from the bed) and sweeps (fast moving fluid directed towards the bed) that are the physical manifestation of the Reynolds stress (Best, 1992).

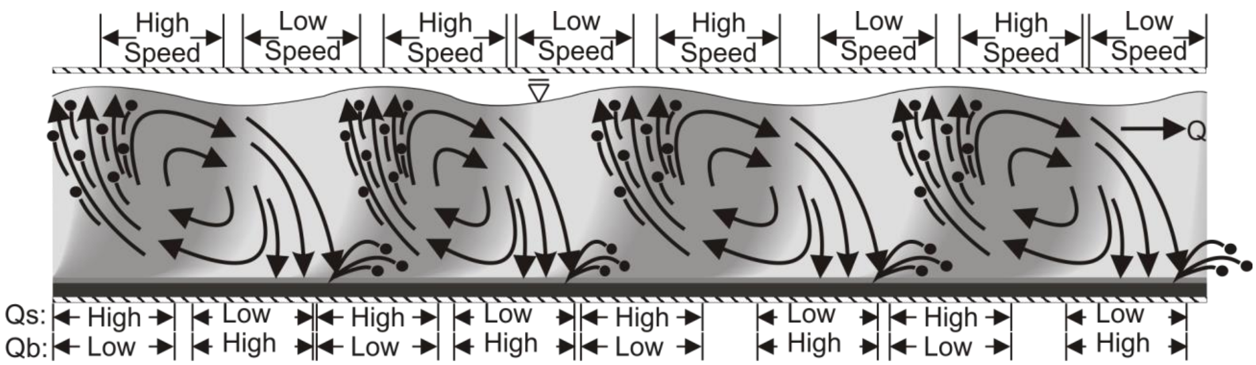

Figure 1-3: Representation of coupling between coherent fluid structures and sediment transport events in open channel flow, adapted from Ferguson et al. (1996). The variables Q, Q_s and $Q_b$correspond to discharge, suspended load and bedload transport rates, respectively. Given the logarithmic nature of the near-bed region of turbidity currents, it is anticipated that they will display similar behavior with respect to coherent fluid structures and sediment transport processes.

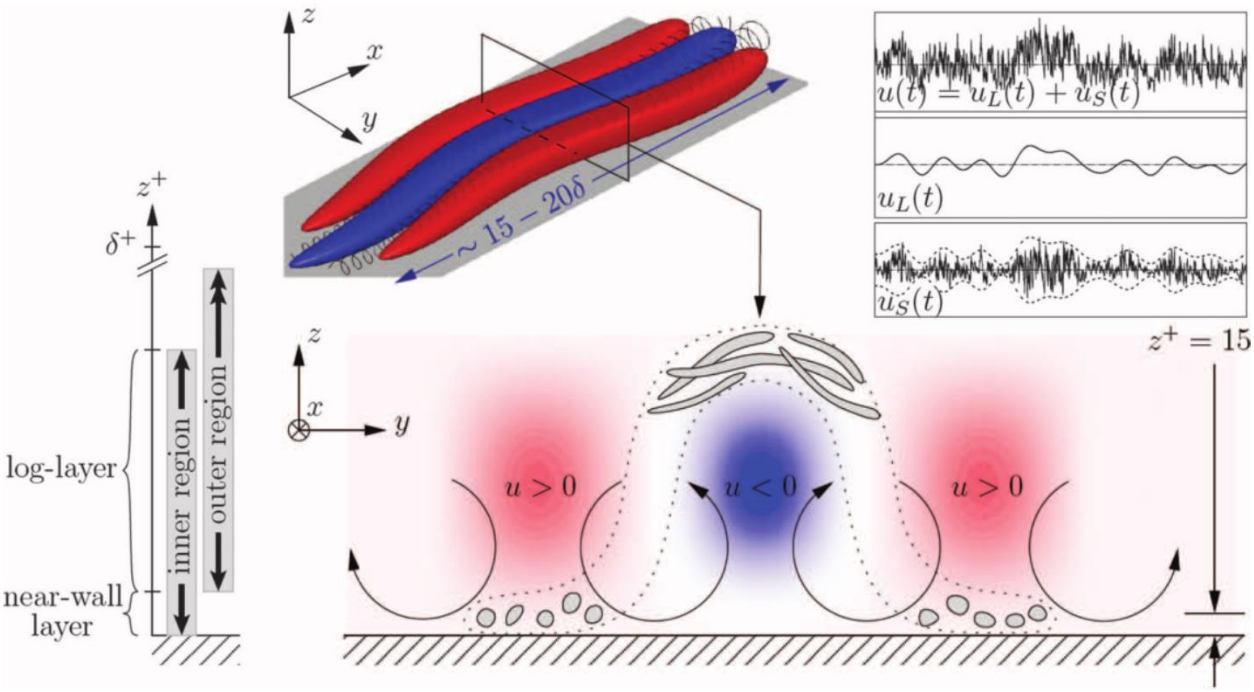

Figure 1-4: Schematic showing the existence of very large coherent fluid structures (much larger than the thickness of the boundary layer (δ)) and their interactions with small scale hair-pin vortices near the wall (Marusic et al., 2010).

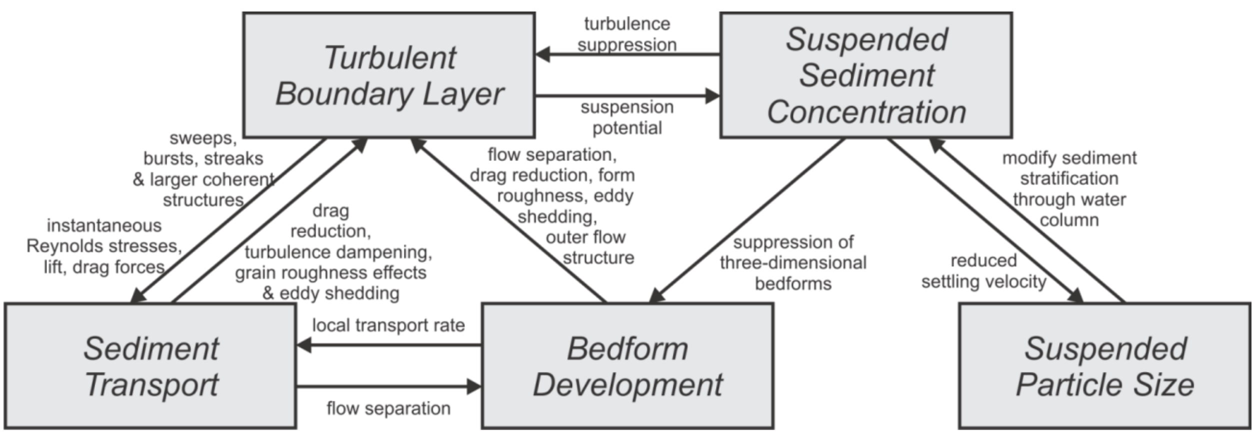

Figure 1-5: Conceptual model showing interactions between turbulent boundary layers, sediment transport and bedform development in open channel flow (adapted from Best (1993)). Additional feedbacks due to the concentration and size of suspended sediments that define turbidity currents are included to demonstrate the extra complexities associated with particle gravity currents.

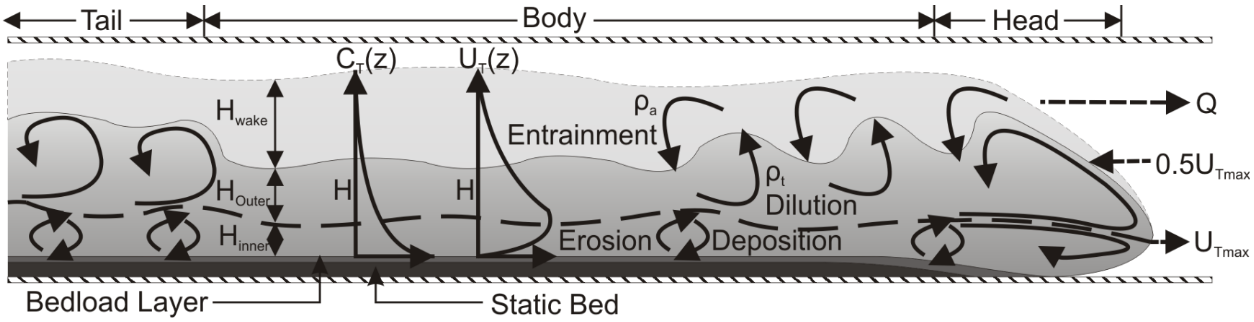

Figure 1-6: Representation of the longitudinal and vertical anatomy of a turbidity current's flow structure. Longitudinally, the current can be divided into three parts, 1) the head, 2) the body and 3) the tail. The current can also be divided vertically into two zones, 1) the inner region (below u_{max}), where velocity increases logarithmically away from the bed, which is the primary source of flow resistance, and 2) the outer region (above u_{max}) where velocity decreases exponentially and flow resistance results from mixing with the ambient fluid (e.g., Hosseini et al., 2006).

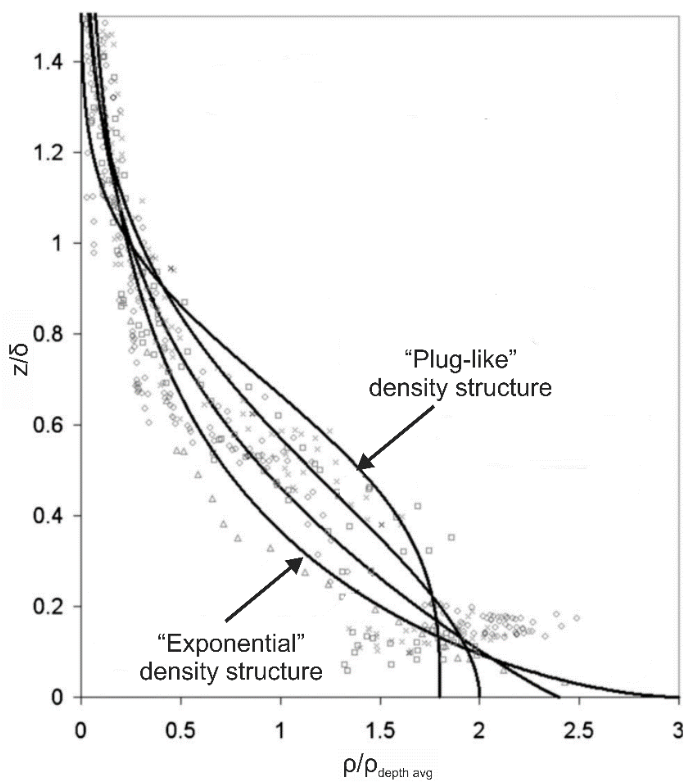

Figure 1-7: Example of two end-member density structures in turbidity currents, 1) exponential ($(\partial\rho/\partial z)_{max}$ at base of flow), and 2) "plug-like" ($(\partial\rho/\partial z)_{max}$ at top of flow). Adapted from Sequeiros et al. (2010).

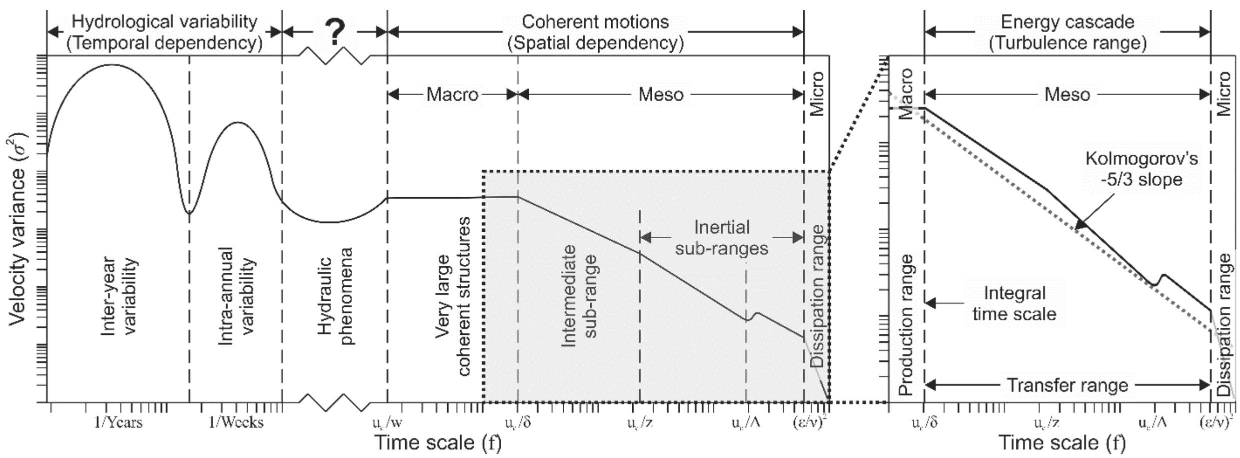

Figure 1-8: Generalized velocity spectra illustrating how the velocity variance (σ^2) from time-series velocity data is partitioned across a broad range of scales (adapted from Nikora (2007)). These scales can be partitioned on the bases of temporally dependent scales (years to weeks) that result from allogenic factors (e.g. climate change, extreme flood events), or spatially dependent scales that result from autogenic factors (e.g. channel width (w), boundary layer thickness (δ), height above bed (z) and particle roughness length (Δ)). The spatial/autogenic factors can be further classified on the bases of non-turbulent (larger) and turbulent (smaller) scales of motion (see inset). The turbulent range can be identified by energy cascade theory, and is characterized by a -5/3rd's slope (Kolmogorov, 1991). The largest fluctuations associated with the 5/3rd's slope is referred to as the integral time scale, and defines the transition between the turbulent and non-turbulent velocity fluctuations within the range of spatially dependent coherent fluid motions.

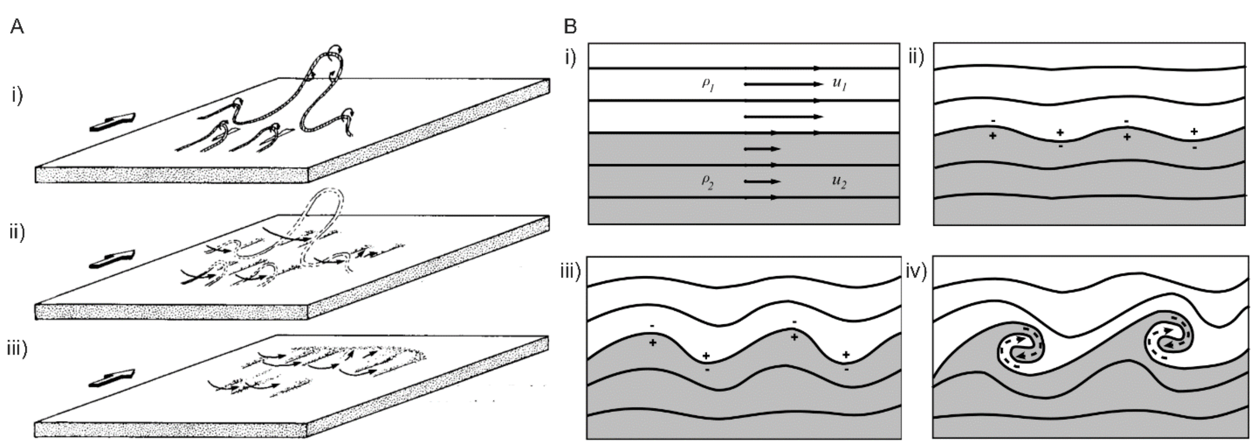

Figure 1-9: Turbulence model (A, adapted from Best (1992)) and hydrodynamic instability model (B, Venditti et al. (2006)) for generating initial bed defects that lead to the development of

angular bedforms. In the turbulence model, the lifting of the leading edge of hairpin vorticities away from the bed (Ai) allow for the inrush of high-speed fluid towards the bed that promoted localized sediment transport (Aii) and the resulting depositional mound (Aiii) promotes flow separation and the development of these mounds propagate downstream as a result of a singular bed defect. In the hydrodynamic instability model, the flow (represented by $_1$) and the bedload layer (represented by $_2$) are treated as two distinct fluids of varying velocity (u) and density (ρ) (Bi). The streamwise variations in u and ρ promote the alteration of convergent (acceleration) and divergent (deceleration) streamlines across the fluid-bedload interface (Bii). From Bernoulli's principle, the streamwise variations are matched by (out of phase) pressure variations (indicated by the + and – signs, Biii) and the organization of laterally oriented vorticities concentrated along the crests of the bedlaod layer (Biv).

CHAPTER 2: A TIME-FREQUENCY DEPENDENT METHOD FOR ESTIMATING CONVECTION VELOCITIES AND ISOLATING TURBULENCE USING LENGTH-SCALE BASED FILTERING IN UNSTEADY FLOWS

M. Tilston[1], R.W.C. Arnott[1] and C.D. Rennie[2]

[1]Department of Earth Sciences, University of Ottawa, Ottawa ON

[2]Department of Civil Engineering, University of Ottawa, Ottawa ON

2.1. **Abstract**

Due to their highly unsteady nature in terms of flow properties and boundary layer thickness, turbidity currents pose numerous challenges for even the most rudimentary analytical procedures such as decoupling the turbulent and non-turbulent components of the flow. Typically, frequency based filters are employed in such conditions to isolate fluid turbulence, but this is dependent on the ability to identify the integral length scale. This nuance poses distinct challenges for the analysis of unsteady flows since convection velocities are time and frequency dependent, resulting in distortions of time-averaged energy spectra. In this study, we use the continuous wavelet transform and employ a novel technique for estimating the eddy convection velocity for all frequencies and all times in the transform to convert instantaneous spectra from time-scale to length-scale domains prior to the averaging process. Subsequently, length-scale filtering is employed to ensure that an eddy of a given size is consistently associated with either the turbulent or non-turbulent components of flow. Results indicate that our technique of deriving convective velocities are identical to that of Taylor's hypothesis after time-averaging, but can account for temporal and frequency variations of this parameter. Thus, compared to Taylor's frozen turbulence hypothesis, turbulent structures are considered frozen rather than the entire flow field due to temporal fluctuations in their convective velocities, which questions the validity of Reynolds decomposition for isolating turbulence in unsteady and quite possibly also steady flows.

Keywords: Unsteady flow, turbulence, Taylor's hypothesis, eddy convection velocity, turbidity current

2.2. **Introduction**

Perhaps the most studied aspect of geophysical flows is fluid turbulence, a subject that has persistently captivated (and confounded) the minds of numerous researchers for more than 100 years. Historically described as a stochastic process, it is now generally accepted that fluid turbulence consists of organized, coherent structures (Grass, 1971; Kline et al., 1967). In open channel flows, the maximum size of turbulent eddies, i.e. the integral length scale, is controlled by boundary layer thickness; these features are inherently unstable and break up, transferring their energy to progressively smaller eddies until they are eventually dissipated via molecular viscosity (Kolmogorov, 1991). This process is often demonstrated through frequency domain spectral analysis where the energy cascade, or the region between the integral and dissipative time scales, is characterized by a slope of -5/3 (Kolmogorov, 1991). Yet turbulence is an inherently spatio-temporal phenomenon, and with recent advances in particle image velocimetry (PIV), it is now possible to resolve fully both the spatial and temporal properties of turbulent structure in clear-water flows (Raffel et al., 2007). However many geophysical flows are too opaque for the acquisition of spatial velocity data by non-intrusive optical means such as PIV, and most PIV systems are of limited utility in high Reynolds number flows. Consequently, many experimental studies rely solely on at-a-point time series velocity data; accordingly Taylor's hypothesis (or more correctly, Taylor's approximation), which assumes that the spatial structure of a turbulent velocity field from local, time-averaged flow measurements (Taylor, 1938). While this approach has been applied to numerous turbulence studies in steady flows, it is ill-suited for unsteady conditions because signal deconvolution techniques yield time-averaged, frequency domain spectra, yet unsteadiness negates the assumption that the duration of a single structure can be equated to a constant length, resulting in spectral distortions. Traditionally, this is handled by limiting analysis to shorter segments of the signal where flow is quasi-steady (e.g. Rennie & Hay, 2010), but this limits the range of frequencies that can be investigated, and longer structures cannot be studied. Moreover, it poses major challenges for spectral filtering, which is needed to distinguish the turbulent and non-turbulent frequency components of at-a-point velocity data.

In general, the first step in turbulence analysis is to differentiate the turbulent and non-turbulent portions of the flow, which can lead to errors in even the most basic turbulence parameters such as turbulence intensity and the Reynolds stress if not done correctly. Presently, there is no satisfactory technique for identifying the turbulent and non-turbulent components in highly unsteady flows. For time series datasets, the instantaneous fluid velocity (u) is the sum of the turbulent and non-turbulent contributions to the flow field, which is defined as

$$u = \tilde{u} + u'. \qquad 2.1$$

Here, u' and $\tilde{u}$ are the turbulent and non-turbulent contributions, respectively. Studies focusing on the turbulence characteristics of density-driven flows such as turbidity currents have largely avoided this issue by focusing on the body of the current, where flow and boundary layer thickness (δ) are assumed to be steady, thus the non-turbulent component is simply $\bar{u}$, or the time-averaged velocity (Reynolds, 1895), and δ is equivalent to $\bar{\delta}$. Yet turbidity current deposits, or turbidites, are characterized by a distinctive upward change in grain size and bed features interpreted to result from waning flow conditions (Bouma, 1962). This suggests that turbidity currents are unsteady by definition, and the entire anatomy of the current must be studied to investigate the feedbacks between coherent fluid structures, sediment transport and bedform development. We are only aware of one study that has analyzed turbulence continuously through the entire current (Choux et al., 2005), but here the non-turbulent component of the flow ($\tilde{u}$) was identified by using a moving average function. While these authors performed a sensitivity analysis to justify their choice of window size, their results focused on time-averaged turbulence statistics rather than discrete coherent fluid structures, which are likely more sensitive to the degree of smoothing incorporated into the averaging function. A more objective approach is to use a combination of spectral analysis and band-pass filtering to identify the turbulent and non-turbulent components of the flow, which, for example, is common practice in marine environments for removing the effects of long period, non-turbulent oscillations associated with waves and tides (French & Clifford, 1992; Heathershaw, 1975; Rennie & Hay, 2010).

Spectral analysis is used as a tool to identify the integral time scale, which is treated as the threshold between turbulent and non-turbulent motions (Nezu & Nakagawa, 1993) (Figure 2-1a), and a high-pass frequency filter is then applied to isolate the turbulent component of the flow. Yet conventional methods for performing signal deconvolution, such as the Fourier transform, assume a constant sampling frequency to create a temporally averaged energy spectrum; thus

Taylor's hypothesis assumes that fluid structures of a given duration have identical length, and the effect of temporal fluctuations in convective velocity are negligible. However turbulence is an inherently spatial phenomenon and in unsteady flows, constant time cannot necessarily be equated to constant length. To demonstrate why this is problematic with respect to the overall shape of time-averaged spectra and frequency-based filtering, consider an eddy of length (λ) at two different vertical points in a steady, open channel flow (Figure 2-1b). Mean velocity ($\bar{u}$), and therefore eddy convection rate (u_c), is greater higher in the water column, and as a consequence two eddies of equal length will have two different frequencies (f); faster regions of flow alias λ towards higher frequencies and slower regions of flow alias λ towards lower frequencies. As a result, the spectra from these two points will have different integral time scales in spite of sharing identical integral length scales since the size of the largest turbulent eddies relates to boundary layer thickness (δ) (Nikora, 2007) (Figure 2-1c). Accordingly, spectra from single point velocity data in steady flows are often normalized with respect to changes in flow velocity by converting from temporal to spatial domains, thus permitting direct comparisons of the size and intensity of turbulent structures at different points in the water column (Soulsby, 1977). This is analogous to what occurs temporally within single-point velocity data time series in unsteady flows; although their integral length scales should remain constant, the integral time scales from segments of the signal containing high speed fluid are different (shorter) than those from low-speed fluid, and temporally averaging the two causes an apparent reduction in slope through the energy cascade, and produces a broad range of frequencies associated with the integral time scale. As such, instantaneous spectra are needed to convert from temporal (Eulerian) to spatial (Lagrangian) domains prior to averaging. Afterwards, the integral length scale can then be used as the criterion to differentiate between the turbulent and non-turbulent components of the flow. This, however, is problematic, since there is no established method for estimating eddy convection velocity in unsteady flows.

Converting between Eulerian and Lagrangian domains requires some knowledge of the eddy convection velocity (u_c), thus converting from frequency (f) to length scale (λ)

$$\lambda = |u_c/f|, \qquad 2.2$$

where the bars on the right hand side represent the absolute value, thereby eliminating negative length scales. In his seminal work on the subject, Taylor (1938) proposed that in steady flows, if the magnitude of turbulent fluctuations ($|u'|$) were small compared to the mean flow velocity ($\bar{u}$), then turbulent eddies are, on average, convected at a rate approximated by the time-averaged velocity. Thus Taylor's frozen turbulence hypothesis implies that u_c is independent of both time and the size of the turbulent structures. The equivalent to Taylor's hypothesis for unsteady flows would be to assume that the convection velocity is closely approximated by the non-turbulent component of the flow ($\tilde{u}$), thus discrete turbulent structures are frozen, but the flow field as a whole is "slushy". However, using $\tilde{u}$ to approximate the eddy convection velocity in unsteady flows poses two key difficulties. First, it neglects the temporal and frequency dependency of u_c. Numerous studies have demonstrated that u_c depends on the size of the structure, and neglecting this can result in over (or under) estimating their true length (Buxton et al., 2013; Krogstad et al., 1998; LeHew et al., 2010; Zaman & Hussain, 1981). Recently, however, Del Álamo and Jiménez (2009) demonstrated that the local mean velocity provides a reasonable approximation of the mean convection rate for only smaller eddies, whereas larger eddies are convected at a rate proportional to bulk flow velocity. Although these authors developed a novel technique to predict u_c for each unique Fourier frequency, it does not account for the temporal dependency of u_c, which can introduce substantial errors in length scale estimates, even in steady flows. Fisher and Davies (1964) demonstrated that large instantaneous fluctuations about the mean velocity result in large deviations between u_c and $\bar{u}$. Subsequently, Lumley (1965) performed a theoretical analysis to investigate the different mechanisms that may invalidate Taylor's hypothesis, and found that at high frequencies, all other effects, except those of turbulence induced fluctuations in u_c, could be neglected. Despite this being a recognized problem, there has previously been no method to account for temporal fluctuations in u_c, which can likely be attributed to the use of time-averaged energy spectra. The second issue is related to the analytical framework for decoupling the turbulent and non-turbulent components of unsteady flows. Specifically, instantaneous spectra and estimates of u_c for all frequencies and at all times are needed to produce better estimates of true length scales and generate normalized time-averaged spectra, which is a precursor to obtaining the non-turbulent component ($\tilde{u}$). Thus $\tilde{u}$ cannot be used to estimate u_c in unsteady flows, and convection velocities for all frequencies and at all times in the convolution must be derived directly from the raw signal. Moreover, numerous studies have demonstrated through space-time correlation that a given Fourier frequency is actually composed of a range of unique length scales because of the effects of turbulence (e.g.Wills (1964)) and therein emphasizing the essential need for instantaneous convection velocities in the analysis of both steady and unsteady flows. Presently, however, there is no technique to account for both the frequency and time dependency of u_c.

The present study focuses on turbidity currents, which are turbulent particle suspensions that behave like surge flows and wall-bounded jets in the longitudinal and vertical directions, respectively (Kneller & Buckee, 2000). Thus they differ in velocity and concentration profiles compared to open channel flow in that the highest velocities are depressed towards the base of the flow as opposed to being at the top, and they have higher concentrations of suspended sediment that are dispersed more evenly throughout the flow thickness (Figure 2-2). Natural turbidity currents are notoriously destructive and efforts to monitor and measure their flow characteristics in the modern deep oceans have been generally unsuccessful (Khripounoff et al., 2003). As a consequence much of the present understanding of turbidity currents has been gained through the study of small-scale laboratory currents. However sediment-transporting laboratory currents are typically highly depositional and always short in duration, commonly lasting for only a few to several tens of seconds, during which they are highly unsteady in terms of their flow properties and boundary layer thicknesses (Kneller et al., 1997; Leclair & Arnott, 2005).

Here we propose a new method to identify the turbulent and non-turbulent components in unsteady flows, including turbidity currents. This technique makes use of the continuous wavelet transform (CWT) - a technique that produces instantaneous spectra rather than an average spectrum. Each unique CWT spectrum is normalized by deriving a unique u_c for all frequencies and at all times throughout the sampling window. It should be noted that the aim of this work is not to describe the spatial structure of turbulence in unsteady flows, but rather to provide an approach for isolating turbulence based on a Lagrangian frame of reference using Eulerian data. Results using this technique demonstrate that the mean values of u_c are in good agreement with those predicted by the non-turbulent component of the flow ($\tilde{u}$), but show substantial deviations with respect to their instantaneous values.

2.3. **Deriving temporal and scale dependent convective velocities (u_c) and boundary layer thicknesses (δ_c) from instantaneous velocity data**

Unlike traditional transforms, continuous wavelet transforms (CWTs) act like a series of narrow band-pass filters to produce unique power spectra for each instantaneous measurement, so it is possible to examine how spectral energy changes in both frequency and time. Consequently, CWT's are being increasingly used *in lieu* of traditional (i.e. Fourier) transforms in a range of geophysical studies (Adamowski et al., 2009; Higgins et al., 2012) including coherent structures in turbulent flows (Farge, 1992), and notably, turbulence analysis of sediment gravity currents (Choux et al., 2005; Gray et al., 2005). To date, CWTs have been used mostly for investigating the temporal dynamics of a signal's spectral signature, yet theey are also ideally suited for signal filtering with the aim of decoupling the turbulent and non-turbulent components from instantaneous velocity data in highly unsteady flow. By producing instantaneous spectra, it will be demonstrated that it is possible to correct for temporal variations in eddy convective velocity (u_c), and to develop dynamic filters to isolate the turbulent and non-turbulent contributions in the signal. To date, we are unaware of any studies that have attempted to exploit either of these two aspects of the CWT.

The CWT ($W(s_j, n)$) of a timeseries u_i with N instantaneous measurements is the convolution of u_i with scaled and translated versions of the mother wavelet $\psi_0(\eta)$, and can be expressed as

$$W(s_j, n) = \sum_{n'=0}^{N-1} u_i(n')\psi^* \left[\frac{(n'-n)\partial t}{s_j}\right], \qquad 2.3$$

where (*) indicates the complex conjugate, n is a counter for location within the timeseries, and ∂t is the time step, and s_j is an individual scale used in the decomposition, which is defined as

$$s_j = s_0 2^{j\partial j}, \qquad j = 0,1, \ldots J. \qquad 2.4$$

Here, ∂j is a user specified constant whose minimum value varies with choice of base wavelet function used in the decomposition, and the terms s_0 and s_J represent the smallest and largest scales used in the transform, respectively (Torrence & Compo, 1998). Thus the dimensions of the matrix W are defined by the number of instantaneous velocity measurements (N) and the number of wavelet scales used in the CWT (J). Converting from wavelet coefficients to wavelet power ($P(s_j, n)$) is a straightforward procedure, as for any given scale and point in time

$$P(s_j, n) = \left|W(s_j, n)\right|^2, \qquad 2.5$$

where the quantity $\left|W(s_j, n)\right|$ is the absolute value of $W(s_j, n)$. To make direct comparisons against the spectra obtained by more traditional approaches, s_j are converted to the equivalent Fourier frequency (f_j) by multiplying by a constant whose value depends on the choice of mother wavelet (Meyers et al., 1993). Thus the time-averaged CWT spectra can be calculated by determining the mean spectral energy for each wavelet scale in the decomposition ($\bar{P}(s_j)$). More generally, the mean spectrum for any arbitrary segment of the signal is

$$\bar{P}(s_j) = \sum_{n=n_1}^{n_2} \frac{P(s_j, n)}{n_2 - n_1 + 1}, \qquad 2.6$$

where the over bar denotes temporal averaging. Although this describes the temporal properties of turbulence, as previously noted it is inherently a spatial phenomenon governed by boundary layer thickness (δ); consequently the temporal and frequency dependency of u_c and δ cannot be neglected when making inferences about the time-averaged spatial characteristics of turbulence from timeseries velocity data. This can only be accounted for due to the unique signal reconstruction properties of the CWT that allow for the derivation of u_c directly from the convolution, and changes in δ are subsequently determined through an iterative process.

Unlike conventional spectral analysis, which describes how signal variance is distributed across a range of frequencies for a given segment of a signal, instantaneous spectra describe how variance is distributed at a single point in time. Thus not only is it possible to reconstruct the signal directly from the transform, but it is possible to perform temporally dynamic filtering simply by omitting the unwanted wavelet coefficients from the reconstruction. Due to the scale and time redundancy inherent to the CWT, it is possible to reconstruct the signal using the delta function (∂) rather than the inverse of the wavelet function used in the decomposition (Farge, 1992). Thus, the reconstructed instantaneous measurement in the signal ($u_{rec}(n)$) is simply the sum of the real part of the wavelet coefficient ($\Re\{W(s_j, n)\}$) at all wavelet scales

$$u_{rec}(n) = \frac{\partial j \partial t^{1/2}}{C_\partial \psi_0(0)} \sum_{j=0}^{j=J} \frac{\Re\{W(s_j, n)\}}{s_j^{1/2}} , \qquad 2.7$$

where the factor $\psi_0(0)$ removes the energy scaling, and C_∂ is a constant that depends on the wavelet function used in the transform (Torrence & Compo, 1998). Since the decomposition acts as a series of band-pass filters, there will always be a residual velocity ($u_{res}(n)$) associated with scales $> s_J$, If s_J is sufficiently long with respect to the lowest period oscillations in the signal, then $u_{res}(n)$ is a constant, equivalent to $\bar{u}$. Otherwise, it can be defined as

$$u_{res}(n) = u(n) - u_{rec}(n). \qquad 2.8$$

Thus in situations requiring the use of a low-pass filter, such as isolating the non-turbulent portion of the flow, wavelet coefficients associated with smaller scales of motion are omitted from **equation 2.7,** and the resulting filtered velocity ($u_{filt}(n)$) is simply

$$u_{filt}(n) = u_{res}(n) + u_{rec}(n). \qquad 2.9$$

More importantly, instantaneous spectra can be corrected to account for unsteady effects that result in spectral distortions if one has prior knowledge of the scale-time localized eddy convection velocity ($u_c(s_j, n)$) and boundary layer thickness ($\delta_c(s_j, n)$).

To derive the eddy convection velocity for any given scale and point of time, we begin by making two assumptions. First, we assume that an eddy of a given size is insensitive to velocity fluctuations associated with smaller scales of motion, thus requiring a low-pass filter. Second, we assume that the convection velocity is accurately estimated by the local mean of the filtered velocity over the duration of the event. Thus the premise in the ensuing technique for deriving u_c is closely rooted in Kolmogorov's energy cascade theory, which is best summarized by the oft cited Richardson (1922) verse: "Big whirls have little whirls, which feed on their velocity; and little whirls have lesser whirls, and so on to viscosity". Thus small eddies are superimposed on larger eddies, and kinetic energy is transferred uni-directionally from large structures to small structures; by extension, this implies that an eddy of a given size is unaffected by smaller structures. Accordingly, the convective velocity for an eddy with a given frequency at any point in time can be derived by utilizing a low-pass filter to remove the wavelet coefficients associated with higher frequencies, reconstructing the signal directly from the CWT, and using a moving average with a temporal span equivalent to the frequency of the eddy in question. Thus in many ways, this approach is similar to Taylor's hypothesis in that it relies on local mean velocity rather than $\bar{u}$, but it accounts for the time-frequency dependency of u_c. Furthermore, u_c is derived directly from the instantaneous velocity data, thus eliminating the need for prior knowledge about the properties of the non-turbulent component of flow; this characteristic is crucial for analyzing unsteady currents.

By substituting **equation 2.7** into **equation 2.9**, and accounting for temporal averaging, the eddy convection velocity for any given scale and time can be calculated as

$$u_c(s_j, n) = \frac{1}{s_j} \sum_{n=\,n-s_j/2}^{n=n+s_j/2} \left(u_{res}(n) + \frac{\partial j \partial t^{1/2}}{C_\partial \psi_0(0)} \sum_{j=j}^{j=J} \frac{\Re\{W(s_j, n)\}}{s_j^{1/2}} \right), \quad 2.10$$

followed by substituting $u_c(s_j, n)$ into **equation 2.2** to derive the length-scales ($\lambda(s_j, n)$) for all values of $W(s_j, n)$.

The second factor that must be accounted for is changes in boundary layer thickness ($\delta_c(s_j, n)$); $\lambda(s_j, n)$ must be normalized with respect to $\delta_c(s_j, n)$ to ensure that a structure of a given relative size is consistently associated with either the turbulent or non-turbulent flow components. Given that the vertical velocity distribution of a turbidity current is similar to a wall-bounded jet flow (Kneller et al., 1997), the same definition of flow thickness is adopted here. As such, $\delta(n)$ is defined as the point above the high velocity core ($\tilde{u}_{max}(n)$) where the non-turbulent component of the flow ($\tilde{u}(n)$) is equal to $0.5\tilde{u}_{max}(n)$. Yet at this point in the analysis $\tilde{u}(n)$ and $u'(n)$ haven't been identified from the instantaneous velocity data. Consequently, we adopt an iterative approach to calculate a time-scale normalized value of boundary layer thickness ($\delta_c(s_j, n)$), which is defined as

$$\delta_c(s_j, n) = \frac{1}{s_j} \sum_{n=\,n-s_j/2}^{n=+n=s_j/2} \delta(n)\,, \quad 2.11$$

where $\delta(n)$ is instantaneous boundary layer thickness. Initially, $\delta(n)$ is set equal to the height of the flume (0.3 m) and all values of $W(s_j, n)$ where $\lambda(s_j, n)$ is less than 2.5δ (the choice of this threshold is discussed later in the text) are removed from the reconstruction to identify $\tilde{u}$. Subsequently, values of relative length-scale ($\frac{\lambda}{\delta_c}(s_j, n)$) are updated and the iteration is repeated until the mean difference of δ between two successive iterations is less than 0.75mm, which is equivalent to the spacing of neighbouring points in the velocity profile.

By definition, application of **equation 2.10** and **equation 2.11** to turbulent flows with temporally variable flow thicknesses inevitably results in unique values of $\frac{\lambda}{\delta_c}(s_j, n)$, hence the instantaneous values of $P\left(\frac{\lambda}{\delta_c}, n\right)$ must be grouped into unique categories of relative length-scale. As in **equation 2.4**, an inverse base 2 logarithmic transformation is used to define relative length-scale categories ($\frac{\lambda}{\delta_{c_k}}$), which emphasizes the spatial resolution of the smaller scale structures, and maintains consistency with the resolution and distribution of wavelet scales used in the transform, as defined by **equation 2.4**. Accordingly, the relative length-scale categories are defined as

$$\frac{\lambda}{\delta_{c_k}} = \frac{\lambda}{\delta_{c_o}} 2^{k\partial k}, \qquad k = 0,1, \ldots K \;, \qquad 2.12$$

where $\frac{\lambda}{\delta_{c_o}}$ and $\frac{\lambda}{\delta_{c_K}}$ are the smallest and largest relative length-scales obtained from the decomposition of $u(n)$, and ∂k is a user specified constant. Here we define K as being equal to J and ∂k as $\left(\frac{\lambda}{\delta_{c_K}} - \frac{\lambda}{\delta_{c_o}}\right)/J$ to maintain the same number of categories used in the decomposition. It is worth noting that for instantaneous spectra, the energy from multiple length-scales ($\frac{\lambda}{\delta_c}$) may be contained within a relative length-scale category ($\frac{\lambda}{\delta_{c_k}}$); accordingly, values of $\frac{\lambda}{\delta_c}$ are rounded to the nearest relative length-scale category ($\frac{\lambda}{\delta_{c_{k\prime}}}$), and instantaneous spectra in the $\frac{\lambda}{\delta_{c_k}}$ domain are defined as

$$P\left(\frac{\lambda}{\delta_{c_k}}\right) = \sum_{j=1}^{J} P\left(\frac{\lambda}{\delta_{c_{k\prime}}}, j\right), \qquad 2.13$$

where J is number of wavelet scales used in the CWT, and the mean spectrum for any arbitrary segment of the signal in the relative length-scale domain is

$$\bar{P}\left(\frac{\lambda}{\delta_{c_k}}\right) = \sum_{n=n_1}^{n_2} \frac{P(\frac{\lambda}{\delta_{c_k}}, n)}{n_2 - n_1 + 1}\ , \qquad 2.14$$

where $\bar{P}\left(\frac{\lambda}{\delta_{c_k}}\right)$ is the time-averaged spectrum in relative length scale domain. Thus it is possible to compare different points in the flow, and in the case of unsteady flows, the temporal evolution of turbulence at a point can be investigated by subtracting the mean spectra from $P(\frac{\lambda}{\delta_{c_k}}, n)$. More importantly, it allows the user to assess whether the distortions in frequency domain spectra are indicative of poor signal quality, or the result of length scale aliasing due to unsteady convective velocities. This is not possible if the temporal dependence of u_c is neglected, as per Taylor's hypothesis.

2.4. **Experimental setup**

A schematic of the experimental setup is shown in Figure 2-3, and consists of a 0.8 m^3 mixing tank suspended above a 0.3 m x 0.3 m x 7.06 m horizontal closed duct that at its downflow end opens into an oversized outlet tank. A gate in the outlet tank maintained a constant fluid level in the duct, which initially consisted of clear water that during the experiment became replaced by the turbid sediment suspension. At the beginning of each run a sediment-water suspension of a pre-determined sediment concentration was prepared in the mixing tank using a Lightnin™ industrial mixer, with propellers situated at 0.2 m and 0.8 m above the bottom of the tank. The slurry itself was composed of 150 μm sand using a sediment concentration of 1033 kg/m^3 (2% by volume) and vertical concentration profiles were measured in the tank using an optical backscatter sensor to verify the homogeneity of the slurry. An orifice valve at the base of the tank controlled the outflow rate, and in turn, the speed of the current in the duct. To begin a run a tight-fitting rubber stopper was abruptly removed from the vertical standpipe that connected the tank to the duct. Driven entirely by its own momentum, the turbid plume then flowed the length of the flat, horizontal duct, passing beneath the velocity profiler (see below). Displaced fluid in the duct drained over a spill gate in the outlet tank that also served to partition the tank into a wet section to maintain water levels in the flume, and a dry section to capture the excess fluid. A flow deflector was placed in the wet section of the outlet tank to prevent current reflection back into the flume and to minimize the development of an adverse pressure-gradient and back-flow.

Three-dimensional velocity data were collected using an ultrasonic Doppler velocimetry profiler (UDV3D) by Signal Processing SA. Like conventional acoustic velocimetry, the UDV3D relies on the coherent pulse pair technique to derive fluid velocity (Lhermitte & Serafin, 1984; Miller & Rochwarger, 1972; Zedel & Hay, 2002; Zedel et al., 1996). The principal advantage of this device over acoustic instrumentation used in conventional hydraulic studies is its relatively low operating frequency, which maximizes back-scatter intensity and minimizes viscous signal attenuation for the grain sizes used in this study (Thorne & Meral, 2008). Due to the reduced signal attenuation, the UDV3D is able to sample flows with high suspended sediment concentrations, thus making it ideally suited for measuring particle gravity currents. The instrument itself consists of a central emitter and three passive receivers, and probe geometry is manually configured for the given application. Because the flow structure of turbidity currents mimics that of wall-bounded jet flows, which means that the high velocity core is located towards the base rather than the top of the current, the probes were mounted to the top of the flume to minimize flow disturbances. Specifics on probe geometry are contained in Figure 2-3, and a summary of the sampling properties is provided in Table 2-1. Prior to measuring the experimental flow, emission power and reception sensitivity of the transducers were adjusted through an iterative process so that only particle laden fluid resulted in Doppler reflections; this was the only way to identify the arrival of the current head directly from the velocity data; however it also means we measured particle rather than fluid velocity. Although the experimental current lasted 45 seconds, the sampling duration was 90 seconds and was subsequently cropped from 10 seconds prior to the arrival of the head and 10 seconds after the passage of the tail. The extraneous portions at the beginning and end of the velocity data were maintained to minimize the cone of influence effects associated with the CWT.

Data treatment was limited to ensure that the UDV3D data had not been phase-wrapped. This occurs when particle speeds exceed the instrument's ambiguity velocity, resulting in false measurements. This issue is discussed in detail by Rennie and Hay (2010) who developed an algorithm to identify and correct corrupted velocity data; their method was applied to the current dataset, and corrupted measurements account for less than 0.1% of the total signal.

2.5. **Results**

The temporal evolution of the experimental sediment gravity current as it passes under the UVD3D is shown in Figure 2-4. The solid line near the base of the flow indicates the portion of the high velocity core ($\tilde{u}_{max}$), and the upper dashed line is where $\tilde{u} = \tilde{u}_{max}/2$, which by convention defines the boundary layer thickness (δ) in wall-bounded jet flows (Kneller et al., 1997). As a whole the flow is clearly unsteady but with a distinct longitudinal anatomy consisting of a rapidly accelerating, short-lived head, a quasi-steady body and a slowly decelerating tail; the body-tail transition is marked by a rapid reduction in flow speed. It is worth noting that, while the body is quasi-steady, the upper part of the flow shows large-scale, coherent pulsing motions most likely related to the passage of Kelvin-Helmholtz instabilities. The longitudinal anatomy of the current is consistent with results from previous studies (Kneller & Buckee, 2000). For example, $\tilde{u}_{max}$ is similarly located at ~0.25δ, and therefore consistent with the range of 0.2δ to 0.3δ often reported in earlier studies (Kneller & Buckee, 2000).

Unsteady flow poses two distinct challenges for traditional fluid turbulence analysis, especially the standard spectral normalization procedure for converting frequency to wave number domains. Firstly, the unsteadiness of the current suggests that the eddy convective velocity (u_c), responsible for transporting fluid turbulence, is similarly unsteady. Thus a given frequency band in conventional windowed spectral analysis comprises a range of eddy length scales rather than a single value. This, in turn, causes spectral flattening and the appearance of multiple peaks in spectral power at the transition between the Taylor (turbulent) and integral (non-turbulent) length scales (Del Álamo & Jiménez, 2009; Moin, 2009). Secondly, the boundary layer thickness (δ) also changes with time; since the maximum length scale associated with fluid turbulence typically scales with flow thickness, and accordingly potentially leads to further distortions of the power spectra. Together, these two factors suggest that the accuracy of conventional methods for deriving the power spectrum of a signal is compromised by the temporal variability (unsteadiness) of u_c and δ with respect to the window size. However, it should be possible to correct instantaneous spectra if one has prior knowledge of u_c and δ for all frequencies, and at all times.

To demonstrate the effects of not correcting for changes in u_c and δ in unsteady flows, Figure 2-5 presents the time-averaged spectral energy plots obtained via both the CWT and the Fast Fourier Transform (FFT) at four different heights above the bed (h ≅0.02, 0.05, 0.1, 0.20 m). It is important to note that the signal used to perform the CWT contained an additional 223 instantaneous measurements beyond the start and end points shown in Figure 2-4; this is far greater than the largest scale (s_J) used in the CWT (194 instantaneous measurements). The padding from either end of the record was subsequently omitted from the analysis and, therefore, the spectra presented herein are not affected by the low confidence issues that typically plague the lower frequencies at the beginning and end of the signal in CWT's. In all cases, beam velocities (Beam 2) are presented rather than Cartesian velocities to minimize the propagation of numerical errors associated with the UDV's velocity resolution. A line depicting a -5/3rds slope associated with the Taylor frequencies has been added to demonstrate the deviation between the theoretical and observed slopes. In general, there is good agreement between the spectral energy distributions obtained from the two techniques, although the CWT method produces a much smoother distribution, especially at higher frequencies, which is consistent with previous observations (Torrence & Compo, 1998). In terms of assessing net signal quality, both result in slopes that deviate towards the high frequencies, particularly in measurements at the base and the top of the current, which suggests that the signal is contaminated by instrument noise (e.g. Rennie and Hay (2010)). Yet as will be demonstrated in the ensuing time-space transformation, spectral flattening at the top of the current results from aliasing due to changes in u_c and, therefore, spectral flattening in the near bed measurements is a by-product of how suspended sediments are distributed through the water column. The larger issue, however, is related to the low frequencies because in highly unsteady flows substantial energy is added to the low-frequency end of the spectrum. This causes the slope break associated with the integral time-scale in steady flows to be obscured, and therein the need for the sprectra to be first converted from frequency to length-scale domains in order to differentiate between turbulent and non-turbulent motions in unsteady flows as the former scales with δ.

Figure 2-6 presents the time-frequency matrices of δ_c and u_c at the four sample heights as calculated by **Equation 2.11** and **Equation 2.10**, respectively, and demonstrates the time-frequency dependency of u_c and δ_c. A spatial Nyquist filter was applied to the CWT results so that values of $W_n(s_j)$ with length scales less than the sample volume thickness along the u_c axis were omitted from the reconstruction. For any given frequency, eddy convective velocities generally decrease between the body and the tail of the current, and with distance from u_{max}, which is consistent with the flow field trends in Figure 2-4. Accordingly, instantaneous spectra from low velocity regions should undergo whole-scale shifts towards shorter length scales, and hence higher wave numbers. Importantly, variations in u_c are not limited to temporal effects associated with highly unsteady flows, but also vary across the frequency band for instantaneous spectra; higher frequencies display a distinct pulsing motion that is absent in the lower frequency range. This is related to the degree of spatial averaging used across the frequency band and demonstrates that conversion from frequency to wave-number domains requires correction for both spectral translation and contraction/dilation effects resulting from narrowing/spreading of the spectra. In general, temporal variation of u_c in the high frequency bands is greater compared to the low frequency bands, which results in larger errors in the estimation of eddy length scales in this frequency range if temporal effects are neglected. Also noteworthy is that the values of $\overline{u_c}$ and $\overline{\delta_c}$ are largely invariant for the frequencies used in the CWT, and are identical to the values of $\bar{u}$ and $\bar{\delta}$ in all but the lowest frequencies; we believe this deviation to be an artifact of the local moving average window, which extends beyond the record limits shown in Figure 2-4, where flow is relatively quiescent. Though these finding contradict those of Del Álamo and Jiménez (2009) on scale dependency of u_c, where the mean convection rate of large and small structures are approximated by the bulk flow velocity and local mean, respectively, it does validate Taylor's hypothesis insofar as $\bar{u}$ can be used to approximate u_c in a statistical sense. However, errors in the length-scale estimates of discrete fluid structures will be high if local signal variance is substantial. Moreover, it suggests that all conversions from time-scale to length-scale domains via Taylor's hypothesis are prone to error unless flows are steady with low turbulence intensity, as per Taylor's original constraints for use of the frozen field hypothesis.

In the absence of time-frequency dependency, u_c can truly be equated to $\bar{u}$ and therefore the shape of spectral energy distributions in length scale domains will be identical to that in frequency space, which clearly is not the case in the present study (Figure 2-6). Figure 2-7 presents the instantaneous spectra from the CWT after they have been converted to length-scale domain, and the resulting mean spectral energy distribution; for comparative purposes, the time-averaged spectra shown in Figure 2-5 have been converted to the length-scale domain using $\bar{u}$ and $\bar{\delta}$ as surrogates for u_c and δ_c, respectively. Clearly the time-frequency dependency of u_c and δ_c modify instantaneous spectra in two distinct ways: 1) spectral shift, and 2) spectral range. Spectral shift results from temporal variations of u_c, and causes a wholesale shift in all frequencies at a given point in time towards shorter or longer length-scales. As such, these shifts are manifestations of temporal dependency, and typically are associated with unsteadiness in the flow field. Conversely, changes in spectral range result from the frequency dependence of u_c at a given point in time, and cause the range of length-scales associated with an instantaneous spectrum to vary. Consequently, these effects are the manifestation of frequency dependency, and are associated with fluid turbulence. In general, spectral shifting is most apparent towards the beginning and end of the current as the entire flow field experiences large accelerations associated with the arrival of the head and the transition between the body and the tail of the current. Variations in spectral range increase with distance from the bed since the reduction in $\bar{u}$ outpaces the reduction in u', thereby increasing the time-frequency dependence of u_c. The culmination of these shift and range effects can be seen in the time-averaged spectra. In general, the near bed spectra show good agreement with those converted using Taylor's hypothesis, although accounting for the temporal and frequency dependency of u_c and δ_c produce smoother spectra with sharper drops in energy at the limits of the spectral range. Given that Figure 2-6 demonstrates $\bar{u}_c$ for a given frequency is equivalent to $\bar{u}$, this similarity was expected and serves to validate the technique presented herein. However, deviations between $u_c(s_j, n)$ and $\bar{u}$ are large, leading to inaccurate length-scale estimates from timeseries velocity data. This is highly problematic for studies attempting to investigate discrete coherent fluid structures.

In terms of spectral normalization, it is worth noting that the length scale associated with the peak in spectral energy is remarkably consistent in all but the upper sampling position (h = 0.195m), where the peak is shifted towards shorter length scales. We believe this is the result of their locations with respect to δ; the three lower positions are located within the boundary layer, hence the similarity between length-scales associated with peaks in spectral energy (Figure 2-4). The upper position is located above the top of the current and therefore should scale with some other presumably smaller variable, such as the distance between δ and the top of the flume. Of particular interest are the vertical trends associated with the smaller/higher frequency structures.

Whereas the uppermost sampling location displays a linear slope between the spectral peak and the smallest structures, towards the bed the shorter length scales show a shallower slope than that predicted by Kolmogorov's theory. Additionally, the point of deviation shifts towards larger structures with decreasing distance to u_{max}. Although this can partly be attributed to the increase in velocity, and therefore u_c towards the bed in wall bounded jet flows, it may also be attributed to increased turbulence dampening related to higher amounts of suspended sediment. Numerous studies have shown that suspended sediments can dampen turbulence, even at relatively low concentrations (Baas & Best, 2002; Geyer, 1993; Graf & Cellino, 2002). Therefore the increased dampening of higher frequencies near the bed may also be attributed to the very nature of sediment distributions in density currents, which following the Rouse equation increase exponentially towards the bed (Garcia, 1994).

2.6. **Discussion**

Since the seminal work of Kline et al. (1967), there has been a mounting push away from describing turbulence in a purely statistical sense, and towards quantifying the properties of coherent fluid structures. Initially focusing on the near wall region with the burst-sweep phenomenon, consisting of slow and high speed fluid packets, respectively, it is now accepted that even steady flows contain coherent fluid structures whose scales are much longer than those associated with inner region fluid turbulence and may play a fundamental role in linking inner and outer region flow processes (Marusic et al., 2010). Regardless of scale, all these features are described as being either high or low speed, thus by definition are advected at different rates, and therefore there is always a temporal dependency associated with u_c.

The need to scale the speed of different fluid structures is not limited to understanding hydraulic processes operating within the flow, but also applies to linkages between turbulent boundary layers, sediment transport and bedform development. Incipient motion studies have demonstrated that the size and associated time duration of a coherent fluid structure is just as important as its intensity for initiation of sediment transport (Diplas et al., 2008). Unfortunately, the near boundary regions in open channel flows correspond with the areas of highest turbulence intensities and, therefore, the least suitable places to invoke Taylor’s hypothesis. Similarly, mounting evidence suggests that bedform development is linked with hydrodynamic instabilities rather than scales of motion associated with fluid turbulence (Paola et al., 1989; Venditti et al., 2006; Venditti et al., 2005). Thus there is also a clear need to quantify length-scales to link bedforms to flow structures, and to identify the proper datum to make the distinction between turbulent and non-turbulent motions, neither of which is possible via Taylor's hypothesis or Reynolds decomposition, respectively. The following section is included to demonstrate the individual and cumulative error in estimates of λ/δ if one neglects the time-frequency dependency of the relevant terms.

In most conventional geophysical flows, the largest source of error in estimating λ/δ is in the derivation of u_c. Assuming that spatial accelerations are negligible, the instantaneous error in length-scale estimates for any given coherent fluid structure due to neglecting the time-frequency dependence of u_c ($\sigma_{u_c}(s_j, n)$) can be can be evaluated by

$$\sigma_{u_c}(s_j, n) = \left(\bar{u}(n) - u_c(s_j, n)\right)/u_c(s_j, n), \qquad 2.15$$

and the mean error associated with any scale ($\sigma_{u_c}(s_j)$) over a given block of the signal ($n_2 - n_1$) is

$$\sigma_{u_c}(s_j) = \frac{1}{n_2 - n_1 + 1} \sum_{n=n_1}^{n=n_2} \sqrt{\sigma_{u_c}(s_j, n)^2}\,. \qquad 2.16$$

Thus the error should be small in steady or weakly unsteady flows with low turbulence intensities, and grow progressively larger as the velocity fluctuations associated with $\tilde{u}$ and u' increase with respect to $\bar{u}$.

The second term responsible for errors in estimates of λ/δ is boundary layer thickness (δ). In open channel flows, changes in boundary layer thickness are small with respect to $\bar{\delta}$ and their influence on λ/δ are negligible in the absence of large changes in discharge or the migration of substantial bedforms such as dunes during the measurement period. Yet due to the large Kelvin-Helmholtz instabilities generated at the interface of density currents and the overlying ambient fluid, there can be a substantial temporal dependency in the value of u_c. As with **equation 2.15**, this secondary source of error in estimates of λ/δ due to the time-scale dependency of δ_c ($\sigma_{\delta_c}(s_j, n)$) can be quantified by

$$\sigma_{\delta_c}(s_j,n) = \left(\bar{\delta}(n) - \delta_c(s_j,n)\right)/\delta_c(s_j,n)\,, \qquad 2.17$$

and the mean error associated with a given scale ($\sigma_{\delta_c}(s_j)$) over a fixed block of the signal ($n_2 - n_1$) is

$$\sigma_{\delta_c}(s_j) = \frac{1}{n_2 - n_1 + 1}\sum_{n=n_1}^{n=n_2}\sqrt{\sigma_{\delta_c}(s_j,n)^2}\,. \qquad 2.18$$

It is worth noting errors in u_c and δ_c are not necessarily independent, thus the root sum of the squares of the mean error values is not used to estimate total error. Rather, the total error was evaluated directly from errors in relative length scale λ_c/δ_c, where estimated length scale λ_c represents u_c/f

$$\sigma_{(\lambda/\delta)_c}(s_j,n) = \left(\frac{\bar{\lambda}(n)}{\bar{\delta}(n)} - \frac{\lambda_c(s_j,n)}{\delta_c(s_j,n)}\right)\Big/\left(\frac{\lambda_c(s_j,n)}{\delta_c(s_j,n)}\right), \qquad 2.19$$

and the mean total error for a given scale ($\sigma_{(\lambda/\delta)_c}(s_j)$) over a fixed block of the signal ($n_2 - n_1$) is

$$\sigma_{(\lambda/\delta)_c}(s_j) = \frac{1}{n_2 - n_1 + 1}\sum_{n=n_1}^{n=n_2}\sqrt{\sigma_{(\lambda/\delta)_c}(s_j,n)^2}\,. \qquad 2.20$$

Since the experimental flow used in the present study is highly unsteady in terms of its velocity and boundary layer thickness, it is anticipated that the differences in relative length scale estimates between Taylor's approach and the technique presented here will be large. The natural extension of Taylor's approach to unsteady flows would to be to use $\tilde{u}(n)$ and $\delta(n)$ instead of $\bar{u}$ and $\bar{\delta}$ as estimates of $u_c(s_j,n)$ and $\delta_c(s_j,n)$, respectively. It is important to recall that these quantities cannot be obtained without first converting the spectral energy distributions from frequency to length scale domains to identify the turbulent and non-turbulent components of the flow, yet they can replace the time-averaged terms in **equations 2.15**, **2.17** and **2.19** to assess how much error is associated with the frequency and local running average dependency of $u_c(s_j,n)$ and $\delta_c(s_j,n)$.

Figure 2-8 presents $\sigma(s_j)$, the mean error in estimates of λ/δ, for each of the Fourier frequencies of the CWT using the steady ($\bar{u}$) and unsteady ($\tilde{u}$) values of u_c and δ_c versus the present estimates $u_c(s_j, n)$ and $\delta_c(s_j, n)$. In both cases, the total time-frequency averaged error in relative length scale increases from approximately 14.7% and 5.7% near the bed to 396.1% and 28.6% at the uppermost point used in the analysis, for the steady and unsteady cases, respectively. In general, the increase in error towards the top of the flow is related to the overall trend of increased relative magnitude of velocity fluctuations with bed distance in wall-bounded jet flows. Lower error in the unsteady case is anticipated as it is able to capture some of the temporal dependency associated with $u_c(s_j, n)$ and $\delta_c(s_j, n)$,. In a steady flow, most of the total error can be attributed to difference in the approximation of u_c; $\sigma_{u_c}(s_j)$ is uniform across all frequencies in the near bed region, but substantial errors develop with increasing distance from the bed, initially appearing in the higher frequencies but eventually encompassing the entire frequency band. It is useful to recall that $u_c(s_j, n)$ is estimated by taking the local mean after removing the high frequency component of the signal, and that by definition of the CWT, the time-averaged value for any unique Fourier frequency is zero. As such, $\bar{u}_c(s_j)$ is very closely approximated by $\bar{u}$ and the changes in error patterns between the bottom and the top of the current must be related completely to differences in the intensity of the local velocity fluctuations ($\sqrt{\overline{(u(t) - \bar{u})^2}}/\bar{u}$). In the near bed region where flow speeds in turbidity currents are highest, these fluctuations are small with respect to $\bar{u}$ resulting in low values of $\sigma_{u_c}(s_j)$, and the uniformity of $\sigma_{u_c}(s_j)$ for all frequencies; this suggests the intensity of the relative fluctuations associated with the non-turbulent component of flow are of the same order of magnitude as those attributed to fluid turbulence. Further up at $h \cong 0.10$ m, larger error is seen in the higher Fourier frequencies, and probably stems from two sources related to the velocity and concentration characteristics of turbidity currents. First, it has been shown in quasi-steady density flows that $\partial\bar{u}/\partial h$ decreases away from the bed at a higher rate than the amplitude of the higher frequency velocity fluctuations, leading to high dimensionless turbulent kinetic energies (e.g. Leeder et al., 2005) hence relative turbulence intensities, which is in direct violation of one of the principal assumptions of Taylor's hypothesis. Second, sediment concentration in density currents increase exponentially towards the bed (Garcia, 1994), and numerous studies have established that the presence of suspended sediments can suppress turbulent velocity fluctuations, even at very low concentrations (Baas & Best, 2008). The effects of suspended sediments are modelled as an additional viscous term in numerical simulations (Zeng & Lowe, 1997) and therefore the effects of turbulence dampening are especially pronounced in the higher frequencies. Although not verifiable at present, this dampening may also contribute to the larger error in the higher frequencies between $h \cong 0.05$ m and $h \cong 0.10$ m in our experimental current. At the uppermost point, $\sigma_{u_c}(s_j)$ is large across all Fourier frequencies, and, given the measurement position with respect to δ (Figure 2-4), the larger error in the lower frequencies is related to the passage of intense Kelvin-Helmholtz instabilities generated at the interface between the current and overlying ambient fluid.

In the case that accounts for the time but not the frequency dependency of u_c and δ_c (i.e., unsteady ($\tilde{u}$) values of u_c and δ_c), a threshold of λ/δ = 2 was used to isolate $\tilde{u}$ and u'. This value was chosen due to the difficulty in identifying the integral length scale due to the large amount of variance associated with the unsteady component of flow. However, it is consistent with the integral length scales reported in numerous turbulent geophysical flows once normalized to boundary layer thickness (Robinson, 1991). A sensitivity analysis on the threshold choice is presented later in this section. Although the patterns in $\sigma_{u_c}(s_j)$ across the frequency band are similar to those obtained using Taylor's hypothesis, errors in u_c steadily decrease and reach a minimum in the frequency band slightly higher than that associated with the threshold between the turbulent and non-turbulent components of the flow. Presumably this is a direct result of minimizing the difference between the frequencies used to reconstruct the signal in **equation 2.10** (prior to time averaging for obtaining u_c) and those used to isolate $\tilde{u}$. It is worth recalling that in normalized length-scale-based filtering, a given value of λ/δ is actually composed of a range of frequencies due to local velocity fluctuations in the flow, and that the mean frequency associated with λ/δ shifts to lower values with increasing distance from the high velocity core, which is consistent with an upward decrease in $\bar{u}$. Consequently, the non-turbulent component of the signal appears to undergo an increasing degree of smoothing between the bottom and top of the flow when plotted in the time domain with length scale filtering.

In contrast to $\sigma_{u_c}(s_j)$, errors in boundary layer thickness ($\sigma_{\delta_c}(s_j)$) are relatively low since the intensity of fluctuations in $\delta(n)$ with respect to $\bar{\delta}$ are considerably lower than those in the velocity signals. Additionally, $\sigma_{\delta_c}(s_j)$ is constant with depth, and the error steadily increases from low to high frequencies in the time-averaged ($\bar{\delta}$), whereas the trend is reversed in the temporally variable scenario. This is largely attributed to how $\delta(n)$ and consequently $\delta_c(s_j, n)$ are derived. Whereas $u_c(s_j, n)$ is calculated directly from a unique velocity signal at a given height above the bed, $\delta(n)$ depends solely on the point where $\tilde{u}(n) = \tilde{u}_{max}(n)/2$, and therefore varies temporally. Nevertheless λ/δ is constant for any given point in an instantaneous velocity profile. Subsequently, $\delta_c(s_j, n)$ is derived from $\delta(n)$ by applying a moving average with a span equivalent to the duration of s_j. Thus by definition, $\sigma_{\delta_c}(s_j)$ must decrease towards the low end of the frequency band since the span of the moving average covers a progressively larger portion of the total signal duration, thereby minimizing the difference between $\delta_c(s_j, n)$ and $\bar{\delta}$. Conversely, the error must decrease towards the high end of the frequency band in the unsteady scenario since progressively smaller moving average spans minimize the difference between $\delta_c(s_j, n)$ and $\delta(n)$.

As previously mentioned, the values of $u_c(s_j, n)$ are derived from the raw velocity signal, and therefore independent of the value of λ/δ used to identify $\tilde{u}$ and u'. Thus in turbulent flows with a constant boundary layer thickness, the technique outlined herein provides a robust means of generating temporally variable and frequency dependent estimates of u_c, and therefore relative length scales. Yet in the case of wall bounded jet flows where $\delta(n)$ is not equivalent to $\bar{\delta}$, this is not necessarily the case as $\delta(n)$ is dependent on $\tilde{u}$; as such, unique values of $\lambda/\delta\ (s_j, n)$ are themselves threshold dependent, which can potentially modify the shape of mean spectral energy distributions. If so, this has important implications for turbulence analysis because it has the potential to shift the value of λ/δ associated with the integral length scale, and therefore the very parameter used to define the scales of motions associated with turbulence versus those associated with the unsteady, non-turbulent component of the flow.

Figure 2-9 presents the results of a sensitivity analysis on the effect of threshold choice on the error estimates of λ/δ, the resulting mean spectral energy distributions in the spatial domain, and the relative error versus the values obtained using a threshold of $\lambda/\delta = 2$. Here, we present the sensitivity results at only $h \cong 0.10$m, although similar trends were also noted at the other measurement points. Irrespective of threshold choice, $\sigma_{u_c}(s_j)$ is low across the frequency band, though there is a general trend of larger values of $\sigma_{u_c}(s_j)$ towards the higher frequencies. This is largely a by-product of how $\delta_c(s_j, n)$ is derived; using smaller values of λ/δ (i.e. higher frequencies) to isolate $\tilde{u}$ increases the temporal variability in boundary layer thickness. Recalling that $\delta_c(s_j, n)$ is calculated by taking the length-scale dependent local average, much of the temporal variability in δ is removed in all but the smallest structures, suggesting a limited influence of threshold choice on estimates of relative length scale. This is further reflected in the spectral energy distribution; the highest errors in spectral energy are associated with the smallest structures and given that these sizes contain the least amount of energy, the net effect of these errors is minimal. Thus the shape of spectral energy distributions is largely independent of threshold choice used to define boundary layer thickness provided that $\left(\delta(n) - \bar{\delta}\right)/\bar{\delta} \ll (u(n) - \bar{u})/\bar{u}$, and that the length scales most susceptible to error are much shorter than those associated with the integral length scale. However the choice of threshold obviously determines the amount of signal variance associated with $\tilde{u}$ versus u'. While this topic is beyond the scope of the present study, it warrants consideration because it has important implications for interpreting the role of coherent fluid structures and potentially redefining the role of turbulence in fluid-particle interactions. This is the case not just for unsteady flows, but also for what are traditionally considered to be steady flows, in which all velocity fluctuations about the time averaged value are associated with turbulence, irrespective of scale.

Velocity signatures from density flows contain large coherent pulsing motions whose scales are much larger than that associated with fluid turbulence (Best et al., 2005). If the intensity of these pulsing motions $\sqrt{\overline{(\tilde{u} - \bar{u})^2}}/\bar{u}$ is of the same order of magnitude as those associated with fluid turbulence ($\sqrt{u'^2}/\tilde{u}$), it can add a substantial amount of energy to the non-turbulent range of the spectra, potentially obscuring the value of λ/δ associated with the integral length scale. This is problematic as improper characterization of the threshold defining the transition between unsteady, non-turbulent motions versus those truly associated with fluid turbulence can lead to gross misrepresentations of even the most basic turbulence parameters like turbulence intensity, turbulent kinetic energy and the Reynolds stress. Given that the integral length scales occupy a relatively narrow range of sizes when normalized against boundary layer thickness in an array of different geophysical flows, and with the recent advent of velocity profilers that can sample over long distances with very high spatial resolutions, such as the UDV3D used here, we strongly advocate the use of a single value of λ/δ to define the threshold between turbulent and non-turbulent motions. The benefit of this approach is that it provides a consistent means of assigning fluid structures of a given size to the turbulent or the unsteady, non-turbulent component of flow, and not just at a single measurement height, but the entire flow field. Consequently, it eliminates user variability (and the tedium) in manually specifying the integral length scale for each vertical point in the velocity profile, and at the same time ensures that flow properties from different points in the profile are directly comparable. Additionally, it provides a non-dimensionalized statistic for cross-comparing the results from other studies. However, the methodology presented here has larger implications for the study of geophysical flows fields beyond quantifying length-scaled and dynamic signal filtering.

In reality, no geophysical flows are truly steady, as all are affected by fluctuations across a range of time-scales, including annual floods in fluvial systems and daily tidal fluctuations in estuaries. Furthermore, very-large coherent fluid structures (VLCS's), or structures much larger that those associated with turbulence, have been identified in steady flows (Nikora, 2007). These VLCS's scale with, and possibly control planform geometry characteristics (Marquis & Roy, 2011). Thus the validity of assumed stationarity in geophysical flows is entirely dependent on the magnitude of signal variation associated with long-timescale variability with respect to the magnitude of short scale fluctuations within the sampling window. If the magnitude of long-timescale variability is high, the conventional approach is to analyze small segments of the signal where flow can be considered steady (Rennie & Hay, 2010; Walter et al., 2011), and traditional assumptions such as Taylor's hypothesis and Reynolds decomposition are generally valid. The downside to this approach is that it limits the lowest frequency structures that can be identifed and restricts analysis to steady flow conditions. Thus the true strength of the technique outlined herein is that it circumvents the need to break signals into smaller, quasi-steady segments, and therein makes it possible to study both larger-scale phenomena and systems undergoing changing flow conditions. More germane to the present work, is that the proposed method removes our reliance on Reynolds decomposition for isolating fluid turbulence for all geophysical flows. Further, since it provides a means of accounting for the time-frequency dependency of u_c and dynamic filtering properties, it should greatly improve the ability to quantify length-scales in the near boundary area. These regions of wall bounded geophysical shear flows, much like the tops of jet flows where relative velocity fluctuation intensity increases as mean flow speeds approach zero, are where Taylor's hypothesis is most likely to fail. Thus, the proposed method should aid in further developing the linkages between fluid boundary layer characteristics and sediment transport and bedform development.

2.7. **Conclusion**

It is well known that turbulence, or more specifically coherent fluid structures, play a fundamental role in sediment transport dynamics and the morphological characteristics of the bed in steady, open channel flows. Yet few studies have investigated the turbulence characteristics of turbidity currents beyond basic time-averaged parameters, and as a consequence the fluid particle dynamics that govern these flows remain poorly understood. In part, this gap can be attributed to the difficulties associated with performing basic steps for analyzing turbulence, such as identifying the turbulent and non-turbulent components in instantaneous velocity data, in these inherently unsteady flows.

Numerous studies have demonstrated that the largest eddies associated with turbulence scale with boundary layer thickness, and given that a spectral frequency contains a range of distinct length-scales, conventional frequency filtering cannot provide a consistent basis for isolating turbulence in highly unsteady flows. To deal with this issue, we have used the Continuous Wavelet Transform (CWT) in a novel way to derive the eddy convection velocity for all frequencies used in the CWT and at all points of time in the velocity signal. The basic premise is that the convective velocity (u_c) of an eddy with a given time scale (i.e. frequency) is equal to its local mean velocity once all the higher frequencies have been removed from the signal. This information allows for length-scale based filtering to identify the turbulent and non-turbulent components of the flow, thus ensuring that coherent fluid motions of a given size are always associated with either the turbulent (u') or the non-turbulent ($\tilde{u}$) component of flow. The power of this approach is that it can analyze the entire signal rather than small segments, thus allowing the study of larger scale phenomena.

The technique for estimating u_c presented herein offers two key advantages over Taylor's "frozen turbulence" hypothesis. First, it is the only approach to our knowledge that can account for both the frequency and temporal dependence of u_c; thus it is not only suitable for application in highly unsteady flows, but also can account for temporal fluctuations in u_c associated with high turbulence intensities in steady flows, which is the primary factor that can invalidate Taylor's hypothesis. Second, it requires no prior knowledge of the properties associated with the non-turbulent component of flow; rather, u_c is calculated directly from the instantaneous time series velocity data. Our results show the mean difference between u_c and both $\tilde{u}$ and $\bar{u}$ for most spectral frequencies are very small, however the instantaneous differences are substantial, which causes large errors in the estimated length of individual coherent structures. In light of this, and the widely reported instances of a single Fourier frequency containing a spectrum of unique length-scales even in steady flows, it seems that it is more appropriate to assume that coherent fluid structures are frozen over their duration rather than the entire measurement period as per Taylor's frozen turbulence hypothesis. Furthermore, since our approach also accounts for turbulence in estimating u_c, it is free of the low-turbulence intensity constraint of Taylor's hypothesis, and therefore may be better suited for near-wall regions of turbulent flows

Although the results presented in this study are encouraging, it was not possible to verify the estimated length-scales directly due to the nature of the experimental setup, and the current itself. As such, we strongly encourage future studies with complete spatio-temporal datasets to test the reliability of this novel approach for estimating u_c in both steady and unsteady turbulent flows. Finally, we would like to offer a word of caution regarding the use of Reynolds decomposition to isolate turbulence in steady flows, particularly in studies focusing on discrete turbulent structures that utilize velocity data collected over an extended period of time; recent studies suggest that the non-turbulent component of the flow may in fact be mildly unsteady, and not accounting for this may bias apparent directions of motion, and even simple parameters such as the time-averaged Reynolds stress.

2.8. **References**

Adamowski, K., Prokoph, A., & Adamowski, J. (2009). Development of a new method of wavelet aided trend detection and estimation. *Hydrological Processes, 23*(18), 2686-2696. doi: 10.1002/Hyp.7260

Baas, J. H., & Best, J. L. (2002). Turbulence modulation in clay-rich sediment-laden flows and some implications for sediment deposition. *Journal of Sedimentary Research, 72*(3), 336-340. doi: 10.1306/120601720336

Baas, J. H., & Best, J. L. (2008). The dynamics of turbulent, transitional and laminar clay-laden flow over a fixed current ripple. *Sedimentology, 55*(3), 635-666. doi: 10.1111/j.1365-3091.2007.00916.x

Best, J. L., Kostaschuk, R. A., Peakall, J., Villard, P. V., & Franklin, M. (2005). Whole flow field dynamics and velocity pulsing within natural sediment-laden underflows. *Geology, 33*(10), 765-768. doi: 10.1130/G21516.1

Bouma, A. H. (1962). *Sedimentology of some flysch deposits: a graphic approach to facies interpretation*. Amsterdam: Elsevier.

Buxton, O. R. H., de Kat, R., & Ganapathisubramani, B. (2013). The convection of large and intermediate scale fluctuations in a turbulent mixing layer. *Physics of Fluids, 25*(12), 125105. doi: 10.1063/1.4837555

Choux, C. M. A., Baas, J. H., McCaffrey, W. D., & Haughton, P. D. W. (2005). Comparison of spatio–temporal evolution of experimental particulate gravity flows at two different initial concentrations, based on velocity, grain size and density data. *Sedimentary Geology, 179*(1-2), 49-69. doi: 10.1016/j.sedgeo.2005.04.010

Del Álamo, J. C., & Jiménez, J. (2009). Estimation of turbulent convection velocities and corrections to Taylor's approximation. *Journal of Fluid Mechanics, 640*, 5-26. doi: 10.1017/s0022112009991029

Diplas, P., Dancey, C. L., Celik, A. O., Valyrakis, M., Greer, K., & Akar, T. (2008). The role of impulse on the initiation of particle movement under turbulent flow conditions. *Science, 322*(5902), 717-720. doi: 10.1126/science.1158954

Farge, M. (1992). Wavelet Transforms and Their Applications to Turbulence. *Annual Review of Fluid Mechanics, 24*(1), 395-457. doi: 10.1146/annurev.fluid.24.1.395

Fisher, M. J., & Davies, P. O. A. (1964). Correlation Measurements in a Non-Frozen Pattern of Turbulence. *Journal of Fluid Mechanics, 18*(1), 97-116. doi: 10.1017/S0022112064000076

French, J. R., & Clifford, N. J. (1992). Characteristics and 'event-structure' of near-bed turbulence in a macrotidal saltmarsh channel. *Estuarine, Coastal and Shelf Science, 34*(1), 49-69. doi: 10.1016/s0272-7714(05)80126-x

Garcia, M. H. (1994). Depositional Turbidity Currents Laden with Poorly Sorted Sediment. *Journal of Hydraulic Engineering-Asce, 120*(11), 1240-1263. doi: 10.1061/(Asce)0733-9429

Geyer, W. R. (1993). The Importance of Suppression of Turbulence by Stratification on the Estuarine Turbidity Maximum. *Estuaries, 16*(1), 113-125. doi: 10.2307/1352769

Graf, W. H., & Cellino, M. (2002). Suspension flows in open channels; experimental study. *Journal of Hydraulic Research, 40*(4), 435-447. doi: 10.1080/00221680209499886

Grass, A. J. (1971). Structural Features of Turbulent Flow over Smooth and Rough Boundaries. *Journal of Fluid Mechanics, 50*(2), 233-255. doi: 10.1017/S0022112071002556

Gray, T. E., Alexander, J., & Leeder, M. R. (2005). Quantifying velocity and turbulence structure in depositing sustained turbidity currents across breaks in slope. *Sedimentology, 52*(3), 467-488. doi: 10.1111/j.1365-3091.2005.00705.x

Heathershaw, A. E. (1975). *Measurements of turbulence near the sea-bed using electromagnetic current meters.* Paper presented at the Proceedings of IEEE Conference on Instrumentation in Oceanography.

Higgins, C. W., Froidevaux, M., Simeonov, V., Vercauteren, N., Barry, C., & Parlange, M. B. (2012). The Effect of Scale on the Applicability of Taylor's Frozen Turbulence Hypothesis in the Atmospheric Boundary Layer. *Boundary-Layer Meteorology, 143*(2), 379-391. doi: 10.1007/s10546-012-9701-1

Khripounoff, A., Vangriesheim, A., Babonneau, N., Crassous, P., Dennielou, B., & Savoye, B. (2003). Direct observation of intense turbidity current activity in the Zaire submarine valley at 4000 m water depth. *Marine Geology, 194*(3-4), 151-158. doi: 10.1016/S0025-3227(02)00677-1

Kline, S. J., Reynolds, W. C., Schraub, F. A., & Runstadler, P. W. (1967). The structure of turbulent boundary layers. *Journal of Fluid Mechanics, 30*(4), 741-773. doi: 10.1017/s0022112067001740

Kneller, B., & Buckee, C. (2000). The structure and fluid mechanics of turbidity currents: a review of some recent studies and their geological implications. *Sedimentology, 47,* 62-94. doi: 10.1046/j.1365-3091.2000.047s1062.x

Kneller, B. C., Bennett, S. J., & McCaffrey, W. D. (1997). Velocity and turbulence structure of density currents and internal solitary waves: potential sediment transport and the formation of wave ripples in deep water. *Sedimentary Geology, 112*(3-4), 235-250. doi: 10.1016/S0037-0738(97)00031-6

Kolmogorov, A. N. (1991). The Local-Structure of Turbulence in Incompressible Viscous-Fluid for Very Large Reynolds-Numbers. *Proceedings of the Royal Society of London Series a-Mathematical Physical and Engineering Sciences, 434*(1890), 9-13. doi: 10.1098/rspa.1991.0075

Krogstad, P. A., Kaspersen, J. H., & Rimestad, S. (1998). Convection velocities in a turbulent boundary layer. *Physics of Fluids, 10*(4), 949-957. doi: 10.1063/1.869617

Leclair, S. F., & Arnott, R. W. C. (2005). Parallel lamination formed by high-density turbidity currents. *Journal of Sedimentary Research, 75*(1), 1-5. doi: 10.2110/Jsr.2005.001

Leeder, M. R., Gray, T. E., & Alexander, J. (2005). Sediment suspension dynamics and a new criterion for the maintenance of turbulent suspensions. *Sedimentology, 52*(4), 683-691. doi: 10.1111/j.1365-3091.2005.00720.x

LeHew, J., Guala, M., & McKeon, B. (2010). A Study of Convection Velocities in a Zero Pressure Gradient Turbulent Boundary Layer *40th Fluid Dynamics Conference and Exhibit*: American Institute of Aeronautics and Astronautics.

Lhermitte, R., & Serafin, R. (1984). Pulse-to-Pulse Coherent Doppler Sonar Signal Processing Techniques. *Journal of Atmospheric and Oceanic Technology, 1*(4), 293-308. doi: 10.1175/1520-0426(1984)001<0293:ptpcds>2.0.co;2

Lumley, J. L. (1965). Interpretation of Time Spectra Measured in High-Intensity Shear Flows. *Physics of Fluids, 8*(6), 1056-1062. doi: 10.1063/1.1761355

Marquis, G. A., & Roy, A. G. (2011). Bridging the gap between turbulence and larger scales of flow motions in rivers. *Earth Surface Processes and Landforms, 36*(4), 563-568. doi: 10.1002/Esp.2131

Marusic, I., Mathis, R., & Hutchins, N. (2010). Predictive model for wall-bounded turbulent flow. *Science, 329*(5988), 193-196. doi: 10.1126/science.1188765

Meyers, S. D., Kelly, B. G., & Obrien, J. J. (1993). An Introduction to Wavelet Analysis in Oceanography and Meteorology - with Application to the Dispersion of Yanai Waves. *Monthly Weather Review, 121*(10), 2858-2866. doi: 10.1175/1520-0493(1993)121<2858:Aitwai>2.0.Co;2

Miller, K., & Rochwarger, M. (1972). A covariance approach to spectral moment estimation. *IEEE Transactions on Information Theory, 18*(5), 588-596. doi: 10.1109/tit.1972.1054886

Moin, P. (2009). Revisiting Taylor's hypothesis. *Journal of Fluid Mechanics, 640*, 1-4. doi: 10.1017/s0022112009992126

Nezu, I., & Nakagawa, H. (1993). *Turbulence in Open-Channel Flows*: A.A. Balkema.

Nikora, V. (2007). 3 Hydrodynamics of gravel-bed rivers: scale issues. In H. Habersack, H. Piégay & R. Massimo (Eds.), *Developments in Earth Surface Processes: Gravel-bed Rivers VI, From Process Understanding to River Restoration* (pp. 61–81). Amsterdam: Elsevier.

Paola, C., Wiele, S. M., & Reinhart, M. A. (1989). Upper-Regime Parallel Lamination as the Result of Turbulent Sediment Transport and Low-Amplitude Bed Forms. *Sedimentology, 36*(1), 47-59. doi: 10.1111/j.1365-3091.1989.tb00819.x

Raffel, M., Willert, C. E., Wereley, S. T., & Kompenhans , J. (2007). *Particle Image Velocimetry: A Practical Guide*: Springer Berlin Heidelberg.

Rennie, C. D., & Hay, A. (2010). Reynolds Stress Estimates in a Tidal Channel from Phase-Wrapped ADV Data. *Journal of Coastal Research, 26*(1), 157-166. doi: 10.2112/08-1090.1

Reynolds, O. (1895). On the Dynamical Theory of Incompressible Viscous Fluids and the Determination of the Criterion. *Philosophical Transactions of the Royal Society A: Mathematical, Physical and Engineering Sciences, 186*, 123-164. doi: 10.1098/rsta.1895.0004

Richardson, L. F. (1922). Weather prediction by numerical process. *Quarterly Journal of the Royal Meteorological Society, 48*(203), 282-284. doi: 10.1002/qj.49704820311

Robinson, S. K. (1991). Coherent Motions in the Turbulent Boundary-Layer. *Annual Review of Fluid Mechanics, 23*, 601-639. doi: 10.1146/annurev.fluid.23.1.601

Soulsby, R. L. (1977). Similarity Scaling of Turbulence Spectra in Marine and Atmospheric Boundary-Layers. *Journal of Physical Oceanography, 7*(6), 934-937. doi: 10.1175/1520-0485(1977)007<0934:Ssotsi>2.0.Co;2

Taylor, G. I. (1938). The spectrum of turbulence. *Proceedings of the Royal Society of London Series a-Mathematical and Physical Sciences, 164*(A919), 0476-0490. doi: 10.1098/rspa.1938.0032

Thorne, P. D., & Meral, R. (2008). Formulations for the scattering properties of suspended sandy sediments for use in the application of acoustics to sediment transport processes. *Continental Shelf Research, 28*(2), 309-317. doi: 10.1016/j.csr.2007.08.002

Torrence, C., & Compo, G. P. (1998). A practical guide to wavelet analysis. *Bulletin of the American Meteorological Society, 79*(1), 61-78. doi: 10.1175/1520-0477(1998)079<0061:Apgtwa>2.0.Co;2

Venditti, J. G., Church, M., & Bennett, S. J. (2006). On interfacial instability as a cause of transverse subcritical bed forms. *Water Resources Research, 42*(7). doi:10.1029/2005wr004346

Venditti, J. G., Church, M. A., & Bennett, S. J. (2005). Bed form initiation from a flat sand bed. *Journal of Geophysical Research-Earth Surface, 110*(F1). doi:10.1029/2004jf000149

Walter, R. K., Nidzieko, N. J., & Monismith, S. G. (2011). Similarity scaling of turbulence spectra and cospectra in a shallow tidal flow. *Journal of Geophysical Research-Oceans, 116*(C10). doi: 10.1029/2011jc007144

Wills, J. A. B. (1964). On Convection Velocities in Turbulent Shear Flows. *Journal of Fluid Mechanics, 20*(3), 417-432. doi: 10.1017/S002211206400132x

Zaman, K. B. M. Q., & Hussain, A. K. M. F. (1981). Taylor Hypothesis and Large-Scale Coherent Structures. *Journal of Fluid Mechanics, 112*(Nov), 379-396. doi: 10.1017/S0022112081000463

Zedel, L., & Hay, A. E. (2002). A three-component bistatic coherent Doppler velocity profiler: Error sensitivity and system accuracy. *Ieee Journal of Oceanic Engineering*, *27*(3), 717-725. doi: 10.1109/Joe.2002.1040953

Zedel, L., Hay, A. E., Cabrera, R., & Lohrmann, A. (1996). Performance of a single-beam pulse-to-pulse coherent Doppler profiler. *Ieee Journal of Oceanic Engineering*, *21*(3), 290-297. doi: 10.1109/48.508159

Zeng, J., & Lowe, D. R. (1997). Numerical simulation of turbidity current flow and sedimentation: I. Theory. *Sedimentology*, *44*(1), 67-84. doi: 10.1111/j.1365-3091.1997.tb00424.x

2.9. **List of Figures**

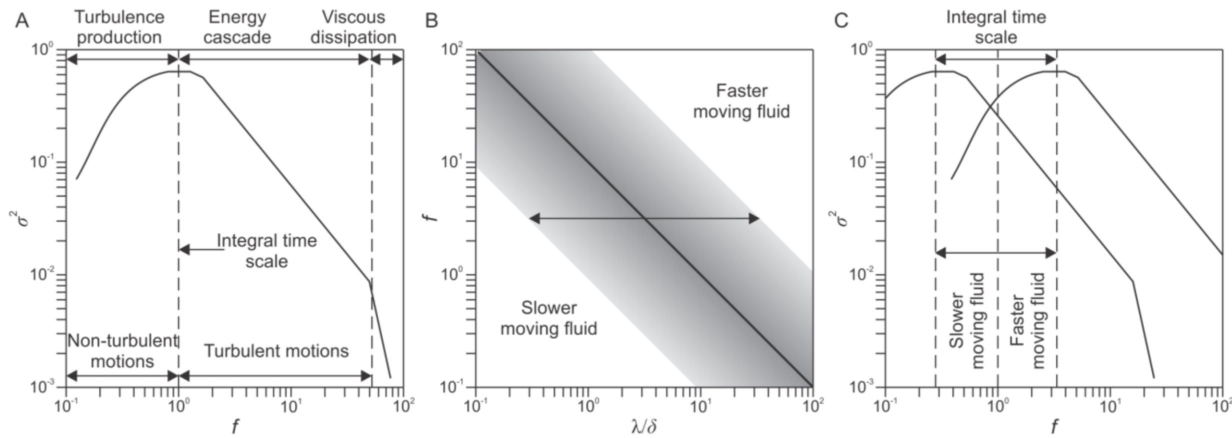

Figure 2-1: (A) Idealized schematic of the energy spectra spectrum in turbulent flow illustrating the change in signal variance (σ^2) with frequency (f) associated with the turbulence production (non-turbulent motions), the energy cascade (turbulent motions), and viscous dissipation (non-turbulent motions) time scales. The integral time scale defines the frequency associated with the transitions between turbulent and non-turbulent motions, and is used in high-pass filters to isolate the frequencies associated with fluid turbulence. The steep drop in σ^2 in the viscous dissipation region is the result of converting the flow's kinetic energy into heat. (B) The effect of changes in u_c on resulting Fourier frequency for a given length scale (λ) normalized with respect to boundary layer thickness (δ), and (C) the resulting spectral displacement associated with changes in u_c. Unsteady flows will have a temporally varying integral time scale that can only be corrected by converting instantaneous spectra from temporal to spatial domains prior to time-averaging.

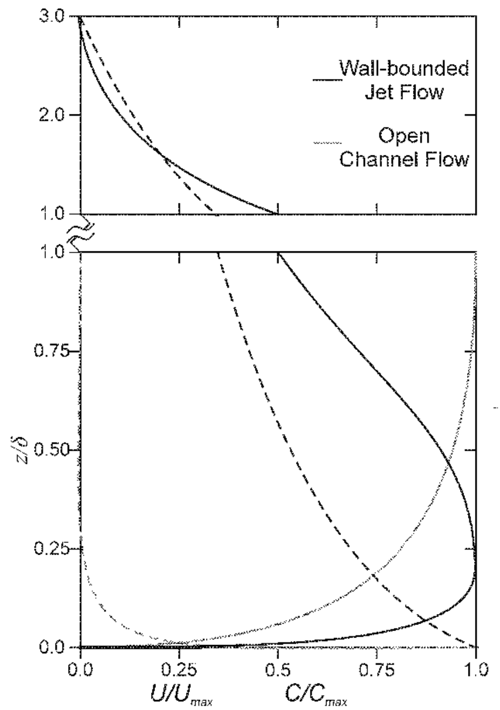

Figure 2-2: Typical velocity (solid) and concentration (dashed) profiles for turbidity currents (black) and open channel flow (grey).

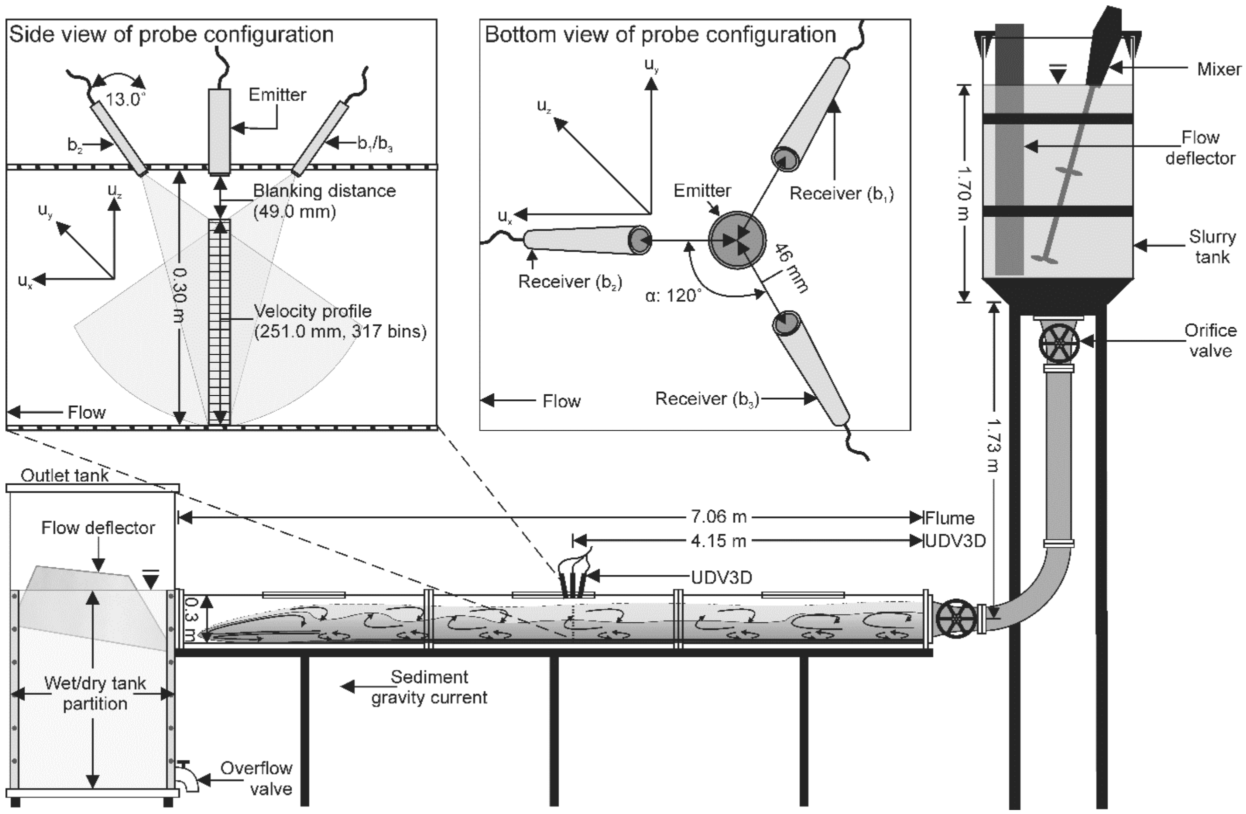

Figure 2-3: Schematic of the experimental setup used to create sediment gravity currents and the probe configuration of the UDV3D.

Table 2-1: Summary of UDV3D's sampling characteristics.

Operating frequency (f_o)	2 MHz
Pulse repetition frequency (τ^{-1})	792 Hz
Emitter diameter	10 mm
Emitter beam angle	5.2º
Receiver diameter	5 mm
Receiver beam angle	9.6º
Pulse-pairs per sample	36
Sampling frequency (τ^{-1})	22.1 Hz
Ambiguity velocity ($u_{b_{amb}}$)	$1.43 \cdot 10^{-1}\, m/s$
Velocity resolution ($u_{b_{res}}$)	$1.11 \cdot 10^{-3}\, m/s$
Sample volume thickness	1.5 mm

Sample volume diameter	30-55 mm

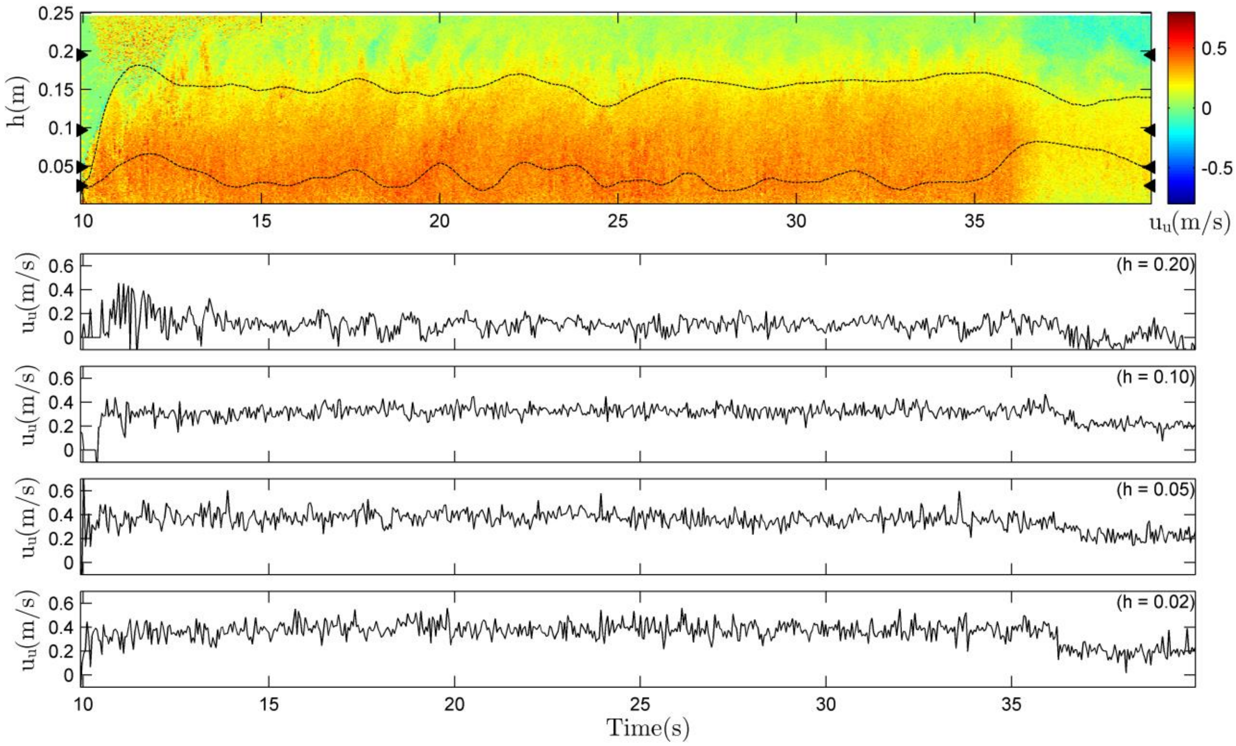

Figure 2-4: Temporal evolution of the experimental current's downstream velocity component as it passes under the UDV3D (top). The lower dashed line near the base of the flow indicates the location of the high velocity core ($\tilde{u}_{max}$), and the upper dashed line is where $\tilde{u} = \tilde{u}_{max}/2$, which defines the boundary layer thickness (δ) in wall-bounded jet flows. The triangles mark the positions of the four vertical points used in the subsequent analysis, and their individual signals are shown below.

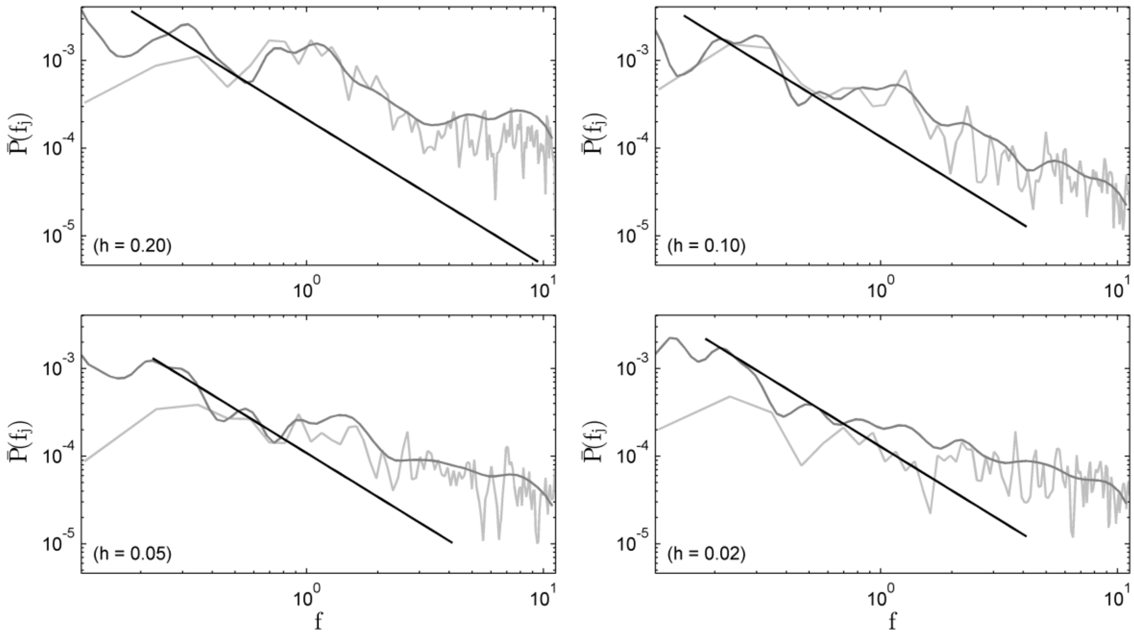

Figure 2-5: Comparison of spectral energy distributions in the frequency (f) domain obtained from the continuous wavelet (dark grey) and Fourier (light grey) transforms at four different heights (h) above the bed, without accounting for temporal and frequency variations in u_c ($h \cong 0.036\ m$) and δ_c ($h \cong 0.148\ m$). For the sake of clarity, only the spectra for beam 2 are presented, though similar results are obtained from beams 1 and 3. A line with a slope of -5/3 (black) is included to show the anticipated slope associated with Kolmogorov's energy cascade.

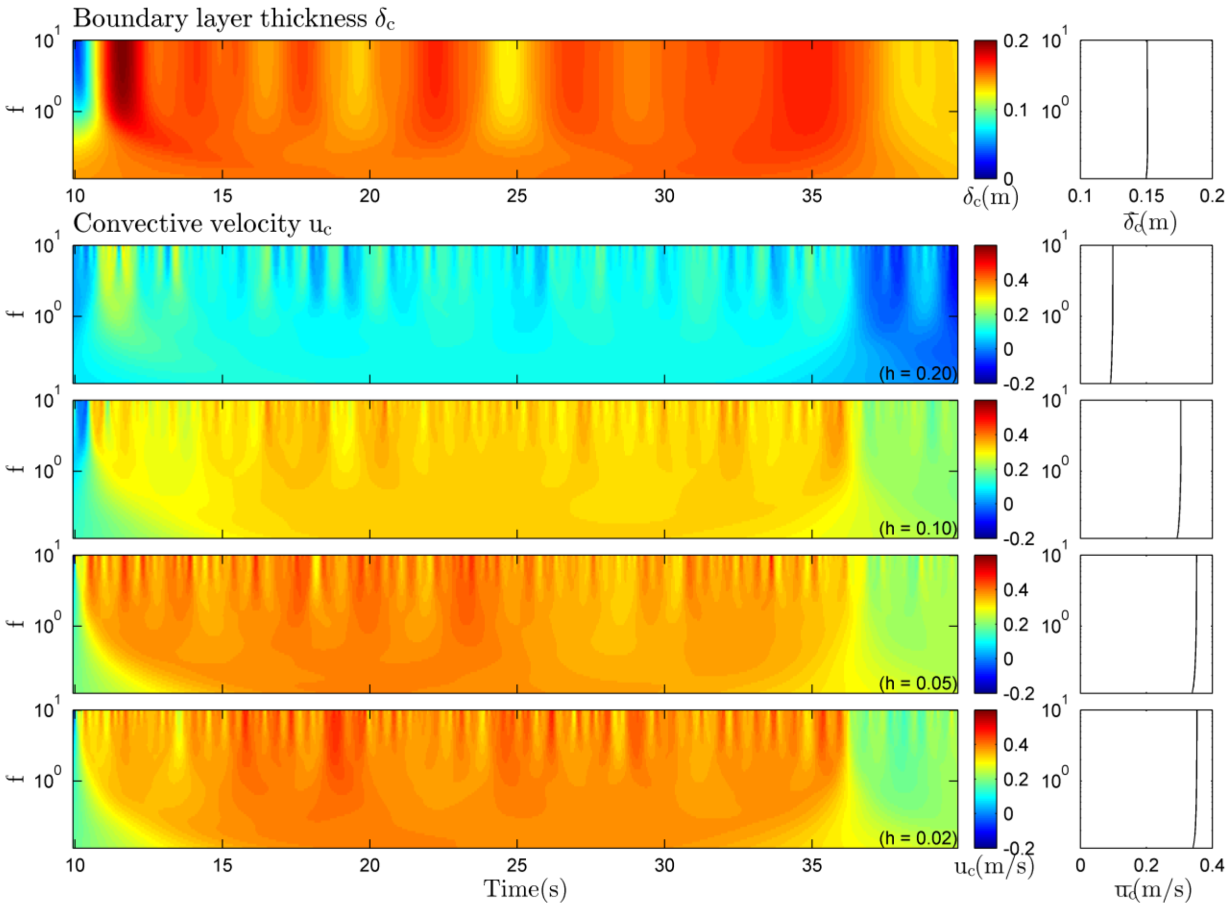

Figure 2-6: Time-frequency matrix of estimated values of δ_c (top) and u_c at the four heights above the bed. The higher frequencies display distinct pulsing motions whereas the lower frequencies show more gradual oscillations; these are artifacts that reflect the turbulent and non-turbulent components contributions to u_c, respectively, and have a substantial impact on normalized length scale (δ/λ) estimates Note that the time-averaged values of $\overline{\delta_c}$ and $\overline{u_c}$ (right) are virtually identical in all but the lowest frequencies, and equivalent to $\bar{\delta}$ and $\bar{u}$, respectively.

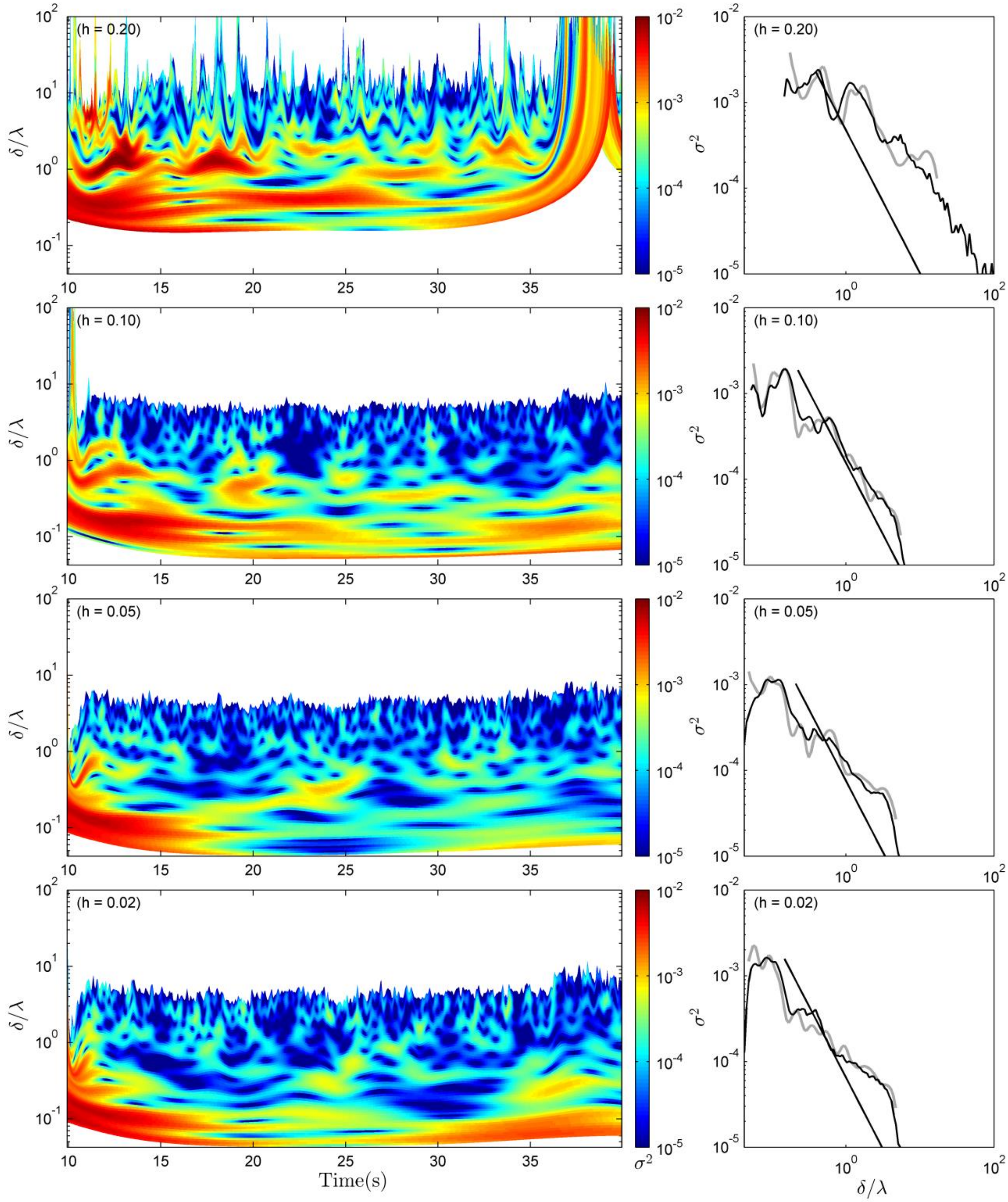

Figure 2-7: Instantaneous (left) and time-averaged (right) wavelet spectra in the normalized length scale domain (δ/λ) for beam 2 at the same four heights above the bed after correcting for temporal and frequency variations in u_c and δ_c. To compare the effects of accounting for

temporal and frequency variations of u_c and δ_c the time-averaged frequency-domain spectra presented in Figure 2-5 have been converted to normalized length-scale domain by using $\bar{u}$ and $\bar{\delta}$ as surrogates for u_c and δ_c, respectively (grey). A line with a slope of -5/3 (dashed) is included to show the anticipated slope associated with Kolomogov's energy cascade. Note that the time-frequency dependence of u_c and δ_c, increases with bed distance. Towards the bed, the spectral energy slope shallows with respect to Kolmogorov's cascade theory for the smaller scale structures, which we interpret to result from increased suspended sediment concentrations, hence turbulence dampening, rather than signal contamination.

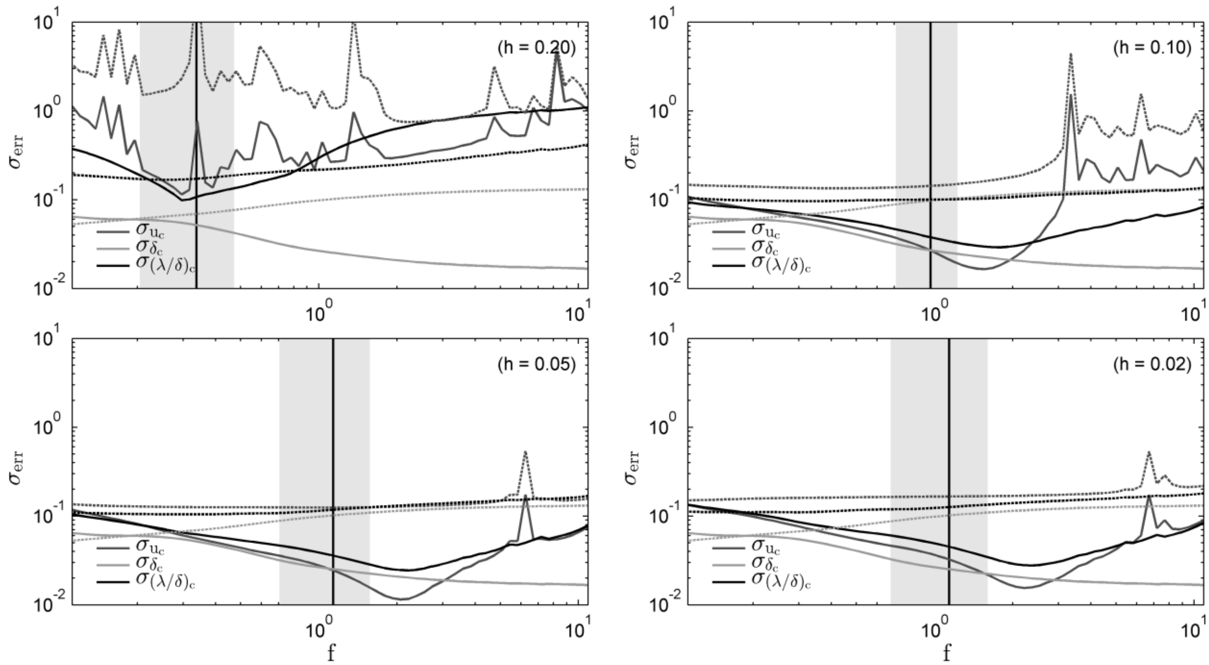

Figure 2-8: Mean error in estimates of δ/λ (black), and the amount of error associated with u_c (dark grey) and δ_c (light grey) for either Taylor's hypothesis (i.e. $u_c = \bar{u}$; $\delta_c = \bar{\delta}$; dashed) or the non-turbulent component of flow (i.e. $u_c = \tilde{u}$; $\delta_c = \tilde{\delta}$; solid) versus the technique presented herein that accounts for the time-frequency dependence of u_c and δ_c. The shaded region represents the range of frequencies corresponding to the choice of threshold to identify the turbulent and non-turbulent components of flow, and corresponds with the region where error is minimized. Recall that prior knowledge of u_c and δ_c for all times and frequencies is needed to identify $\tilde{u}$ and $\tilde{\delta}$.

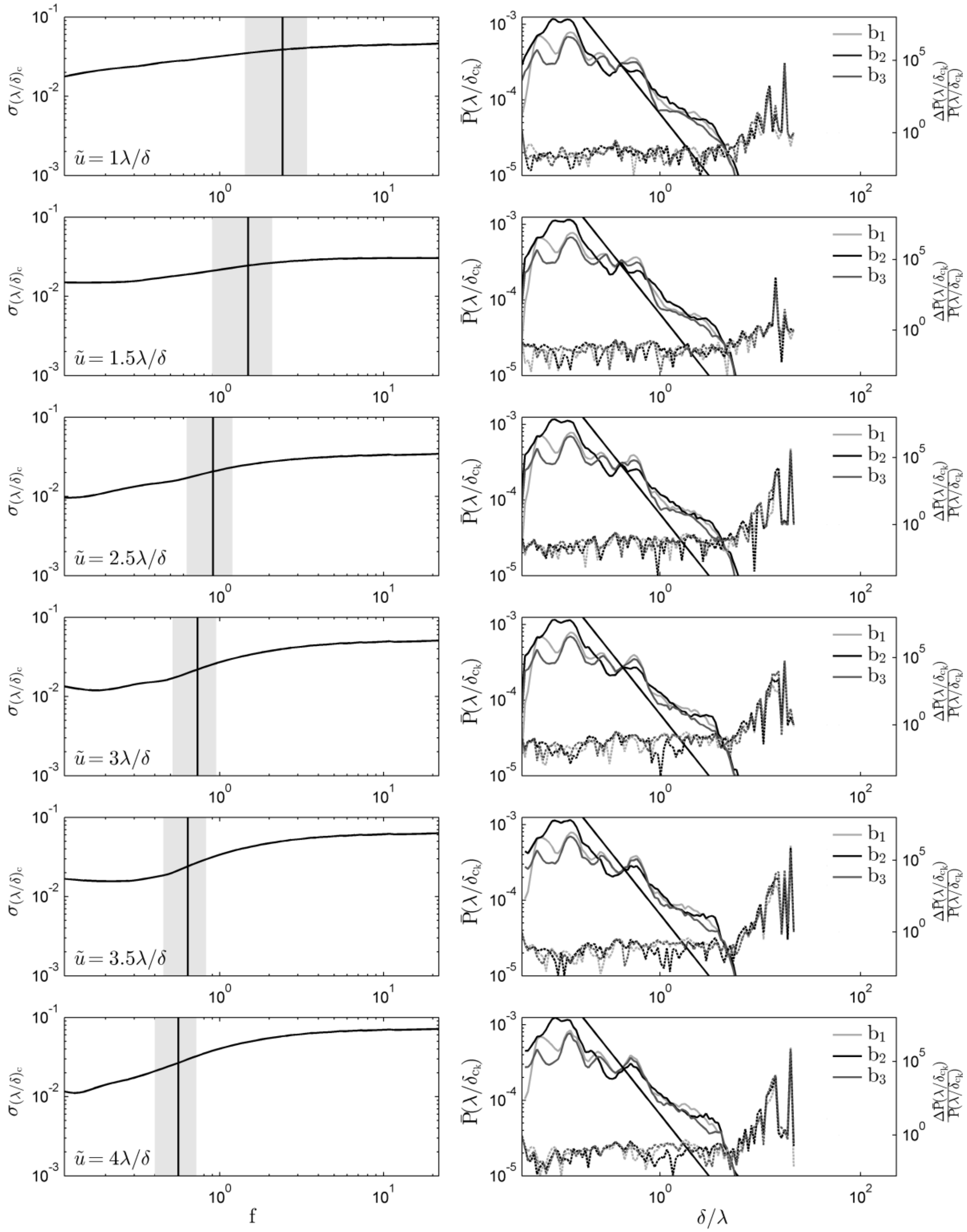

Figure 2-9: The effect of threshold choice used to isolate $\tilde{u}$ and derive $\tilde{\delta}$, and the resulting error ($\bar{\lambda}_{err}(s_j)$) on estimates of δ/λ and the time-averaged spectrum in the δ/λ domain ($\bar{P}\left(\frac{\lambda}{\delta_{c_k}}\right)$) at

$h \cong 0.10$m; errors are relative to the values of $\delta_c(s_j, n)$and $\bar{P}\left(\frac{\lambda}{\delta c_k}\right)$ using a threshold of λ/δ = 2. In both cases, errors are small and limited to the high frequency/small scale structures.

CHAPTER 3: THE INFLUENCE OF GRAIN SIZE ON THE VELOCITY AND SEDIMENT CONCENTRATION PROFILES AND DEPOSITIONAL RECORD OF TURBIDITY CURRENTS

M. Tilston[1], R.W.C. Arnott[1], C.D. Rennie[2] and B. Long[3]

[1]Department of Earth Sciences, University of Ottawa, Ottawa ON

[2]Department of Civil Engineering, University of Ottawa, Ottawa ON

[3] Centre Eau Terre Environnement, INRS, Québec City QC

3.1. **Abstract**

Cross-stratification formed by migrating dunes is ubiquitous in fluvial channel deposits, it is comparatively uncommon in channel deposits on the ocean floor, the reasons for which is the subject of much debate. In part, this is related to the difficulty associated with acquiring high resolution datasets; natural turbidity currents are highly destructive, whereas physical models are hampered by the short-comings of conventional laboratory instrumentation. Consequently the internal structure of turbidity currents is poorly understood, thus hindering the ability to identify the linkages between flow properties and depositional characteristics. In this study we use a medical grade Computed Tomography (CT) scanner coupled with a three-dimensional ultrasonic Doppler velocity profiler (UDVP-3D) to characterize the flow field and depositional morphology across a range of grain sizes (D_{50}: 70 -330 µm) and concentrations (5-17.5% by mass). Results show that the development of angular bedforms is suppressed in all flows with particle concentrations greater than 9.5% by mass, but notably also in all flows with particles less than 230 µm and sediment concentrations down to at least 5% by mass. This suggests a first order control on the response of the bed to the make-up of the overriding current. More fundamentally, we propose that grain size controls the character of near-bed density stratification, which is a requisite condition to generate the hydrodynamic instabilities that create the initial bed defects, which then lead to the development of angular bedforms like ripples and dunes.

Keywords: bed morphology, turbidites, cross-stratification, concentration profiles, grain size.

3.2. **Introduction**

Turbidity currents, like open channel flows, are unidirectional. But unlike open channel flows, turbidity currents are propelled by gravity acting directly on the suspended sediment and the interstitial fluid is entrained by the particles to form the current. Yet under low to no grade conditions such as on the basin floor, turbidity currents will decelerate and eventually come to rest. Since net deposition occurs during the waning phase of these currents, their deposits (turbidites) exhibit a suite of sedimentological features that, stratigraphically upward, suggest progressively lower energy conditions. Such patterns were first popularized by Bouma (1962) who described distinctively upward-fining beds with a consistent vertical assemblage of depositional characteristics. Notably absent in this idealized succession, however, is dune cross-stratification, which, based on the open channel flow literature should occur above upper plane bed and below ripples in bed sediment between ~0.2-0.7 mm (cf. Southard & Boguchwal, 1990). The absence of dune cross-stratification in the Bouma model, and its paucity in the ancient or modern deep-marine sedimentary records as a whole, has been noted by numerous authors and remains the subject of a long-standing debate.

Previous explanations for the absence of dunes in turbidites have focused on the requisite bed configuration and hydraulic conditions needed for their development, including insufficient growth time (Walker, 1965), the negative influence of suspended sediment-fallout (Lowe, 1988), the negative impact of turbulence suppression associated with higher suspended sediment concentrations (Allen & Leeder, 1980; Lowe, 1988), the negative effect of clay content on flow structure and/or bed rheology (Baas & Best, 2002; Schindler et al., 2015).

Recently, both laboratory experiments (Baas, 1994; Cartigny et al., 2013) and direct observations in submarine canyons (Talling, 2013; Xu et al., 2014) have shown that turbidity currents are commonly supercritical, whereas in open channel flows ripples and dunes form under subcritical conditions; thus their absence results from the unique velocity and concentration profiles of density currents (Parker et al., 2013). However, experimental work has also confirmed the presence of downstream migrating angular bedforms that are dimensionally similar to dunes in supercritical flow (Sequeiros et al., 2010a); thus the Froude number may not be a good predictor of bed morphology in turbidity currents.

Another possible explanation for the lack of angular bedforms relates to the average horizontal distance travelled by a sediment particle before it settles to the bed, which is lnown as the advection length (Ganti et al., 2014). Here, the particle's advection length sets the size of the smallest morphologic features that can form, suggesting that coarser sediments are more likely to create smaller features, hence there is a distinct grain size control in turbidite morphology.

Finally, Arnott (2012) suggested that the lack of dunes might be related to the flow lacking a sufficiently well developed near-bed hydrodynamic instability needed for (angular) bed form initiation and subsequent growth. However, this explanation lacked experimental verification. The objective here, then, is to report on a set of novel experiments that continuously measured the velocity, but more importantly, density within depositional sediment-driven turbidity currents, and to link those characteristics to the ensuing bed morphology. In doing so these data test the relationship between bed form development and the hydraulic state of the flow, in addition to elucidating sediment concentration profiles near the bottom of suspended-sediment-driven turbidity currents

3.3. **Experimental methods**

Experimental currents were created in a horizontal, 7 m long acrylic closed-topped flume with inner cross-sectional dimensions of 0.3 × 0.3 m. Initial sediment slurries were homogenized in a 0.8 m^3 cylindrical mixing tank suspended 1.87 m above the flume with an orifice valve at the base of the mixing tank to control outflow rates. During each run velocity and sediment concentration data were collected continuously 4 m downstream of the flume inlet in order to permit full flow development and maximize measurement duration. Profiles of velocity were recorded with ~1.5 mm vertical resolution at 22 Hz using a three-dimensional ultrasonic Doppler velocity profiler (UDVP-3D). Direct density measurements were collected using a medical grade Computed Tomography (CT)-scanner as 360º cross-sectional, 512 × 512 pixel images of the flow. Image reconstruction was constrained to the cross-sectional area of the flume, making each pixel about 0.6 × 0.6 mm. This combination of equipment offers the advantages of being non-obtrusive, minimal offset in sampling position of the two flow properties, and yields datasets with very high spatial and temporal resolution.

A total of 12 experimental currents were run using four different, well-sorted grain size distributions of Ottawa sand and three different concentrations. A summary of the experimental current properties and the resulting bed morphologies is provided in Table 3-1. For brevity, detailed analysis is limited to the 150 μm and 230 μm runs with concentrations of 9.5% by mass.

3.4. **Results**

In general, runs were fully turbulent, supercritical and consistent in character with those reported in previous studies (e.g. Kneller & Buckee, 2000); namely the arrival of the current head was marked by an abrupt increase in flow speed, followed by a slightly faster, quasi-steady body with an abrupt decrease in velocity in the current tail, and well developed Kelvin-Helmholtz instabilities were present along the top of the currents. Depth and time averaged flow properties were controlled by initial slurry mass, whereas depositional morphology was controlled by both concentration and grain size.

The aggraded bed was either planar or covered entirely with small-scale, downstream migrating bedforms (Figure 3-1a). In the case of the former, video analysis showed a slight lag between the arrival of the current head and the onset of deposition, after which deposition was constant throughout the body. Millimeter-high, ephemeral sand mounds formed that lacked a consistent spacing and downstream-migration pattern, suggesting they result from non-uniform transport and deposition associated with flow pulsing (Best et al., 2005) rather than sand waves linked with the formation of upper-stage plane bed in rivers (Bennett et al., 1998). No evidence of these sand mounds was visible on the surface of the final bed deposit. In the case of the downstream migrating bedforms, deposition was similar to plane bed runs for the first 8 s, after which short, equally spaced bed defects spontaneously appeared everywhere along the bed, that then migrated downstream and grew to a height of several millimeters in only a few seconds (Figure 3-1b). Presumably the lag between the arrival of the head and their development is attributed to the currents initially being issued onto the Plexiglas base of the flume rather than a pre-existing sand deposit, which is needed for angular bedform development. Notably, these bed features have wavelengths and heights of 70 mm and 5 mm, respectively, and thus are dimensionally similar to two-dimensional current ripples (Baas, 1994).

Intriguingly, grain size exerts a clear control on bed morphology. Irrespective of grain size, all runs with initial concentrations of 17.5% by mass resulted in a planar deposit; significantly, ripples or dunes would dominate the bed morphology at these flow speeds, depths and grain sizes in open channel flows (e.g.: Southard, 1991) and particle advection lengths (Ganti et al., 2014). As such, the planar bedding observed in these experiments is interpreted to be the byproduct of excessive suspended particle concentrations. With decreasing sediment concentration, here the 9.5% and 5% currents, grain size begins to exert a profound effect on bed morphology. Again, based on flow speed and advection length, ripples would dominate in open channel flows, yet despite having almost identical depth and time-averaged hydraulic characteristics, the coarser grained runs consistently produced downstream migrating bedforms, whereas a plane bed formed in the finer grained flows. Accordingly, the disparity in bed response may be related to how sediment is distributed within the flow.

Figure 3-2 presents a temporal volumetric reconstruction of current density, cut longitudinally through the center of the flume for the two runs, one with 150 µm sand and the other with 230 µm sand. Also included is the ratio between boundary shear stress $\left(\tau_0 = \rho\left(\kappa z \frac{du}{dz}\right)^2\right)$, and critical shear stress $(\tau_c = \theta_c(\rho_s - \rho)gd_{50})$, where ρ is current density, κ is Von Karmen's constant, z is flow thickness $(u(z) = u_{max}/2)$, du/dz is the vertical velocity gradient, θ_c is Shields theta, ρ_s is sediment density, g is gravitational acceleration, and d_{50} is mean particle diameter. In both cases, τ_0/τ_c values are generally orders of magnitude greater than unity, suggesting general bedload transport rather than incipient motion conditions. However, the way sediment is distributed through the water column differs significantly between the two runs. Whereas the 230 µm run is characterized by a highly concentrated basal layer, above which is a dramatic decrease in suspended sediment concentration, the 150 µm run shows a more gradual upward decrease in suspended sediment concentration. Note that the region of low shear coincides with the position of the high velocity core.

3.5. **Discussion**

Although common in turbidity current deposits, cross-stratification, especially formed by dunes, is much more pervasive in fluvial deposits, the reasons for which are unclear. Six hypotheses have been proposed to explain this disparity: 1) turbulence suppression (e.g., Allen & Leeder,

1980) 2) insufficient development time (Walker, 1965), 3) excessive sedimentation rates (Lowe, 1988), 4) hydraulic state of the flow (Sequeiros et al., 2010b), 5) particle advection length scales (Ganti et al., 2014), 6) bed rheology (e.g., Baas & Best, 2002). However, these hypotheses are inconsistent with observations presented here since 1) all flows were fully turbulent (see Re_d in Table 3-1), 2) downstream migrating bedforms developed in a matter of seconds (see Figure 3-1b, 3) sedimentation rates were higher in the coarser grained currents that did form bedforms, 4) all flows were supercritical through the current body, but produced two distinct bed states (see bed morphology and Fr_d in Table 3-1), 5) advection length scales fell within the regime for angular bedforms, 6) the bed is cohesionless. What is apparent is that grain size has a profound effect on the density structure of the currents, which in turn controls the final bed configuration.

Figure 3-3 presents the time-averaged velocity and concentration profiles for the 9.5% and 17.5% runs. Here, three important trends are associated with decreasing grain size. First, compared to coarse grained flows ($d_{50} \geq 230$ μm), u_{max} in the fine grained flows ($d_{50} \leq 150$ μm) is positioned higher above the static bed, therefore a lower vertical velocity gradient, resulting in less internal shear and related mixing. Second, the fine grained flows are significantly less stratified; presumably, lower shear in the fine grained flow is offset by reduced particle settling and increased particle interactions associated with the higher number of particles and surface area to volume ratios. Thirdly, angular bedforms only developed in the coarser grained flows at concentrations up to 9.5% by mass, whereas at higher concentration, and more importantly in all of the fine grained runs down to concentrations of at least 5% by mass, a plane bed formed. These differences indicate that angular bedform development is controlled by both sediment concentration and grain size as both these parameters alter the vertical density structure of the flow; whereas fine-grained flows show a quasi-linear decrease in sediment concentration away from the bed, coarse-grained flows display a dense basal layer, which thickens with concentration, and is overlain by a much more dilute region of flow.

As summarized by (Best, 1992), ripple development in open channel flows is preceded by incipient features termed bed defects, although the mechanism governing their initiation remains a source of debate. Historically envisioned as a single mound formed by fluid turbulence (Williams & Kemp, 1971), defects cause spatial variations in local bed shear that eventually lead to the formation of ripples. However this model fails to explain the rapid development and spatially regularity of many defects, and especially their development in laminar flow (e.g. Coleman & Eling, 2000). Importantly, the work of Venditti et al. (2005) demonstrated that bed defects can develop spontaneously over the entire bed, rather than propagating downstream from a single node. Moreover, these same authors developed a mechanism for the initiation of bed defects (Venditti et al., 2006), and subsequently three-dimensional bedforms in open channel flows, which most probably can be effectively extended to laminar as well as highly concentrated flows that experience turbulence suppression. Specifically, (Venditti et al. (2006)) suggested that open channel flow can be regarded as a two-phase fluid flow consisting of a dense basal layer, which in their case coincided with the bedload layer, overlain by a low density upper layer. Under appropriate conditions, the interface separating the two fluids becomes hydrodynamically unstable, causing spatio-temporal variations in sediment transport and deposition, leading to bed defects. We believe that a similar mechanism explains our findings in the coarser grained flows. Here, the coarse, high concentration basal layer and faster, significantly more dilute overlying fluid are, respectively, analogous to the bedload layer and overlying clear water in open channel flows. Although the sampling rate of the CT scanner (2 Hz) and the flow speeds (~ 0.4 m/s) imposed a lower limit on a minimum resolvable hydrodynamic instability wavelength (0.2 m) that is approximately three times that of the bedforms, this mechanism of defect generation is supported by process of elimination. Consequently the hydrodynamic instability is sufficiently strong and close to the bed that it becomes imprinted, leading to the initiation of defects, and ultimately downstream migrating angular bedforms. Conversely, higher concentrations, or equivalently all finer grained flows, lack the requisite strong vertical density stratification in their near-bed region, and as a result the hydrodynamic instability is either too weak or too high above the bed to become imprinted, and accordingly a plane bed remains stable.

3.6. **Conclusions**

The present study investigates the density structure of sediment gravity currents using a range of well-sorted grain sizes and particle concentrations. Data show that the development of downstream migrating bedforms is controlled by both the concentration and density structure of the flow, the latter being governed by the interplay between hydraulic shear and particle settling velocity. Like ripples and dunes in open channel flows, we believe a steep near-bed density gradient is necessary to generate a hydrodynamic instability that imprints the bed and forms the incipient topographic defects that grow into downstream migrating bedforms. Note that although additional work is needed to identify thresholds on bedform development, this work shows that coarse-grained, dilute flows have a higher propensity to form such features. Since density structure depends on both grain size and concentration, future research should investigate polygrain flows to assess the effect of fine sediment, especially on the development of migrating bedforms, and hence cross-stratification in turbidities.

3.7. **References**

Allen, J. R. L., & Leeder, M. R. (1980). Criteria for the Instability of Upper-Stage Plane Beds. *Sedimentology, 27*(2), 209-217. doi: 10.1111/j.1365-3091.1980.tb01171.x

Arnott, R. W. C. (2012). Turbidites, and the Case of the Missing Dunes. *Journal of Sedimentary Research, 82*(5-6), 379-384. doi: 10.2110/Jsr.2012.29

Baas, J. H. (1994). A Flume Study on the Development and Equilibrium Morphology of Current Ripples in Very Fine Sand. *Sedimentology, 41*(2), 185-209. doi: 10.1111/j.1365-3091.1994.tb01400.x

Baas, J. H., & Best, J. L. (2002). Turbulence modulation in clay-rich sediment-laden flows and some implications for sediment deposition. *Journal of Sedimentary Research, 72*(3), 336-340. doi: 10.1306/120601720336

Bennett, S. J., Bridge, J. S., & Best, J. L. (1998). Fluid and sediment dynamics of upper stage plane beds. *Journal of Geophysical Research-Oceans, 103*(C1), 1239-1274. doi: 10.1029/97jc02764

Best, J. (1992). On the Entrainment of Sediment and Initiation of Bed Defects - Insights from Recent Developments within Turbulent Boundary-Layer Research. *Sedimentology, 39*(5), 797-811. doi: 10.1111/j.1365-3091.1992.tb02154.x

Best, J. L., Kostaschuk, R. A., Peakall, J., Villard, P. V., & Franklin, M. (2005). Whole flow field dynamics and velocity pulsing within natural sediment-laden underflows. *Geology, 33*(10), 765-768. doi: 10.1130/G21516.1

Bouma, A. H. (1962). *Sedimentology of some flysch deposits: a graphic approach to facies interpretation*. Amsterdam: Elsevier.

Cartigny, M. J. B., Eggenhuisen, J. T., Hansen, E. W. M., & Postma, G. (2013). Concentration-Dependent Flow Stratification in Experimental High-Density Turbidity Currents and Their Relevance to Turbidite Facies Models. *Journal of Sedimentary Research, 83*(11-12), 1047-1065. doi: 10.2110/Jsr.2013.71

Coleman, S. E., & Eling, B. (2000). Sand wavelets in laminar open-channel flows. *Journal of Hydraulic Research, 38*(5), 331-338. doi: 10.1080/00221680009498314

Ganti, V., Lamb, M. P., & McElroy, B. (2014). Quantitative bounds on morphodynamics and implications for reading the sedimentary record. *Nat Commun, 5*, 3298. doi: 10.1038/ncomms4298

Kneller, B., & Buckee, C. (2000). The structure and fluid mechanics of turbidity currents: a review of some recent studies and their geological implications. *Sedimentology, 47,* 62-94. doi: 10.1046/j.1365-3091.2000.047s1062.x

Lowe, D. R. (1988). Suspended-Load Fallout Rate as an Independent Variable in the Analysis of Current Structures. *Sedimentology, 35*(5), 765-776. doi: 10.1111/j.1365-3091.1988.tb01250.x

Parker, G., Fu, X., Zhang, Y., Zinger, J., & Konsoer, K. (2013). *Bedform Regime Diagram for Rivers and Turbidity Currents: Conditions for the Formation and Obliteration of Dunes.* Paper presented at the Proceedings of 2013 IAHR Congress.

Schindler, R. J., Parsons, D. R., Ye, L., Hope, J. A., Baas, J. H., Peakall, J., . . . Bass, S. J. (2015). Sticky stuff: Redefining bedform prediction in modern and ancient environments. *Geology, 43*(5), 399-402. doi: 10.1130/g36262.1

Sequeiros, O. E., Spinewine, B., Beaubouef, R. T., Sun, T., Garcia, M. H., & Parker, G. (2010a). Bedload transport and bed resistance associated with density and turbidity currents. *Sedimentology, 57*(6), 1463-1490. doi: 10.1111/j.1365-3091.2010.01152.x

Sequeiros, O. E., Spinewine, B., Beaubouef, R. T., Sun, T., Garcia, M. H., & Parker, G. (2010b). Characteristics of Velocity and Excess Density Profiles of Saline Underflows and Turbidity Currents Flowing over a Mobile Bed. *Journal of Hydraulic Engineering, 136*(7), 412-433. doi: 10.1061/(Asce)Hy.1943-7900.0000200

Southard, J. B. (1991). Experimental-Determination of Bed-Form Stability. *Annual Review of Earth and Planetary Sciences, 19*(1), 423-455. doi: 10.1146/annurev.earth.19.1.423

Southard, J. B., & Boguchwal, L. A. (1990). Bed configuration in steady unidirectional water flows; Part 2, Synthesis of flume data. *Journal of Sedimentary Research, 60*(5), 658-679. doi: 10.1306/212f9241-2b24-11d7-8648000102c1865d

Talling, P. J. (2013). Hybrid submarine flows comprising turbidity current and cohesive debris flow: Deposits, theoretical and experimental analyses, and generalized models. *Geosphere, 9*(3), 460-488. doi: 10.1130/Ges00793.1

Venditti, J. G., Church, M., & Bennett, S. J. (2006). On interfacial instability as a cause of transverse subcritical bed forms. *Water Resources Research*, *42*(7). doi:10.1029/2005wr004346

Venditti, J. G., Church, M. A., & Bennett, S. J. (2005). Bed form initiation from a flat sand bed. *Journal of Geophysical Research-Earth Surface*, *110*(F1). doi:10.1029/2004jf000149

Walker, R. G. (1965). The Origin and Significance of the Internal Sedimentary Structures of Turbidites. *Proceedings of the Yorkshire Geological Society*, *35*(1), 1-32. doi: 10.1144/pygs.35.1.1

Williams, P. B., & Kemp, P. H. (1971). Initiation of ripples on a flat sediment bed. *Journal of Hydraulic Engineering, 97*(4), 502-522.

Xu, J. P., Sequeiros, O. E., & Noble, M. A. (2014). Sediment concentrations, flow conditions, and downstream evolution of two turbidity currents, Monterey Canyon, USA. *Deep-Sea Research Part I-Oceanographic Research Papers, 89*, 11-34. doi: 10.1016/j.dsr.2014.04.001

3.8. **List of Figures**

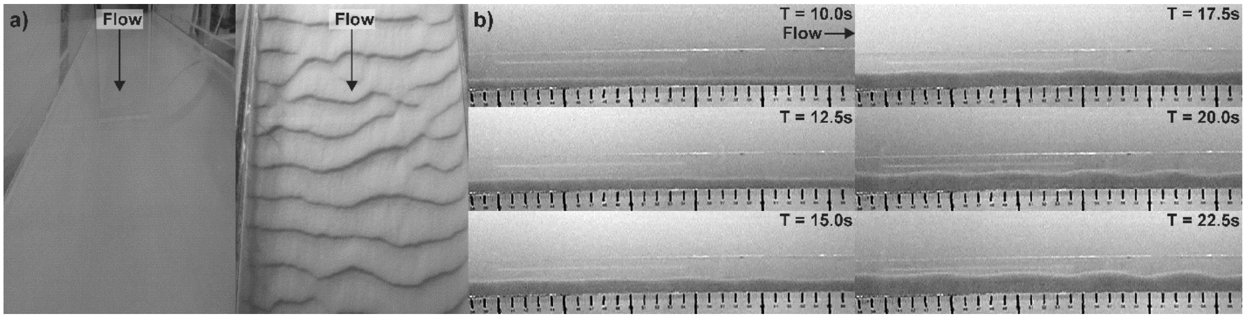

Figure 3-1: a) End member bed morphologies (indicated by the arrows): planar bed (left), and downstream migrating angular bedforms (right). b) Temporal development of angular bedforms.

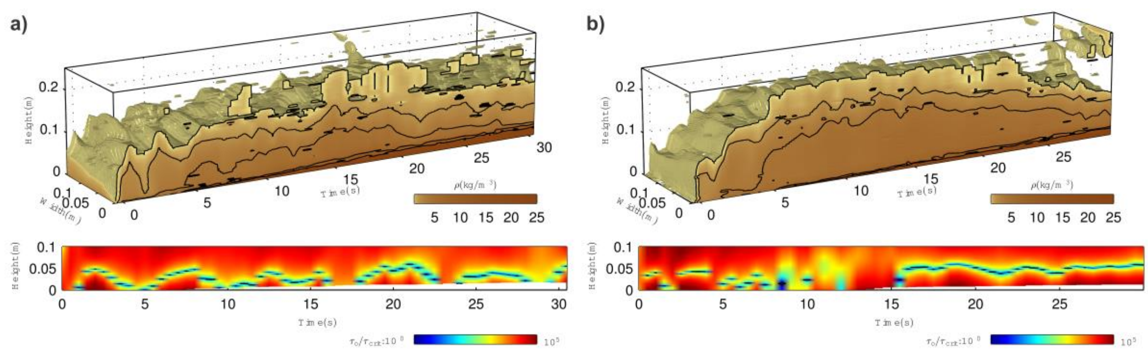

Figure 3-2: Temporal evolution of sediment and hydraulic properties in the 230 μm (a) and 150 μm (b) runs (9.5% by mass). The upper part of the figure shows the volumetric reconstructions from time-lapse CT images, with contour intervals at 1%, 2%, 4% and 8% by mass; lateral 0 m position corresponds with the centerline of the flume. The lower part of the figure shows time-space variations in $\tau_{\circ}/\tau_{crit}$, with contours for $\tau_{\circ}/\tau_{crit} \leq 1$.

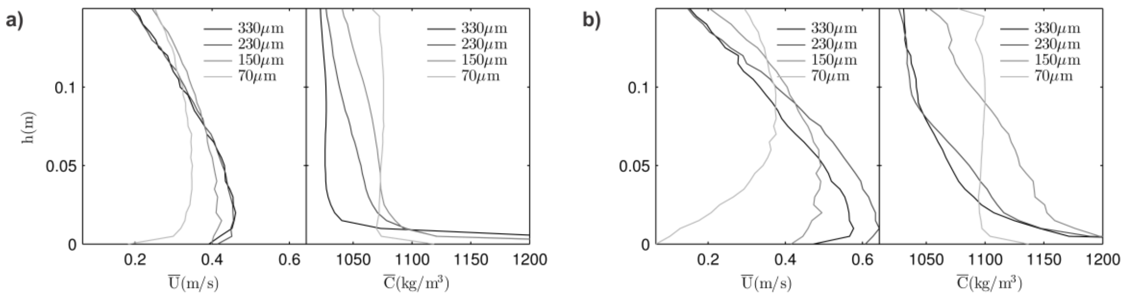

Figure 3-3: Time-averaged velocity and concentration profiles for the four grain sizes (330 µm, 230 µm, 150 µm, and 70 µm) at concentrations of a) 9.5% and b) 17.5% by mass. Only the basal portion of the flow is shown as it is here where bedforms develop.

Table 3-1: Summary of flow properties and depositional characteristics for all experimental flows. Note that these are time-averaged values of flow thickness (δ, position at $0.5u_{max}$), height of u_{max}, along with depth averaged and local values (at u_{max}) of u, ρ_{flow}, the Reynolds (Re_d)and densiometric Froude numbers (Fr_d). Standard deviation is included to reflect some of the current's temporal dynamics.

Slurry Conc.	d_{50}	Bed Morphology	δ (cm)		U (cm/s)		ρ_{flow} (kg/m³)		Re_d (×10⁴)	Fr_d
			Depth Avg.	at U_{max}	Depth Avg.	at U_{max}	Depth Avg.	at U_{max}	$(\rho_f \tilde{u} \delta/\mu)$	[illegible]
5% mass (2% vol.)	70 µm	Plane	16.3 ±1.9	3.8 ±1.3	19.8 ±2.3	31.0 ±4.4	1015 ±5	1020 ±6	2.16	1.63
	150 µm	Plane	14.8 ±1.8	3.6 ±1.6	22.7 ±4.8	35.6 ±6.0	1014 ±7	1020 ±7	2.27	1.95
	230 µm	3D Bedform	14.0 ±3.8	3.1 ±1.3	21.8 ±11.0	34.3 ±10.8	1012 ±7	1014 ±7	2.28	2.35
	330 µm	3D Bedform	- ± -	- ± -	- ± -	- ± -	- ± -	- ± -	-	-
9.5% mass (4% vol.)	70 µm	Plane	16.8 ±1.6	5.4 ±2.2	22.1 ±0.6	35.4 ±7.9	1040 ±9	1050 ±9	2.56	1.27
	150 µm	Plane	14.8 ±2.4	2.1 ±1.4	27.0 ±13.5	41.8 ±14.9	1040 ±13	1059 ±19	2.90	1.47
	230 µm	3D Bedform	12.5 ±2.7	2.1 ±1.4	27.0 ±11.9	45.3 ±13.5	1035 ±15	1053 ±28	2.45	1.64
	330 µm	3D Bedform	11.7 ±2.9	2.0 ±1.1	26.0 ±14.9	45.8 ±19.3	1009 ±6	1020 ±55	2.39	6.17
17.5% mass (8% vol.)	70 µm	Plane	17.1 ±2.2	7.6 ±3.2	20.1 ±3.3	40.3 ±6.5	1050 ±13	1076 ±12	2.35	0.82
	150 µm	Plane	10.9 ±2.4	4.6 ±1.6	28.9 ±17.7	46.3 ±16.3	1084 ±15	1137 ±29	2.42	1.21
	230 µm	Plane	9.8 ±1.6	1.3 ±0.5	33.3 ±10.5	63.6 ±12.2	1068 ±27	1116 ±31	2.36	1.56
	330 µm	Plane	8.9 ±2.8	5.7 ±2.4	30.7 ±20.3	57.2 ±24.3	1090 ±29	1098 ±36	2.29	1.33

CHAPTER 4: HOW DO FLUIDS REALLY BEHAVE? SCRUTINIZING THE BOUSSINESQ DENSITY APPROXIMATION IN PARTICLE GRAVITY (TURBIDITY) FLOWS USING CT IMAGERY

M. Tilston[1], R.W.C. Arnott[1], and C.D. Rennie[2]

[1]Department of Earth Sciences, University of Ottawa, Ottawa ON

[2]Department of Civil Engineering, University of Ottawa, Ottawa ON

4.1. **Abstract**

One of the most widely invoked assumptions when describing the properties of geophysical flows is the Boussinesq density approximation, which assumes that density stratification effects are negligible when describing the shearing behavior in fluids. While this generalization is suitable for most flows, it may be inappropriate for particle gravity flows where the neutrally buoyant fluid, which makes up the majority of the flow, is entrained by suspended particles kept aloft by shear forces related to a vertical momentum gradient. This distinction is especially important for understanding the flow dynamics of the largest sediment transporting events on Earth: turbidity currents. However, addressing this question has previously been impeded by the technical challenges of measuring fluid density and, consequently, flow behavior has typically been explained based solely on their velocity fields.

Here we report on a series of experiments that paired a three-dimensional ultrasonic Doppler velocity profiler (UDVP-3D) and a medical-grade computed tomography (CT) scanner to simultaneously examine the velocity and density structure of sediment gravity currents for two well sorted grain sizes (d_{50}: 150 and 330 µm) at an excess sediment concentration of ~18% by mass (8% by volume). Results show that the point of maximum density stratification shifts away from the bed with decreasing particle size, and the density stratification trends are tracked by the velocity structure. Density stratification, on the other hand, increases the divergence between the velocity and momentum fields, the latter being vertically constrained towards the basal region of the flow. Lastly, a momentum gradient analysis shows that the density and velocity gradient terms are the same order of magnitude, which invalidates the Boussinesq density approximation.

Accordingly, a density based framework is needed to more accurately describe the flow mechanics of density stratified flows like turbidity currents.

Keywords: Fluid mechanics, turbidity currents, density stratification, momentum structure, Boussinesq density approximation.

4.2. **Article**

From atmospheric circulation, to oceanic currents, to fluvial systems that serve as a major link between terrestrial and marine environments, the surface of the planet is principally molded by the action of moving fluids (Ganti et al., 2014), and therefore understanding the mechanics that govern them is essential for interpreting the past, present and future morphologies of the Earth's surface. In the vast majority of geophysical flows this can be reduced to a relatively simple conceptual model where the shearing that results from the interaction of a moving fluid and boundary resistance drives turbulence and sediment transport, as described by the Navier-Stokes equations. Yet these equations require a number of simplifying assumptions to reduce them into a solvable format, some of which may not be appropriate for all geophysical flows. One potentially erroneous assumption is the Boussinesq density approximation.

Central to the very existence of particle gravity currents is suspended sediment, which is controlled by the ratio of turbulent velocity fluctuations, which keep the particles aloft, to particle settling velocity (Rouse, 1937). Since the pioneering work of Osborne Reynolds on the mechanics of homogeneous, incompressible fluids (Reynolds, 1883, 1895), it's been widely accepted that the shear stresses responsible for generating these turbulent fluctuations can be described by local velocity gradients and bulk fluid density parameters. These conditions form the basis of the Boussinesq density approximation, where density gradient effects are assumed to be negligible owing to weak stratification. The impact of this assumption can be demonstrated by the vertical momentum gradient:

$$\frac{\partial p}{\partial z} = \frac{\partial(\rho u)}{\partial z} = \rho\frac{\partial u}{\partial z} + u\frac{\partial \rho}{\partial z} \qquad 4.1$$

where p, ρ and u are fluid momentum, density and velocity, respectively, and z is positive away from the bed. By adopting the Boussinesq density approximation the density gradient term ($u(\partial\rho/\partial z)$) reduces to zero, and changes the momentum gradient expression to its more conventional format ($\rho(\partial u/\partial z)$). In addition to simplifying the math, this assumption has significant practical advantages because it eliminates the need for an accurate estimate of particle concentration, which has been a longstanding problem. Indeed under low particle concentrations, one might argue that the total momentum carried by the particles is so small compared to the bulk current as to be ignored (Reynolds, 1987). However unlike most geophysical flows where gravity acts on the fluid, which then entrains sediment, gravity acts directly on suspended solids in turbidity currents, which then entrain the (neutrally-buoyant) ambient fluid (Middleton, 1966), indicating that particle momentum is responsible for generating the current and therefore cannot be neglected. This is an important question since particle gravity currents, which may only represent a small percentage of geophysical flows are disproportionately significant in terms of their geomorphic and economic impact.

Turbidity currents are turbulent particle suspensions that are not just the principal mechanism for conveying sediments down the continental slope and onto the deep ocean floor, but also the largest sediment transporting events on the planet. (Talling, Amy, et al., 2007). With individual flow events lasting just hours to days (Allen, 1991) they transport the equivalent of the annual sediment flux from all of the worlds fluvial systems combined (Talling, Wynn, et al., 2007), in addition to building up the largest and some of the most economically important sedimentary bodies on Earth (Saller et al., 2006). Yet for numerous reasons, the fluid-particle interactions that invariably control these flows remain poorly understood. First, natural continental margin turbidity currents form in deep water, and their highly episodic and notoriously destructive nature makes *in situ* measurements, especially near the bed, difficult (Khripounoff et al., 2003). Second, obtaining simultaneous velocity and density data from natural, but also experimental currents, poses many technical challenges, notably the density component. Most experimental flows are limited to very dilute particle suspensions (Hosseini et al., 2006), or even saline solutions to generate excess density that mimic turbidity currents, although the latter are unable to replicate the fluid-particle processes that might lead to density stratification characteristics in real sediment gravity flows. Accordingly, density stratification effects are generally neglected and momentum characteristics are equated to velocity structure, like in open channel flows.

Vertically, turbidity currents can be divided into two parts based on the principal source of flow resistance (Stacey & Bowen, 1988), which defines the sign of their velocity gradient and therefore the nature of fluid mixing in the absence of density effects. The lower region, or inner zone, is controlled by resistance with the bed and characterized by a positive velocity gradient up to the velocity maxima (u_{max}) and is thought to be broadly analogous to typical wall-bounded shear flows. As such, turbulent mixing and sediment suspension processes are similar to open channel flows, with vertical momentum exchange taking place by the movement of coherent fluid couplets known as bursts and sweeps that bring low speed fluid away and high speed fluid towards the bed, respectively (Robinson, 1991) – it is the anisotropy between the intensity and frequency of these motions that is responsible for particle suspension (Bagnold, 1966). Above u_{max} lies the outer region that is characterized by a negative velocity gradient where resistance is provided by the ambient fluid and enhanced mixing by Kelvin-Helmholtz instabilities that depresses u_{max} towards the base of the flow. As such, the flow mechanics in the outer region can be regarded as the mirror image of those acting in the inner region, but with a reversed Reynolds stress pattern (Gray et al., 2005). Separating these is a narrow region where the velocity gradient is zero (u_{max}), leading to the idea that this area represents a barrier to vertical momentum exchange between the inner and outer regions (Garcia & Parker, 1993). Yet if we accept that density stratification effects are important, then this model may be incomplete.

Generally, the vertical density structure of turbidity currents consists of two end-member configurations: 1) a plug-like structure where density is close to uniform in all but a thin region at the interface between the current and the ambient fluid, and 2) a highly dense basal layer that progressively weakens upward (Garcia, 1994; Sequeiros et al., 2009; Tilston et al., 2015). While there are two opposing hypothesizes to explain these endmember states, one based on flow criticality that controls the stratification stability of fluids (Sequeiros, 2012) and the other on the balance between turbulent velocity fluctuations (oriented perpendicular to the bed) that promote sediment suspension and particle settling velocities (Leeder et al., 2005), it is irrefutable that the stronger the density stratification, the greater the divergence between a current's momentum and velocity structures. Fundamentally, this refutes the Boussinesq density approximation. From an experimental perspective, modulating the stratification of experimental density currents is simple: changing either the slurry outflow rate or particle diameter will achieve this. However measuring the effects of that stratification are hampered by conventional instrumentation, and hence alternatives are needed. One candidate is computed tomography (CT), which allows non-intrusive detection of even minute density variations.

The experimental apparatus consists of a 7 m long horizontal, closed-top acrylic flume (inner dimension of 0.3 × 0.3 m) where the proximal end is connected to a 0.8 m^3 cylindrical mixing tank suspended 1.87 m and the distal end is attached to a partitioned reservoir tank that maintains ambient fluid levels and captures the experimental current (**Figure 4-1a**). Cross-sectional density data was measured using the CT scanner (2 Hz), situated 4 m from the proximal end of the flume, and was paired with a 2 MHz three-dimensional ultrasonic Doppler velocimeter (UDV-3D: ~23 Hz) to obtain high resolution, instantaneous full-depth profiles of the flow structure. Two slurries with sediment concentrations of 12% by volume (17.5% by mass) were created, one using well-sorted fine sand (d_{50}: 150 µm) and the other with well-sorted medium sand (d_{50}: 330 µm). The resulting currents were consistent with those in the summary of experimental work by Kneller and Buckee (2000); both currents were supercritical, fully turbulent and highly depositional throughout their anatomies, yet qualitatively they differed markedly in their vertical structure (**Figure 4-1b**). In the medium sand current, the high density portion of the flow is constrained to the near-bed region and overlain by a thick, dilute cloud of sediment (**Figure 4-1bi**). By comparison, the dense basal portion of the fine sand current is more vertically extensive and the overlying, dilute sediment cloud is vertically constrained (**Figure 4-1bii**). These observations are consistent with the size of the Kelvin-Helmholtz instabilities atop the currents, where their vertical extent appears constrained to zones with strong density gradients (**Figure 4-1b**). These density trends are confirmed by the volumetric reconstructions from the CT scanner.

Density volumes are created by cross-sectional time-lapse data slices from a fixed location, and therefore show flow evolution at that location with time. Cropping along the base of the volumes shows the height of the aggrading (static) bed. The top is an isosurface of 1% excess density by volume, which is the approximate density resolution limit given the CT scanner's sampling parameters for these experiments. The longitudinal slice corresponds with the centerline of the flume (and the position of the UDV-3D), thereby minimizing wall effects.

Temporally, the head-body and body-tail transitions in both experimental flows occur at ~2 s and ~20 s, respectively (**Figure 4-2a**). The heads are characterized by increasing sediment concentration and general flow acceleration due to reduced mixing and low flow resistance once the ambient fluid has been displaced by the current's nose, which is a well-documented phenomenon (Allen, 1971). Conversely, the body and the tail are both quasi-steady in terms of their velocity and density structures, with the transition marked by rapid flow deceleration and collapse. Remarkably, the density structure of the two currents is very different despite being formed under similar conditions. The fine sand flow displays a quasi-linear decrease in density away from the bed (maximum stratification at $h \sim 0.10\ m$) whereas the maximum density stratification of the medium sand current is found in the near bed region ($h \sim 0.01\ m$) and overlain by a thick dilute and poorly stratified zone (**Figure 4-2a**). Additionally, undulations in the 1% iso-surface are much more pronounced in the 330 µm current, in agreement with visual observations, and are attributed to Kelvin-Helmholtz like instabilities entraining the dense basal fluid vertically through the flow; similar but smaller features were observed in the 150 µm run, but are too small to be measured due to the CT's temporal averaging algorithm.

Recalling that these currents are driven by particle inertia, density structure must play at least some role in defining both their velocity and momentum flow fields. The 150 µm run has a thick, quasi-uniform high velocity core that becomes thinner and moves towards the bed in the 330 µm flow; presumably this trend is related to the latter's higher settling velocities and enhanced mixing with the ambient fluid (**Figure 4-2b**). This establishes a clear trend between particle size and vertical flow structure: the relative thinning of the inner region ($\partial u/\partial z > 0$) and thickening of the outer region ($\partial u/\partial z < 0$) is correlated with coarser particle suspensions. As we shall see, this trend is more pronounced if momentum characteristics are used to define the inner-outer region boundary. Crucially, if $\pm\ \partial p/\partial z$ is in fact the correct way to define the boundary, then p_{max} must coincide with $\partial p/\partial z = 0$ for the Boussinesq density approximation to be valid.

Vertically, the velocity and momentum structure of the 150 µm run are similar throughout the flow except for very near the bed, where the latter is more vertically uniform (**Figure 4-2c**). We attribute this to the general lowering and increased temporal variability in the position of p_{max} compared to u_{max}. Significantly this trend is more pronounced in the coarse grained run: here, p_{max} has been lowered to the point where it actually coincides with the bed, and the entire current becomes dominated by outer region flow behavior. Indeed, this finding is confirmed in the momentum gradient results obtained from **Equation 4-1**, which shows an upward switch from $\partial p/\partial z > 0$ to $\partial p/\partial z < 0$ in the lower portion of the fine grained run, whereas $\partial p/\partial z$ is always less than zero in the coarse grained run (**Figure 4-2d**). Importantly, the region where $\partial p/\partial z = 0$ is consistently situated above p_{max} in the 150 µm run, and despite the time-averaged values of $\partial p/\partial z < 0$ in the coarse grained run, here too we see distinct temporal pulses in the flow where $\partial p/\partial z > 0$. This is the first real hint that the Boussinesq density approximation may not be appropriate for particle gravity currents.

To test this intriguing result we plot the ratio (φ) of the density ($u(\partial\rho/\partial z)$) and velocity ($\rho(\partial u/\partial z)$) shear terms from **Equation 4-1** to determine their relative contribution to the net density gradient (**Figure 4-2e**). In both experimental currents, the upper portion of the flow is characterized by values of $\varphi \approx 0$, indicating that density stratification effects are negligible and the Boussinesq approximation is indeed valid. Yet this is not the case in the lower regions of flow. Here the absolute values of φ demonstrate that the $u(\partial\rho/\partial z)$ term makes a significant contribution towards defining the net momentum gradient structure, and is greatest in the coarse grained current due to its steep near-bed density gradient. Crucially, the data in **Figure 4-2e** has been normalized, and a value of $\varphi = 1$ is equivalent to $\varphi \approx 10^4$ in un-normalized data units; this clearly demonstrates the invalidity of the Boussinesq approximation. Of particular note is the upward shift from $\varphi < 0$ to $\varphi > 0$. Values of $\varphi > 0$ indicate the current's velocity and density characteristics are acting constructively, enhancing the local momentum gradient, while the opposite is true when $\varphi < 0$. This suggests that density stratification effects serve to dampen and enhance shear stress in the regions below and above u_{max}, respectively, compared to the values predicted using the Boussinesq density approximation.

Collectively these results can be synthesized into a conceptual model that describes the flow structure of turbidity currents based largely on their density stratification characteristics. Begin by considering their two end member states: 1) a non-stratified current where the Boussinesq density approximation can be applied, and 2) a highly stratified density flow that violates the Boussinesq approximation (**Figure 4-3a**). It is worth noting that while we have modulated stratification by altering particle size, the same effect can be achieved with the same particle diameter but different flow speed. In the case of the non-stratified current, gravity acts uniformly through the flow, producing a thick high velocity core that is lifted well above the bed. In stratified flows, on the other hand, gravity acts preferentially on the high-density basal part of the flow, resulting in a thin high velocity core that hugs the bed. Yet if we accept that it is momentum rather than velocity that controls flow processes, high density stratification causes the entire momentum structure to be condensed with respect to the velocity field. Conversely, the momentum and velocity structures of the non-stratified current remain similar (**Figure 4-3b**). Since the inner and outer flow regions of turbidity currents have historically been defined by $\partial u/\partial z > 0$ and $\partial u/\partial z < 0$, respectively, and while this is appropriate for non-stratified currents, there is a large deviation between $\partial u/\partial z$ and $\partial p/\partial z$ in stratified flows (**Figure 4-3c**). This has broad implications for how we interpret mixing characteristics and, as shown above, there is a tendency to overestimate the relative size of the inner region with respect to the outer region (**Figure 4-3d**). Indeed this may help explain why scaling flow characteristics of particle gravity currents has proven to be notoriously difficult.

Although this work has focused on turbidity currents, results from the testing of the applicability of the Boussinesq density approximation has broader implications for understanding stratified fluid flows. For example, we have shown that in regions where $\partial u/\partial z > 0$, velocity shear effects are muted by $\partial \rho/\partial z$, which is always negative, leading to a weaker momentum gradient than what would be predicted using the Boussinesq density approximation. Although these conditions are only met in the lower portion of turbidity currents, these condition are always satisfied in more common systems like open channel flows. Here the Boussinesq density approximation is always invoked, so it is interesting that suspended sediment transport is usually modelled by an extra viscosity term that reduces shear. Indeed, this may just be a convenient way of indirectly modelling density stratification effects. Similarly, little is known about the mechanisms responsible for capacity driven deposition, which might also be attributed to reduced shear due to strong density stratification. At a minimum, this concept certainly warrants further exploration.

4.3. **References**

Allen, J. R. L. (1971). Mixing at Turbidity Current Heads, and Its Geological Implications. *Journal of Sedimentary Petrology, 41*(1), 97-&. doi: 10.1306/74d721f8-2b21-11d7-8648000102c1865d

Allen, J. R. L. (1991). The Bouma Division-a and the Possible Duration of Turbidity Currents. *Journal of Sedimentary Petrology, 61*(2), 291-295. doi: 10.1306/d42676f4-2b26-11d7-8648000102c1865d

Bagnold, R. A. (1966). An approach to the sediment transport problem from general physics *Professional Paper* (- ed.).

Ganti, V., Lamb, M. P., & McElroy, B. (2014). Quantitative bounds on morphodynamics and implications for reading the sedimentary record. *Nat Commun, 5*, 3298. doi: 10.1038/ncomms4298

Garcia, M., & Parker, G. (1993). Experiments on the entrainment of sediment into suspension by a dense bottom current. *Journal of Geophysical Research, 98*(C3), 4793. doi: 10.1029/92jc02404

Garcia, M. H. (1994). Depositional Turbidity Currents Laden with Poorly Sorted Sediment. *Journal of Hydraulic Engineering-Asce, 120*(11), 1240-1263. doi: 10.1061/(Asce)0733-9429

Gray, T. E., Alexander, J., & Leeder, M. R. (2005). Quantifying velocity and turbulence structure in depositing sustained turbidity currents across breaks in slope. *Sedimentology, 52*(3), 467-488. doi: 10.1111/j.1365-3091.2005.00705.x

Hosseini, S. A., Shamsai, A., & Ataie-Ashtiani, B. (2006). Synchronous measurements of the velocity and concentration in low density turbidity currents using an Acoustic Doppler Velocimeter. *Flow Measurement and Instrumentation, 17*(1), 59-68. doi: 10.1016/j.flowmeasinst.2005.05.002

Khripounoff, A., Vangriesheim, A., Babonneau, N., Crassous, P., Dennielou, B., & Savoye, B. (2003). Direct observation of intense turbidity current activity in the Zaire submarine valley at 4000 m water depth. *Marine Geology, 194*(3-4), 151-158. doi: 10.1016/S0025-3227(02)00677-1

Kneller, B., & Buckee, C. (2000). The structure and fluid mechanics of turbidity currents: a review of some recent studies and their geological implications. *Sedimentology, 47*, 62-94. doi: 10.1046/j.1365-3091.2000.047s1062.x

Leeder, M. R., Gray, T. E., & Alexander, J. (2005). Sediment suspension dynamics and a new criterion for the maintenance of turbulent suspensions. *Sedimentology, 52*(4), 683-691. doi: 10.1111/j.1365-3091.2005.00720.x

Middleton, G. V. (1966). Experiments on Density and Turbidity currents *Canadian Journal of Earth Sciences., 3*, 523-546.

Reynolds, O. (1883). An Experimental Investigation of the Circumstances Which Determine Whether the Motion of Water Shall Be Direct or Sinuous, and of the Law of Resistance in Parallel Channels. *Philosophical Transactions of the Royal Society of London, 174*(0), 935-982. doi: 10.1098/rstl.1883.0029

Reynolds, O. (1895). On the Dynamical Theory of Incompressible Viscous Fluids and the Determination of the Criterion. *Philosophical Transactions of the Royal Society A: Mathematical, Physical and Engineering Sciences, 186,* 123-164. doi: 10.1098/rsta.1895.0004

Reynolds, S. (1987). A Recent Turbidity-Current Event, Hueneme-Fan, California - Reconstruction of Flow Properties. *Sedimentology, 34*(1), 129-137. doi: 10.1111/j.1365-3091.1987.tb00565.x

Robinson, S. K. (1991). Coherent Motions in the Turbulent Boundary-Layer. *Annual Review of Fluid Mechanics, 23*, 601-639. doi: 10.1146/annurev.fluid.23.1.601

Rouse, H. (1937). Modern Conceptions of the Mechanics or Fluid Turbulence. *Transactions of the American Society of Civil Engineers, 102*(1), 463-505.

Saller, A., Lin, R., & Dunham, J. (2006). Leaves in turbidite sands: The main source of oil and gas in the deep-water Kutei Basin, Indonesia. *Aapg Bulletin, 90*(10), 1585-1608. doi: 10.1306/04110605127

Sequeiros, O. E. (2012). Estimating turbidity current conditions from channel morphology: A Froude number approach. *Journal of Geophysical Research-Oceans, 117*(C4). doi: 10.1029/2011jc007201

Sequeiros, O. E., Naruse, H., Endo, N., Garcia, M. H., & Parker, G. (2009). Experimental study on self-accelerating turbidity currents. *Journal of Geophysical Research-Oceans, 114*(C5). doi: 10.1029/2008jc005149

Stacey, M. W., & Bowen, A. J. (1988). The Vertical Structure of Density and Turbidity Currents - Theory and Observations. *Journal of Geophysical Research-Oceans, 93*(C4), 3528-3542. doi: Doi 10.1029/Jc093ic04p03528

Talling, P. J., Amy, L. A., & Wynn, R. B. (2007). New insight into the evolution of large-volume turbidity currents: comparison of turbidite shape and previous modelling results. *Sedimentology, 54*(4), 737-769. doi: 10.1111/j.1365-3091.2007.00858.x

Talling, P. J., Wynn, R. B., Masson, D. G., Frenz, M., Cronin, B. T., Schiebel, R., . . . Amy, L. A. (2007). Onset of submarine debris flow deposition far from original giant landslide. *Nature, 450*(7169), 541-544. doi: 10.1038/nature06313

Tilston, M., Arnott, R. W. C., Rennie, C. D., & Long, B. (2015). The influence of grain size on the velocity and sediment concentration profiles and depositional record of turbidity currents. *Geology, 43*(9), 839-842. doi: 10.1130/g37069.1

4.4. **List of Figures**

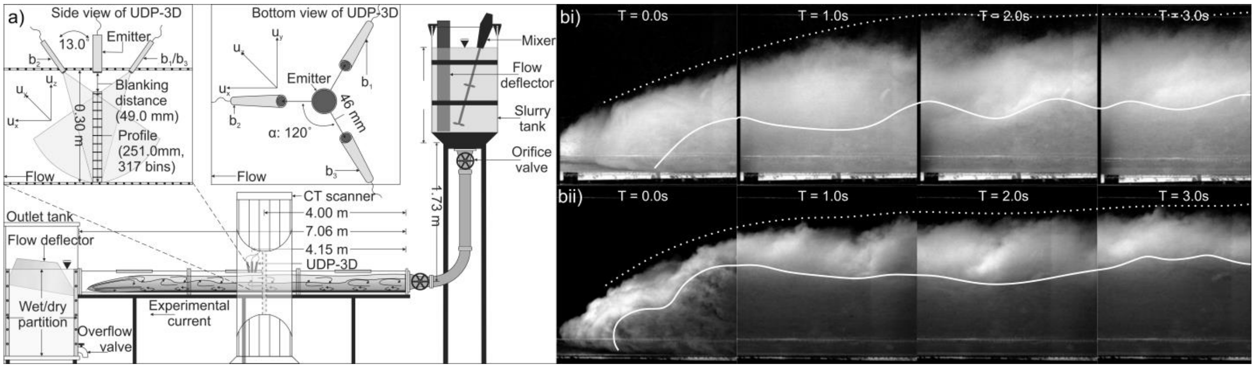

Figure 4-1: Schematic of the experimental apparatus (a) and qualitative comparison of the 330µm (bi) and 150µm (bii) experimental currents as revealed through high-speed, time-lapse photography. Traces delineating the approximate upper (dashed) and lower (solid) bounds of hydrodynamic instability driven mixing to highlight differences in vertical flow structure.

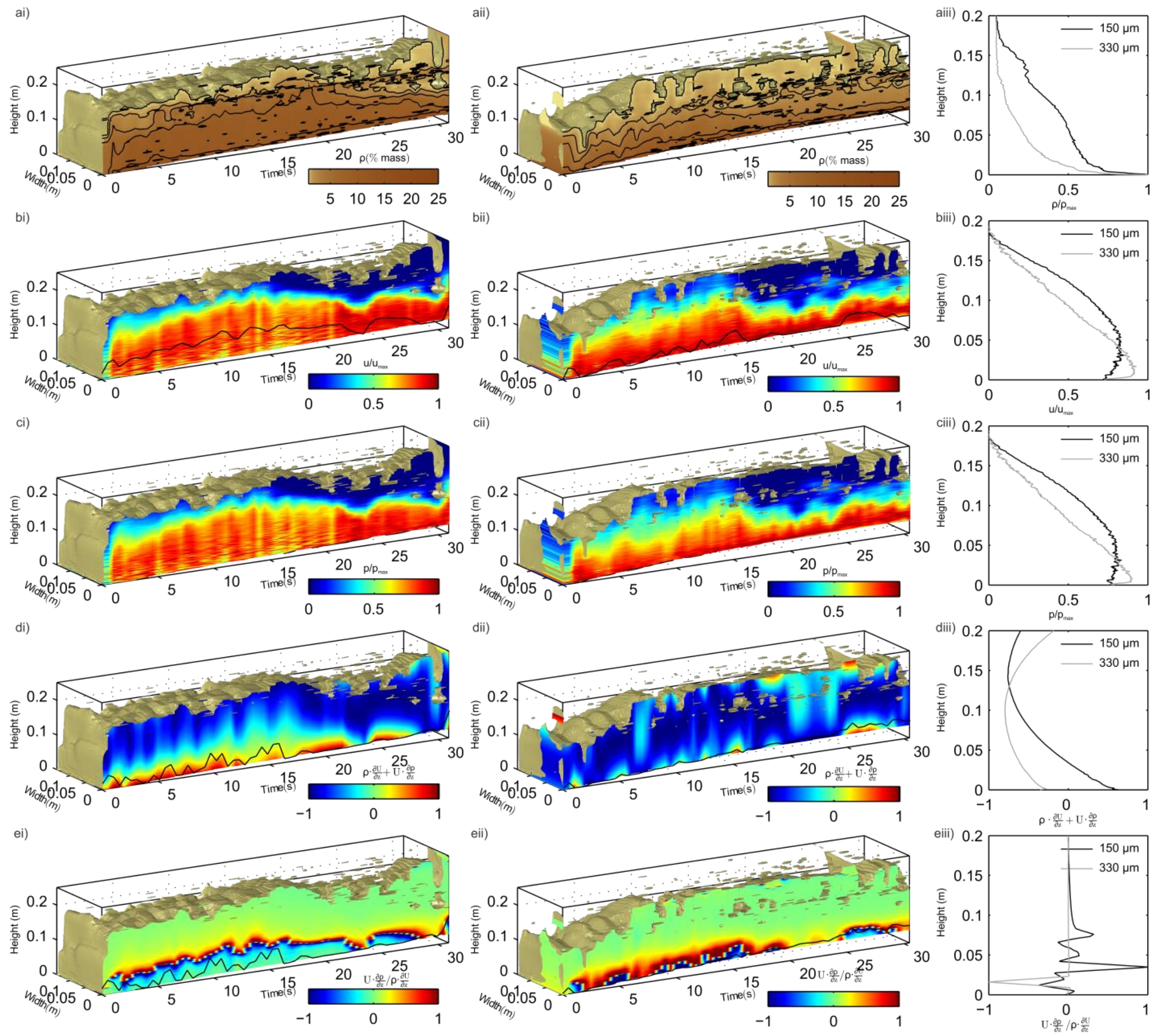

Figure 4-2: Volumetric reconstructions of the: (i) 150µm and (ii) 330µm experimental currents and their time-averaged characteristics (iii) for the following parameters: a) % excess by density (contours represent 1%, 2%, 4%, 8% and 12%); (b) velocity (u) -- position of u_{max} marked by the solid black line; (c) momentum (p) – positions of p_{max} and u_{max} marked in black and grey, respectively; (d) momentum gradient ($\partial p/\partial z = \rho\frac{\partial u}{\partial z} + u\frac{\partial \rho}{\partial z}$); (e) ratio of $u\frac{\partial \rho}{\partial z}$: $\rho\frac{\partial u}{\partial z}$ defining the net contribution of the two terms in forming $\partial p/\partial z$. Under the Boussinesq density approximation, $u\frac{\partial \rho}{\partial z}$: $\rho\frac{\partial u}{\partial z} = 0$.

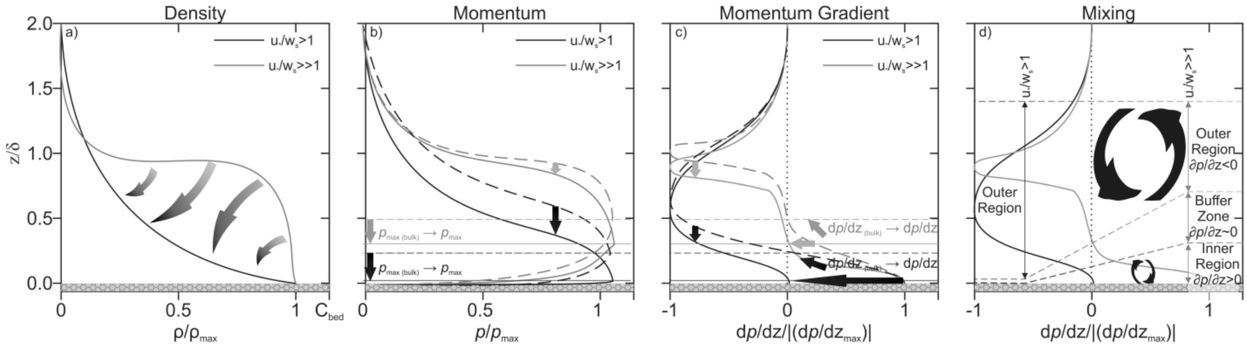

Figure 4-3: Momentum based conceptual model describing the vertical flow structure of turbidity currents: (a) variations in density stratification characteristics, determined by the ratio of shear (u_*) and particle settling (w_s), (b) comparative velocity (dashed) and momentum (solid) profiles (note the difference in the positions of u_{max} and p_{max}) (c) changes in momentum gradient by applying (dashed) or neglecting (solid) the Boussinesq density approximation, (d) implications for defining vertical flow structure of particle gravity currents on the basis of a velocity (grey) versus momentum (black) fields.

CHAPTER 5: CONCLUSIONS

5.1. **Summary**

Unlike most geophysical flows, turbidity currents owe their very existence to the presence of suspended particles, forming the active portion of the current, which then entrain the fluid, forming the passive component. As such, properly representing the mechanics responsible for particle suspension is crucial to better understanding the fluid-particle interactions that control these flows. Results of the work described here advances this issue on three crucial levels.

The first is the problematic issue of isolating turbulence, the fluid process responsible for maintaining sediment suspension, in highly unsteady flows. I begin with the generally held assumption that the maximum scales of turbulent motions are proportional to boundary layer thickness, and that the duration of these motions can be converted to physical sizes using a convection velocity as per Taylor's frozen turbulence hypothesis. In contrast to Taylor, who assumed that turbulent structures are convected at a rate proportional to the mean velocity, I develop a novel technique using the continuous wavelet transform, which provides an energy spectra for all frequencies and at all points of time to derive their equivalent convection velocities. This appears to be a highly robust methodology since it captures all the time and frequency variations in convection velocity, and the time-averaged values of the convection velocity are identical to those reported in Taylor's original hypothesis. This methodology may be superior to standard Reynolds decomposition for analyzing turbulence in any geophysical flows as it might help to better unravel the role of turbulence and the ubiquitous larger coherent fluid structures that are present in all flows, and how they relate to the geomorphic response of a deformable sediment substrate.

The second aspect is related to flow resistance and the unequal presence of angular bedforms in the deposits of turbidity currents (i.e. turbidites) and rivers. As outlined in the article, there are two competing models to explain the development of bed defects, which then lead to ripple formation. The first is related to incipient transport conditions, where turbulent motions lead to the development of localized defects, which then alter local flow structure in a way that allows the defects to propagate downstream and the bed to become progressively populated with angular bedforms. The second mode occurs under higher transport conditions when the entire bed is mobilized; this mobilized layer acts as a denser, slower moving basal fluid that allows for the development of hydrodynamic instabilities that instantly populate the entire bed with angular bedforms. In the experiments the bed shear stresses are well above the thresholds for motion, which is consistent with the waning flow conditions of turbidity currents entering their depositional stage. However angular bedforms only in those flows in which density decreased rapidly upward – plane bed remained stable in flows with a plug-like density profile. This suggests that the lack of angular bedform development is tied with current density structure and the absence of a well-defined bedload layer, and therefore the requisite conditions for the development of near-bed hydrodynamic instabilities needed for bed defect generation.

The final aspect is related to improving our understanding of the internal structure of turbidity currents and how flow structure is controlled by density stratification characteristics. Here it is demonstrated that the density structure of turbidity currents plays the primary role in defining their velocity fields, and also the divergence between their velocity and momentum characteristics. In most flow dynamics studies it is the velocity component that is used to describe and explain flow behavior, but here it is shown that with increasing density stratification, the density component eventually comes to control flow behavior. It is then shown that the widely applied Boussinesq density approximation, which assumes that density gradients are negligible in describing fluid processes, is not appropriate for highly stratified turbidity currents. Finally, a novel conceptual model is proposed to describe vertical momentum exchange, and therefore mixing and particle suspension dynamics in turbidity currents, and unifies their density and velocity fields. This model indicates that the traditional, velocity-based framework for defining their vertical structure could lead to substantial misinterpretations about their flow processes, notably the common perception that the velocity maxima represents a barrier to vertical momentum exchange.

5.2. **Next steps**

In this work the focus was on the effects of particle size and concentration in defining the flow structure of turbidity currents and their influence on bedform development, or small-scale depositional features. The next logical step is to expand this work to macro-scale morphologic features like submarine lobe deposits, whose outboard and vertical dimensions are linked with run-out distance. Ultimately, this is controlled by three key aspects that merit future work: 1) sediment suspension potential; 2) flow resistance; 3) the availability of marine mud.

As described in **Section 1.4**, sediment suspension is based on the ratio of buoyancy forces that can be described by either the flow's shear characteristics or the vertical component of turbulence in comparison to particle settling velocity. However there is still a great deal of uncertainty about how to best identify shear stress in turbidity currents. Indeed there is no well accepted method for isolating turbulence in unsteady flows, and the effects of suspended sediments on muting turbulence are poorly understood. These are basic questions that must be addressed before investigating the mechanics of sediment suspension in particle propelled density currents.

Next is the question of flow resistance, which in the case of turbidity current, is derived from two sources: 1) the bed and 2) the ambient fluid. In the case of the bed, there is still the ongoing debate of how supercritical flows can produce what appear to be subcritical bedforms. This is an exceptionally pressing question for sedimentary geologists as it directly impacts the ability to interpret flow properties at the time of deposition. Of equal interest is the extent of flow resistance (energy loss) that occurs between turbidity currents and the ambient fluid. It is easy to envision how larger Kelvin-Helmholtz instabilities would entrain more ambient fluid and slow the current, but has received little attention in the literature.

Finally there's the question on the availability of mud. An event as violent as a turbidity travelling downslope should easily erode pre-existing marine mud from the seafloor, thereby gaining mass and energy, promoting further gravitational acceleration and, ultimately, longer run-out distances. However, little is known about the factors affecting mud availability. Is it a result of flow frequency? Cementation?

APPENDIX A: ARTICLE 1

This is the published content from **Chapter 3**. Although this is a repeat of what is presented in **Chapter 3**, I felt this was an appropriate inclusion to demonstrate the scientific merits of this research project. I hope this appendix demonstrates that the scientific community is highly receptive to this research.

A.1: Tilston, M., Arnott, R.W.C., Rennie, C. and Long, B. (2015). The influence of grain size on the velocity and sediment concentration profiles and depositional record of turbidity currents. *Geology* 43, 839-842.

The influence of grain size on the velocity and sediment concentration profiles and depositional record of turbidity currents

M. Tilston[1], R.W.C. Arnott[1], C.D. Rennie[2], and B. Long[3]
[1]Department of Earth Sciences, University of Ottawa, Ottawa, K1N-6N5 Ontario, Canada
[2]Department of Civil Engineering, University of Ottawa, Ottawa, K1N-6N5 Ontario, Canada
[3]Centre Eau Terre Environnement, INRS, Québec City, G1P-4S5 Québec, Canada

ABSTRACT

Cross-stratification formed by migrating dunes is ubiquitous in fluvial channel deposits, yet cross-stratification, specifically formed by dunes, is comparatively uncommon in deep-marine channel deposits subjected to similarly unidirectional flows, the reasons for which is the subject of much debate. In part, this is related to the difficulty associated with acquiring high-resolution data sets; natural turbidity currents are highly destructive, whereas physical models are hampered by the shortcomings of conventional laboratory instrumentation. Consequently the internal structure of turbidity currents is poorly understood, thus hindering the ability to identify the linkages between flow properties and depositional characteristics. In this study we use a medical-grade computed tomography scanner coupled with a three-dimensional ultrasonic Doppler velocity profiler to characterize the flow field and depositional morphology across a range of grain sizes (d_{50}: 70–330 µm) and sediment concentrations (5%–17.5% by mass). Results show that the development of angular bedforms is suppressed in all flows with particle concentrations greater than 9.5% by mass, but notably also in all flows with particles <230 µm and sediment concentrations down to 5%, the lowest slurry densities used in these experiments, by mass. This suggests a first-order control on the response of the bed by the makeup of the overriding current. More fundamentally, we propose that grain size controls the character of near-bed density stratification, which is a requisite condition to generate the hydrodynamic instabilities that create the initial bed defects, which then lead to the development of angular bedforms like ripples and dunes.

INTRODUCTION

Turbidity currents, like open-channel flows, are unidirectional. But unlike open-channel flows, turbidity currents are propelled by gravity acting directly on the suspended sediment, and the interstitial fluid is entrained by the particles to form the current. Yet under low- to no-grade conditions such as on the basin floor, turbidity currents decelerate and eventually come to rest. Because net deposition occurs during the waning phase of these currents, their deposits (turbidites) exhibit a suite of sedimentological features that, stratigraphically upward, suggest progressively lower-energy conditions. This depositional model was popularized by Bouma (1962) who described distinctively upward-fining beds with a consistent vertical assemblage of depositional characteristics. Notably absent in this idealized succession, however, is dune cross-stratification, which, based on the open-channel flow literature, should occur above upper plane bed and below ripples in bed sediment calibre (d_{50}) between ~0.2 mm and 0.7 mm (cf. Southard and Boguchwal, 1990). The absence of dune cross-stratification in the Bouma model, and its paucity in ancient or modern deep-marine sedimentary records as a whole, has been noted by numerous authors and remains the subject of a long-standing debate.

Previous explanations focused on the requisite bed configuration and hydraulic conditions needed for angular bedform development, including insufficient growth time (Walker, 1965), the (negative) influence of suspended-sediment fallout on incipient bedform development (Lowe, 1988), the (negative) impact of turbulence suppression associated with higher suspended-sediment concentrations (Allen and Leeder, 1980; Lowe, 1988), and the (negative) effect of clay content on flow structure and/or bed rheology (Baas and Best, 2002; Schindler et al., 2015). However Arnott (2012) argued that based on the typical textural and geometric attributes of cross-stratification in most turbidites, and the duration of natural turbidity currents versus the time needed to create angular bedforms like ripples and dunes, these earlier explanations are questionable.

Recently, both laboratory experiments (Baas, 1994; Cartigny et al., 2013) and direct observations in submarine canyons (Talling, 2013; Xu et al., 2014) have shown that turbidity currents are commonly supercritical, whereas in open-channel flows, ripples and dunes form under subcritical conditions; thus the absence of angular bedforms results from the unique velocity and concentration profiles of density currents (Parker et al., 2013). However, experimental work has also confirmed the presence of downstream-migrating angular bedforms that are dimensionally similar to dunes in supercritical flow (Sequeiros et al., 2010); thus the Froude number may not be a good predictor of bed morphology in turbidity currents.

Another possible explanation for the lack of angular bedforms relates to the advection length of settling particles (Ganti et al., 2014). Here, the particle's advection length sets the size of the smallest morphologic features that can form, suggesting that coarser sediments are more likely to create smaller features, hence there is a distinct grain-size control in turbidite morphology.

Finally, Arnott (2012) suggested that the lack of dunes in turbidites might be related to the flow lacking a sufficiently well-developed near-bed hydrodynamic instability needed for (angular) bedform initiation and subsequent growth, however this explanation lacked experimental verification. The objective here, then, is to report on a set of novel experiments that continuously measured the velocity and, more importantly, density within depositional sediment-driven turbidity currents, and to link those characteristics to the ensuing bed morphology. In doing so, these data test the relationship between bedform development and the hydraulic state of the flow, as well as elucidate sediment concentration profiles near the bottom of suspended sediment–driven turbidity currents.

EXPERIMENTAL METHODS

Experimental currents were created in a horizontal, 7-m-long, acrylic closed-topped flume with inner cross-sectional dimensions of 0.3 × 0.3 m. Initial sediment slurries were homogenized in a 0.8 m^3 cylindrical mixing tank suspended 1.87 m above the flume with an orifice valve at the base of the mixing tank to control outflow rates. During each run, velocity and sediment-concentration data were collected continuously 4 m downstream of the flume inlet in order to permit full flow development and maximize measurement duration. Profiles of velocity were recorded with ~1.5 mm vertical resolution at 22 Hz using a three-dimensional ultrasonic Doppler velocity profiler. Direct density measurements were collected using a medical-grade computed tomography scanner as 360° cross-sectional, 512 × 512 pixel images of the flow. Image reconstruction was constrained to the cross-sectional area of the flume, making each pixel ~0.6 × 0.6 mm. This combination of equipment offers the advantages of being non-obtrusive, having minimal offset in sampling position of the two flow properties, and yielding data sets with very high spatial and temporal resolution.

A total of 12 experimental currents were run using four different well-sorted grain-size distributions of Ottawa sand and three concentrations.

GEOLOGY, September 2015; v. 43; no. 9; p. 839–842 | Data Repository item 2015285 | doi:10.1130/G37069.1

A summary of the experimental current properties and their resulting bed morphologies is provided in the GSA Data Repository[1]. For brevity, detailed analysis is limited to the 150 µm and 230 µm runs with a concentration of 9.5% by mass.

RESULTS

In general, all runs were fully turbulent, supercritical, and consistent in character with those reported in previous studies (e.g., Kneller and Buckee, 2000); namely, the arrival of the current head was marked by an abrupt increase in flow speed, followed by a slightly faster, quasi-steady body with an abrupt decrease in velocity in the current tail, and well-developed Kelvin-Helmholtz instabilities along the top of the currents. Depth- and time-averaged flow properties are controlled by initial slurry mass, whereas depositional morphology is controlled by both concentration and grain size.

Attendant also with the influence of grain size on flow structure are differences in the character of the aggraded bed, being either planar or covered entirely with small-scale, downstream-migrating bedforms (Fig. 1A). In the case of the former, video analysis showed a slight lag between the arrival of the current head and the onset of deposition, after which deposition was constant throughout the body. Millimeter-high, ephemeral sand mounds formed that lacked a consistent downstream-migration pattern, suggesting they result from non-uniform transport and deposition associated with flow pulsing (Best et al., 2005) rather than sand waves linked with the formation of upper-stage plane bed in rivers (Bennett et al., 1998). No evidence of these sand mounds was visible on the surface of the final bed deposit. In the case of the downstream-migrating bedforms, deposition was similar to that of the plane-bed runs for the first 8 s, after which short, equally spaced bed defects spontaneously appeared everywhere along the bed that then migrated downstream and grew to a height of several millimeters in only a few seconds (Fig. 1B). Presumably, the lag between the arrival of the head and bedform development is attributed to the lack of a preexisting deformable bed in our experiments (i.e., a Plexiglas surface) rather than a real change in current properties over this period. Notably, these bed features have spacing and heights of 70 mm and 5 mm, respectively, and thus are dimensionally similar to two-dimensional current ripples (Baas, 1994). Intriguingly, there is a clear control of grain size on the resulting bed morphology.

Irrespective of grain size, all runs with initial slurry concentrations of 17.5% by mass resulted in a planar deposit; significantly, ripples or dunes would dominate the bed morphology at these flow speeds, depths, and grain sizes (e.g., Southard, 1991) and particle advection length scales (Ganti et al., 2014) in open-channel flows.. As such, planar bedding is the byproduct of excessive suspended-particle concentrations. With decreasing sediment concentration, here the 9.5% and 5% currents, grain size begins to exert a profound effect on bed morphology. Again, based on flow speed and advection length, ripples would dominate in open-channel flows, yet despite having almost identical depth- and time-averaged hydraulic characteristics, the coarser-grained runs consistently produced downstream-migrating bedforms, whereas a plane bed formed in the finer-grained flows. Accordingly, the disparity in bed response may be related to how sediment is distributed within the flow.

Figure 2 presents a temporal volumetric reconstruction of current density, cut longitudinally through the center of the flume. Also included is the ratio between boundary shear stress $\left(\tau_0 = \rho\left(\kappa z \frac{du}{dz}\right)^2\right)$ and critical shear stress $[\tau_c = \theta_c(\rho_s - \rho)gd_{50}]$, where ρ is current density, κ is the von Kármán constant, du/dz is the vertical velocity gradient of streamwise velocity (u), z is flow thickness $[u(z) = u_{max}/2]$, , θ_c is the Shields parameter, ρ_s is sediment density, g is gravitational acceleration, and d_{50} is mean particle diameter. In both cases, τ_0/τ_c values are generally orders of magnitude greater than unity, suggesting general bedload transport rather than incipient-motion conditions. However, the way sediment is distributed through the water column differs significantly between the two runs. Whereas the 230 µm run is characterized by a highly concentrated basal layer above which is a dramatic decrease in suspended-sediment concentration, the 150 µm run shows a more gradual upward decrease in suspended-sediment concentration. Note that the region of low shear coincides with the position of the high-velocity core.

DISCUSSION

Although pervasive in fluvial deposits, cross-stratification formed by dunes is comparatively rare in the deep-marine sedimentary record, the reasons for which are unclear. Six hypotheses have been proposed to explain this disparity: (1) turbulence suppression, (2) insufficient development time, (3) excessive sedimentation rates, (4) hydraulic state of the flow, (5) particle advection length scales, and (6) bed rheology. However, these hypotheses are inconsistent with observations presented here because: (1) all flows were fully turbulent, (2) downstream-migrating bedforms developed in a matter of seconds, (3) sedimentation rates were higher in the coarser-grained currents that did form bedforms, (4) all flows were supercritical through the current body, but produced two distinct bed states, (5) advection length scales fell within the regime for angular bedforms, and (6) the bed is cohesionless. What is apparent is that grain size has a profound effect on the density structure of the currents, which in turn controls the final bed configuration.

Figure 3 presents the time-averaged velocity and concentration profiles for the 9.5% and 17.5% runs. Here, three important trends are associated with decreasing grain size. First, compared to coarse-grained flows (d_{50} ≥

[1]GSA Data Repository item 2015285, summary of flow properties and depositional characteristics for all experimental flows, is available online at www.geosociety.org/pubs/ft2015.htm, or on request from editing@geosociety.org or Documents Secretary, GSA, P.O. Box 9140, Boulder, CO 80301, USA.

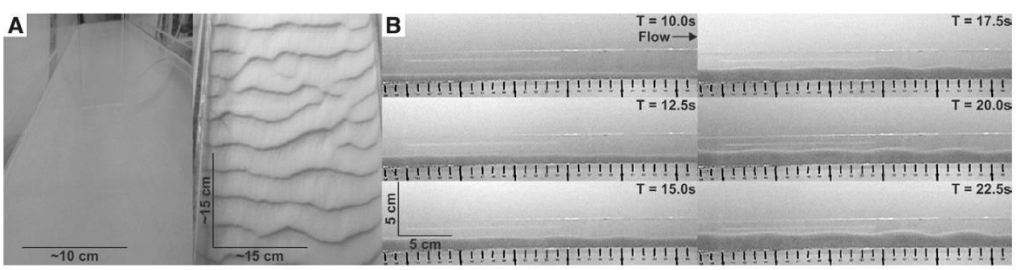

Figure 1. A: End-member bed morphologies: planar bed (left) and downstream-migrating angular bedforms (right). B: Temporal development of angular bedforms.

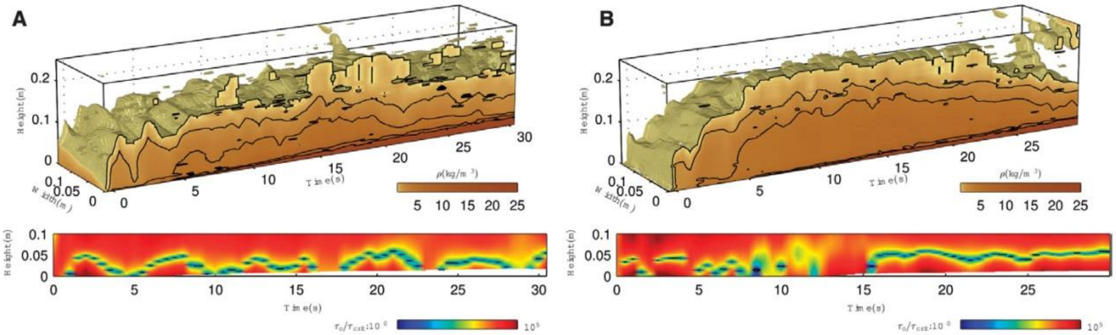

Figure 2. Temporal evolution of sediment and hydraulic properties in runs with particles of size 230 µm (A) and 150 µm (B) (9.5% by mass). Upper part of figure shows volumetric reconstructions from time-lapse computed tomography images, with contours at sediment concentrations of 1%, 2%, 4%, and 8% by mass (ρ is current density); lateral 0 m position corresponds with centerline of flume. Lower part of figure shows time-space variations in ratio between boundary shear stress and critical shear stress (τ_0/τ_{crit}); all values of $\tau_0/\tau_{crit} \geq 1$ where $du/dz \approx 0$.

230 µm), u_{max} in the fine-grained flows ($d_{50} \leq 150$ µm) is positioned higher above the static bed, which results in a lower vertical velocity gradient, and accordingly, reduced internal shear and related mixing. Second, the fine-grained flows are significantly less stratified; presumably, lower shear in the fine-grained flow is offset by reduced particle settling and increased particle interactions associated with the higher number of particles and surface area–to–volume ratios. Thirdly, angular bedforms only developed in the coarser-grained flows at concentrations up to 9.5% by mass, whereas at higher concentration, and more importantly in all of the fine-grained runs down to the lowest concentrations used in these experiments (5% by mass), a plane bed formed. These differences indicate that angular bedform development is controlled by both sediment concentration and grain size, as both of these parameters alter the vertical density structure of the flow; whereas fine-grained flows show a quasi-linear decrease in sediment concentration away from the bed, coarse-grained flows display a dense basal layer which thickens with concentration and is overlain by a much more dilute region of flow.

As summarized by Best (1992), ripple development in open-channel flows is preceded by incipient features termed bed defects, although the mechanism governing their initiation remains a source of debate. Historically envisioned as single mounds formed by fluid turbulence (Williams and Kemp, 1971), defects cause spatial variations in local bed shear that eventually lead to the formation of ripples. However this model fails to explain the rapid development and spatially regularity of many defects, and especially their development in laminar flow (e.g., Coleman and Eling, 2000). Importantly, the work of Venditti et al. (2005) demonstrated that bed defects can develop spontaneously over the entire bed rather than propagating downstream from a single node. Moreover, these same authors developed a mechanism for the initiation of bed defects (Venditti et al., 2006) and subsequently three-dimensional bedforms in open-channel flows, which most probably can be effectively extended to laminar as well as highly concentrated flows that experience turbulence suppression. Specifically, Venditti et al. (2006) suggested that open-channel flow can be regarded as a two-phase fluid flow consisting of a dense basal layer, which in their case coincided with the bedload layer, overlain by a low-density upper layer. Under appropriate conditions, the interface separating the two fluids becomes hydrodynamically unstable, causing spatio-temporal variations in sediment transport and deposition, leading to bed defects. We believe that a similar mechanism explains our findings in the coarser-grained flows. Here, the coarse, high-concentration basal layer and faster, significantly more dilute overlying fluid are, respectively, analogous to the bedload layer and overlying clear water in open-channel flows. Consequently the hydrodynamic instability is sufficiently strong and close to the bed that it becomes imprinted, leading to the initiation of defects and ultimately downstream-migrating angular bedforms. Conversely, higher-concentration flows, or equivalently all finer-grained flows, lack the requisite strong vertical density stratification in their near-bed region, and as a result, the hydrodynamic instability is either too weak or too high above the bed to become imprinted, and accordingly a plane bed remains stable.

CONCLUSIONS

The present study investigates the density structure of sediment gravity currents using a range of well-sorted grain sizes and particle concentrations. Data show that the development of downstream-migrating bed-

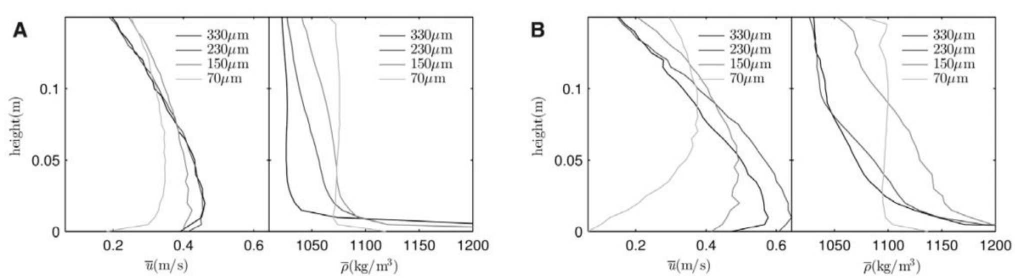

Figure 3. Time-averaged velocity (*u*) and concentration (ρ) profiles for four grain sizes (330 µm, 230 µm, 150 µm, and 70 µm) at sediment concentrations of 9.5% (A) and 17.5% (B) by mass. Only basal portion of flow is shown, as it is here that bedforms develop.

forms is controlled by both the concentration and density structure of the flow, the latter being governed by the interplay between hydraulic shear and particle settling velocity. Like for ripples and dunes in open-channel flows, we believe a steep near-bed density gradient is necessary to generate a hydrodynamic instability that imprints the bed and forms the incipient topographic defects that grow into downstream-migrating bedforms. Note that although additional work is needed to identify thresholds on bedform development, this work shows that coarse-grained, dilute flows have a higher propensity to form such features. Because density structure depends on both grain size and concentration, future research should investigate polygrain flows to assess the effect of fine sediment, especially on the development of migrating bedforms and hence cross-stratification in turbidites.

ACKNOWLEDGMENTS

We thank Mathieu Cartigny, Joris Eggenhuisen, and two anonymous reviewers for their helpful suggestions, and also corporate members of the Windermere Consortium.

REFERENCES CITED

Allen, J.R.L., and Leeder, M.R., 1980, Criteria for the instability of upper-stage plane beds: Sedimentology, v. 27, p. 209–217, doi:10.1111/j.1365-3091.1980.tb01171.x.

Arnott, R.W.C., 2012, Turbidites, and the case of the missing dunes: Journal of Sedimentary Research, v. 82, p. 379–384, doi:10.2110/jsr.2012.29.

Baas, J.H., 1994, A flume study on the development and equilibrium morphology of current ripples in very fine sand: Sedimentology, v. 41, p. 185–209, doi:10.1111/j.1365-3091.1994.tb01400.x.

Baas, J.H., and Best, J.L., 2002, Turbulence modulation in clay-rich sediment-laden flows and some implications for sediment deposition: Journal of Sedimentary Research, v. 72, p. 336–340, doi:10.1306/120601720336.

Bennett, S.J., Bridge, J.S., and Best, J.L., 1998, Fluid and sediment dynamics of upper stage plane beds: Journal of Geophysical Research, v. 103, p. 1239–1274, doi:10.1029/97JC02764.

Best, J., 1992, On the entrainment of sediment and initiation of bed defects—Insights from recent developments within turbulent boundary-layer research: Sedimentology, v. 39, p. 797–811, doi:10.1111/j.1365-3091.1992.tb02154.x.

Best, J.L., Kostaschuk, R.A., Peakall, J., Villard, P.V., and Franklin, M., 2005, Whole flow field dynamics and velocity pulsing within natural sediment-laden underflows: Geology, v. 33, p. 765–768, doi:10.1130/G21516.1.

Bouma, A.H., 1962, Sedimentology of Some Flysch Deposits: A Graphic Approach to Facies Interpretation: Amsterdam, Elsevier, 168 p.

Cartigny, M.J.B., Eggenhuisen, J.T., Hansen, E.W.M., and Postma, G., 2013, Concentration-dependent flow stratification in experimental high-density turbidity currents and their relevance to turbidite facies models: Journal of Sedimentary Research, v. 83, p. 1047–1065, doi:10.2110/jsr.2013.71.

Coleman, S.E., and Eling, B., 2000, Sand wavelets in laminar open-channel flows: Journal of Hydraulic Research, v. 38, p. 331–338, doi:10.1080/00221680009498314.

Ganti, V., Lamb, M.P., and McElroy, B., 2014, Quantitative bounds on morphodynamics and implications for reading the sedimentary record: Nature Communications, v. 5, 3298, doi:10.1038/ncomms4298.

Kneller, B., and Buckee, C., 2000, The structure and fluid mechanics of turbidity currents: A review of some recent studies and their geological implications: Sedimentology, v. 47, p. 62–94, doi:10.1046/j.1365-3091.2000.047s1062.x.

Lowe, D.R., 1988, Suspended-load fallout rate as an independent variable in the analysis of current structures: Sedimentology, v. 35, p. 765–776, doi:10.1111/j.1365-3091.1988.tb01250.x.

Parker, G., Fu, X., Zhang, Y., Zinger, J., and Konsoer, K., 2013, Bedform regime diagram for rivers and turbidity currents: Conditions for the formation and obliteration of dunes, *in* Proceedings of the 2013 International Association for Hydro-Environment Engineering and Research Congress, Chengdu, China, 8–13 September: Beijing, Tsinghua University Press, Abstract 10079.

Schindler, R.J., et al., 2015, Sticky stuff: Redefining bedform prediction in modern and ancient environments: Geology, v. 43, p. 399–402, doi:10.1130/G36262.1.

Sequeiros, O.E., Spinewine, B., Beaubouef, R.T., Sun, T., Garcia, M.H., and Parker, G., 2010, Bedload transport and bed resistance associated with density and turbidity currents: Sedimentology, v. 57, p. 1463–1490, doi:10.1111/j.1365-3091.2010.01152.x.

Southard, J.B., 1991, Experimental determination of bed-form stability: Annual Review of Earth and Planetary Sciences, v. 19, p. 423–455, doi:10.1146/annurev.ea.19.050191.002231.

Southard, J.B., and Boguchwal, L.A., 1990, Bed configuration in steady unidirectional water flows; Part 2, Synthesis of flume data: Journal of Sedimentary Research, v. 60, p. 658–679, doi:10.1306/212F9241-2B24-11D7-8648000102C1865D.

Talling, P.J., 2013, Hybrid submarine flows comprising turbidity current and cohesive debris flow: Deposits, theoretical and experimental analyses, and generalized models: Geosphere, v. 9, p. 460–488, doi:10.1130/GES00793.1.

Venditti, J.G., Church, M.A., and Bennett, S.J., 2005, Bed form initiation from a flat sand bed: Journal of Geophysical Research, v. 110, F01009, doi:10.1029/2004JF000149.

Venditti, J.G., Church, M., and Bennett, S.J., 2006, On interfacial instability as a cause of transverse subcritical bed forms: Water Resources Research, v. 42, W07423, doi:10.1029/2005WR004346.

Walker, R.G., 1965, The origin and significance of the internal sedimentary structures of turbidites: Proceedings of the Yorkshire Geological Society, v. 35, p. 1–32, doi:10.1144/pygs.35.1.1.

Williams, P.B., and Kemp, P.H., 1971, Initiation of ripples on a flat sediment bed: Journal of Hydraulic Engineering, v. 97, p. 502–522.

Xu, J.P., Sequeiros, O.E., and Noble, M.A., 2014, Sediment concentrations, flow conditions, and downstream evolution of two turbidity currents, Monterey Canyon, USA: Deep Sea Research, Part I: Oceanographic Research Papers, v. 89, p. 11–34, doi:10.1016/j.dsr.2014.04.001.

Manuscript received 22 September 2014
Revised manuscript received 15 June 2015
Manuscript accepted 12 July 2015

Printed in USA

APPENDIX B: ARTICLE 2

Although the inclusion of this article may seem out of context, it is reflection on how the scope of this project has evolved during the intervening years. The initial objective of this Ph.D. was to compare and contrast the behavior of secondary currents in sub-aerial and submarine channel bends. Given that turbulence is the driving force behind maintaining sediment suspension, it seemed that establishing a baseline for the behavior of turbulence in the bends of open channel flows was a necessary precursor for the analysis. However objectives change, and while the implications of these findings are certainly important in terms of linking velocity fields to morpho-dynamic responses, this is an avenue that I have not been able to explore/exploit to its fullest potential. With this context, I encourage anyone to further explore the relationships between body forces and general turbulence/ theory.

B.1: Tilston, M., Rennie, C., Arnott, R.W.C., and Post, G. (2009). On the nature of coherent turbulent structures in channel bends: burst-sweep orientations in three-dimensional flow fields. 33rd IAHR Congress: Water Engineering for a Sustainable Environment. 851-858.

On the Nature of Coherent Turbulent Structures in Channel Bends: Burst-Sweep Orientations in Three-Dimensional Flow Fields

M. Tilston[1], C. Rennie[2], R.W.C. Arnott[1] and G. Post[3]

[1]Department of Earth Sciences, University of Ottawa, Ottawa ON, [2]Department of Civil Engineering, University of Ottawa, Ottawa ON, [3]Northwest Hydraulic Consultants Ltd.

Abstract

It is widely accepted that natural flows are characterized by coherent turbulent structures, known as bursts and sweeps, which transfer fluid momentum across local velocity gradients. While these have been the subject of extensive laboratory and field investigations, no studies have attempted to address their characteristics in channel bends. In part, this is related to the existing analytical frameworks, which are inherently two dimensional. The objectives of this study are to a) develop a fully three-dimensional scheme for analysing coherent turbulent structures; b) investigate the orientation of bursts and sweeps in an experimental channel bend. This involves solving the Reynolds tensor and performing octant analysis in lieu of conventional two-dimensional approaches. Results indicate that bursts and sweeps lack a preferred orientation upstream and downstream of the bend. However, flow in the channel bend strongly displays inner-bank oriented bursts and outer-bank oriented sweeps. These findings suggest that burst-sweep orientations are controlled by vertical gradient of the cross-stream velocity component and turbulence generated fluctuations in the cross-stream force balance.

Introduction

All river systems are characterized by three-dimensional, turbulent flow fields and perhaps no other fluvial environment better illustrates the fundamental role of secondary currents on channel morphology and evolution than meander loops. Their unique forms are a direct result of helical flow fields, and continue to be the subject of intensive study attempting to relate flow structure, sediment transport (Bridge and Jarvis, 1982; Dietrich and Whiting, 1989) and channel evolution (Rhoads and Welford, 1991; Darby and Delbono, 2002). However, there is one flow process that has been largely overlooked in the context of channel bends: coherent turbulent structures.

The most basic feature of turbulent flows are rotating eddies, which serve to transfer momentum through the water column. This mixing is accomplished as the leading edge of an eddy brings high momentum fluid from the upper part of the flow towards the bed, whereas the opposite occurs along the tailing half of the eddy (Schvidchenko and Pender, 2001). Taken together, these two types of fluid motions are known as “sweeps” and “bursts”, respectively, and represent the physical basis of the Reynolds stress. Historically, these types of motions are studies by using quadrant analysis (Willmarth and Lu, 1971) where bursts correspond to quadrant 2 events and sweeps correspond with quadrant 4 events.

By definition, this is a two-dimensional analytical framework that is unable to fully capture the dynamics of turbulent fluid motions in highly three-dimensional flow fields. The objectives of this study are; a) develop a fully three-dimensional scheme for analysing coherent turbulent structures; and b) investigate the orientation of bursts and sweeps in an experimental channel bend. This involves solving the Reynolds tensor and using an octant framework in lieu of the principal Reynolds stress and a quadrant framework.

33rd IAHR Congress: Water Engineering for a Sustainable Environment

ISBN: 978-94-90365-01-1

Methodology

The measurements used for this research were collected in a model river bend in the Civil Engineering Hydraulics Laboratory at the University of Ottawa. The flume has a centerline length of 18.2 m, consisting of an initial 12.19 m straight section leading into a 135° bend followed by a second 2.44 m straight section. The channel is 1 meter wide with a radius of curvature of 1.5 m; this represents a relatively low radius of curvature to width ratio, thereby allowing for the rapid development of strong secondary currents. Bed sediments consisted of sub-angular particles (d_{50}=1.1 mm). The slope was set to 0.044%, the critical value for entrainment in the straight section required for maximum clear-water scour conditions. Six sections of velocity measurements (2 minute time series) collected using Nortek Vectrino ADVs (sampling rate of 200 Hz) are utilized the present analysis; 4 of these sections were located in the bend proper at 30° intervals (Post, 2007).

The most standard method for quantifying coherent structures in turbulent velocity signals is to perform quadrant analysis (Nezu and Nakagawa, 1993). Here, a velocity component at time t ($u_i(t)$) can be decomposed into a time-averaged term and an instantaneous fluctuation about the mean using the equation:

$$u_i(t) = \overline{u_i} + u_i'$$

Where $\overline{u_i}$ is the time averaged term and u_i' is the instantaneous fluctuation. Using this notation, the magnitude of the Reynolds shear tensor (τ) can be solved by the equation:

$$\tau = \sqrt{\tfrac{1}{2}\sum_{ij}(\tau_{ij}')^2} = \sqrt{\tfrac{1}{2}\sum_{ij}(-\rho u_i' u_j')^2}$$

Where τ_{ij}' represents the standard instantaneous Reynolds stress component.

Subsequently, an octant diagram can be used to identify burst-sweep orientation. Conceptually, an octant diagram can be thought of as two quadrant diagrams placed side by side, where one quadrant diagram represents all events with a positive cross-stream velocity fluctuation (u_v') and the other for cases where u_v' is negative (**Figure 1**). In this framework, an event with a positive

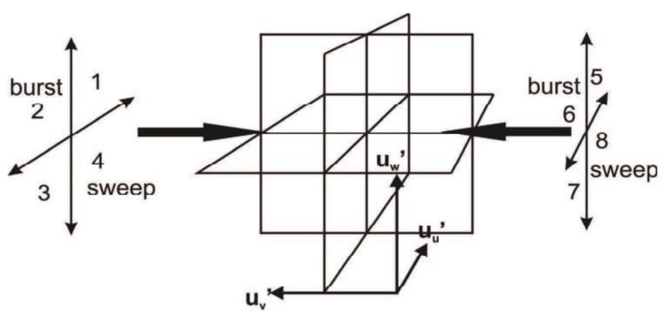

Figure 1: Octant framework for identifying burst-sweep orientation.

u_v' (inner bank orientation) corresponds with octants one through four, whereas octants 5 through 8 indicate a negative value of u_v'(outer bank orientation).

Results

Figure 2 presents the velocity and three components of the Reynolds stress through the study bend. Here, the velocity and Reynolds tensor data are normalized by the bend maxima to illustrate changes through the study bend, whereas the three planes of Reynolds stress are normalized by the sectional maxima to demonstrate tensor composition.

As flow travels around the bend, the high velocity core shifts towards the outer bank, decelerates and develops strong secondary currents. This is in agreement with previous field studies (Bridge and Jarvis, 1982). However, the high velocity core moves from the water surface to the lower third of the flow depth between the bend apex and exit and the area above the core is characterized by a weakly negative vertical velocity gradient. Currently the reasons for this are not completely understood, but might be a consequence of the tightness of the bend ($r_c / w = 1.5$). Interestingly, the Reynolds stress increases through the bend, reaching maximum levels at the 120° section. Yet, the more important result from this study is the tensor composition.

Upstream of the bend, the zone of maximum principal Reynolds stress (u_u'u_w') is found at the bed across the entire width of the channel and decreases towards the water surface. This is in agreement with previous studies (Song and Chiew, 2001). Although this trend persists through the bend, it is much weaker than the section upstream of the bend entrance and the upper portion of the flow is actually characterized by negative principal Reynolds stresses downstream of the

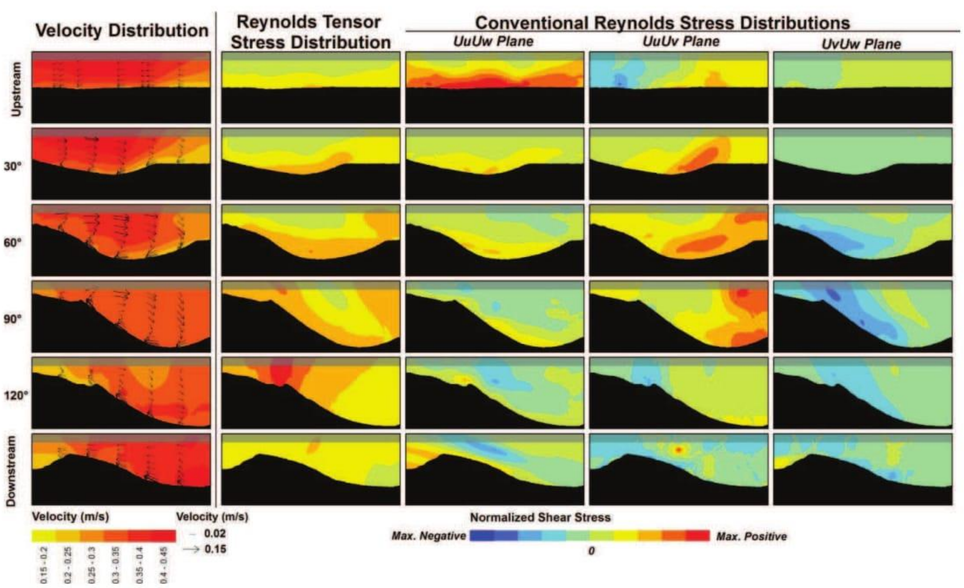

Figure 2: Velocity and shear stress distributions through the channel bend.

60° transect. The negative sign indicates directionality of momentum transfer and is associated with the lowering of the high velocity core. Interestingly, momentum exchange appears to be dominated by the $u_u'u_v'$ and $u_v'u_w'$ planes throughout the bend (Jamieson et al, in revision). Due to the reduction in the vertical gradient of u_u, the increased influence of these planes was anticipated; however, their dominance was not expected because previous bend flume studies using similar planform geometries have demonstrated that the dominant Reynolds stress is associated with the downstream-vertical plane (Blanckaert and Graf, 2001). This is likely related to the weakening of the vertical velocity (u_u) gradient above the near bed region, which drives fluid momentum exchange in this plane. Moreover, it may influence burst-sweep orientations.

Historically, burst-sweep analysis has focused on two key parameters: intensity and frequency (Willmarth and Lu, 1972). This type of analysis has been applied in the present study and extended to include the mean event impulse for examining burst-sweep orientations, which is the product of these two variables. In addition to the untreated data, a hole size filter (H=2) based on the cross-sectionally averaged tensor magnitude was applied to remove the effects of weaker turbulent motions. **Figure 3** and **Figure 4** present the patterns of burst and sweep orientations through the study bend. Here, the orientation ratio is defined as the relative effect of outward oriented bursts (octant 6) and sweeps (octant 8) with respect to the cumulative effect of all burst and sweep events. Thus, values of zero indicate that all bursts and sweeps display inner bank orientations within the time series, whereas values of 1 indicate an outer bank orientation.

In the regions upstream and downstream of the bend, event intensity and frequency ratios for

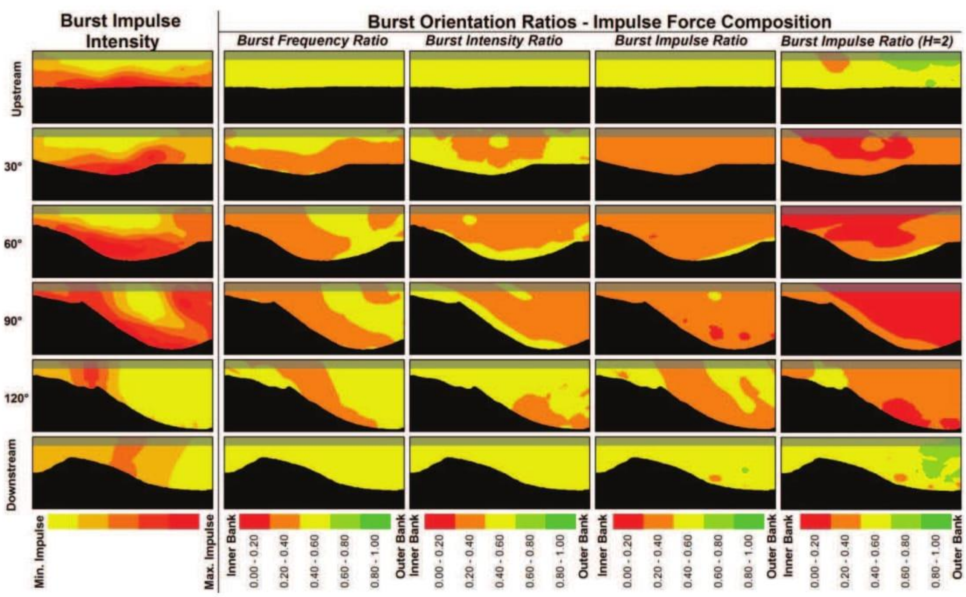

Figure 3: Burst orientation ratios. Red indicates a strong preference for inner bank orientation and green indicates a strong preference for outer bank orientation.

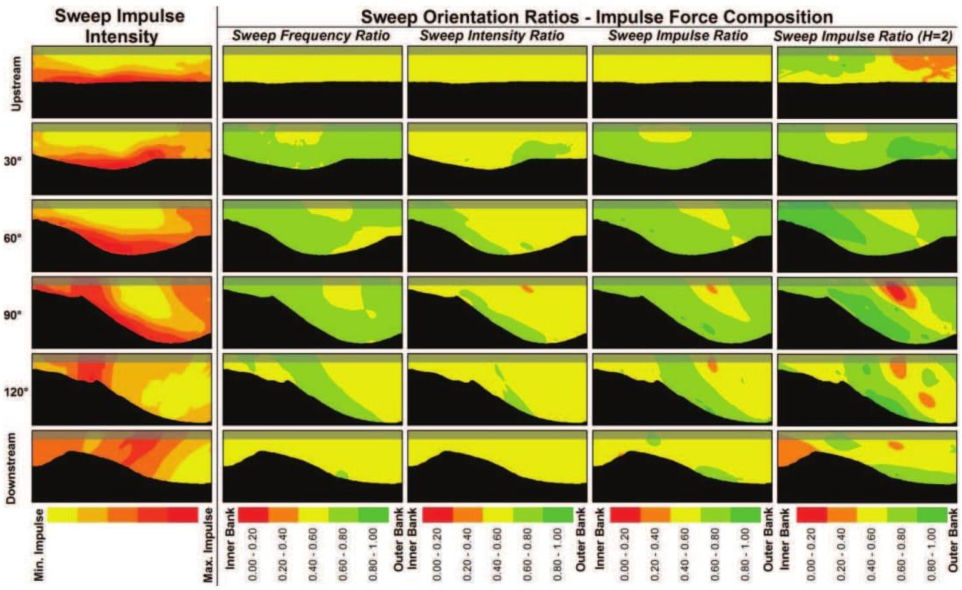

Figure 4: Sweep orientation ratios. Red indicates a strong preference for inner bank orientation and green indicates a strong preference for outer bank orientation.

bursts and sweeps range between 0.4 and 0.6. This suggests that both the ratio of inner-bank and outer-bank oriented turbulent motions are roughly equal in terms of strength and regularity. However, the situation is very different within the bend. Here, burst impulse ratios typically range between 0.2 and 0.4, demonstrating a preference for inner-bank orientation (**Figure 3**). This trend is further highlighted after applying the filter, where impulse ratios vary between 0 and 0.4 and appears to be a product of elevations in both frequency and intensity. Conversely, sweep impulse ratios generally range between 0.4 and 0.8, indicating a preference for outer-bank orientation (**Figure 4**). Again, impulse ratio patterns are enhanced upon filter application. Yet the trends seen in sweep orientation differ from bursts in two important ways. First, burst orientation appears to be largely controlled by event frequency rather than intensity. Secondly, impulse patterns are not as consistent as those of the bursts, and begin to show a reversal in orientation through the upper portions of flow in the 90° and 120° sections. Yet it is worth noting that these zones of reversed orientation coincide with those where impulse intensity is at a minimum and thus represent a small fraction of bulk momentum exchange within the section. This is probably an artifact of the weak vertical velocity gradient (u_u), hence turbulent fluid momentum exchange is being controlled locally by the $u_u'u_v'$ and $u_v'u_w'$ stress planes.

Discussion

The results demonstrate clearly that turbulent structures display a preferred orientation in channel bends, with bursts being oriented towards the inner bank and sweeps towards the outer bank. Given the well established links of the burst-sweep cycle with turbulent fluid momentum exchange, sediment transport and bedform development (e.g. Best, 1993), the presence of a preferred orientation represents an important finding. In order to understand the mechanisms controlling burst-sweep orientations, it is necessary to take a closer look at the stress distributions within the $u_u'u_v'$ and $u_v'u_w'$ planes.

It is well accepted that the nature of turbulent fluid momentum exchange, hence the sign associated with the time-averaged principal Reynolds stress, is directly related to that of local velocity gradients (Nezu and Nakagawa, 1993). Theoretically, this notion should also apply to the secondary stress planes, which is confirmed along the $u_u'u_v'$ plane upstream of the bend (**Figure 2**). Here, the region between the channel centerline and the inner bank are characterized by negative Reynolds stresses, whereas the region between the centerline and the outer-bank contain positive Reynolds stresses. This means that the $u_u'u_v'$ plane is characterized by high momentum fluid traveling towards the channel boundaries and low momentum fluid being brought towards the high velocity core (**Figure 5a**). However, the normal patterns of fluid momentum exchange clearly break down upon entering the bend. The 30° and 60° sections indicate that slow moving fluid moves towards the inner-bank and fast moving fluid is oriented towards the outer-bank, and therefore are independent of the cross-stream distribution of u_u. Similarly, one would expect the $u_v'u_w'$ plane to be characterized by the transfer of high momentum fluid from the near-surface and near bed regions towards the middle of the water column along the channel centerline; the reverse would be true for low momentum fluid. This process and anticipated stress distribution is presented in **Figure 5b**, yet results show that there is no reversal in sign associated with the Reynolds stress. Notwithstanding, both the observed $u_u'u_v'$ and $u_v'u_w'$ planes are similar to their theoretical distributions. Thus it would appear that there is an underlying process acting in channel bends that influences not only burst sweep orientations, but also turbulent momentum exchange along the $u_u'u_v'$ and $u_v'u_w'$ stress planes in channel bends. We propose that burst-sweep orientations in channel bends can be attributed to

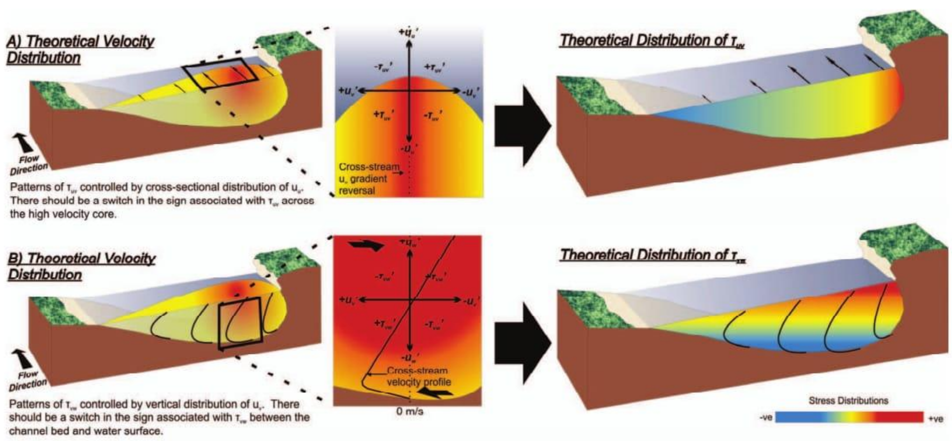

Figure 5: Theoretical velocity and stress distributions for the a) $u_u'u_v'$ and b) $u_v'u_w'$ planes.

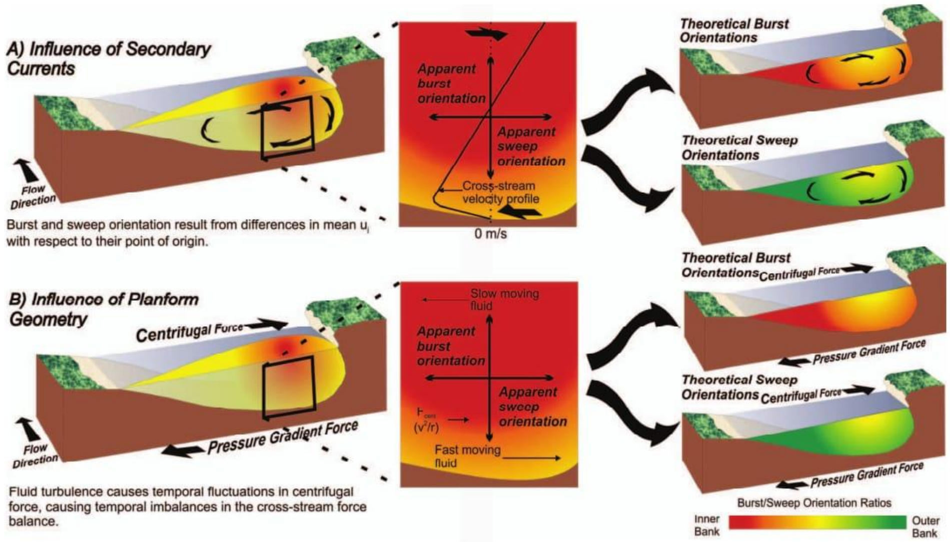

Figure 6: Conceptual models illustrating the roles of a) secondary currents and b) planform geometry on burst-sweep orientations in channel bends.

two factors: 1) the presence of strong secondary currents; and 2) channel planform geometry.

Strong secondary current can affect burst-sweep orientations due to a strong vertical gradient in u_v (**Figure 6a**). As a burst brings slow moving up through the water column, mean values of u_v become progressively more oriented towards the outer bank with respect to those at its point of origin. Therefore a burst would appear to be travelling towards the inner bank with respect to the mean value of u_v at the point of measurement. The reverse would be true for sweeps. Alternatively, burst-sweep orientation could also be modifying the cross-stream force balance associated with planform geometry (**Figure 6b**). While the pressure gradient force would remain relatively constant, centrifugal force would not since it is entirely dependent on velocity. Given that bursts are associated with slow moving fluid, they would cause a reduction in centrifugal force and result in inner-bank orientation. Conversely, fast moving sweeps would increase the centrifugal component of the force balance and result in outer-bank orientation. Each of these processes would lead to inner-bank bursting and outer-bank sweeping motions throughout the cross-section.

Determining the relative contribution of these two mechanisms has proven difficult. Results for the 120° section show a strong correlation between vertical gradients of u_v and a preferred orientation. However, this is also the section where u_u is at a minimum, and therefore the section with minimum centrifugal force. Moreover, the upper portions of flow in the 30° and 60° sections illustrate that sweeps show an outer-bank orientation despite the weak vertical gradient of u_v. Therefore, it would appear that the dominant mechanism controlling burst-sweep orientation is dependent on the intensity of u_u' with respect to the vertical gradient of u_v.

Conclusion

In this study we have developed a novel technique for analyzing coherent turbulent structures in three-dimensional flow fields. Results indicate that bursting motions are preferentially oriented towards the inner-bank, whereas sweeping motions are preferentially oriented towards the outer-bank. We believe this phenomenon can be attributed to temporal imbalances in the cross-stream force balance associated with the passage of turbulent structures and changes in mean cross-stream velocity through the water column associated with secondary currents. Future work should be conducted in different environments such as river confluences to properly asses the influence of secondary currents versus planform geometry.

References

Best, J.L. (1993). "On the interactions between turbulent flow structure, sediment transport and bedform development: some considerations from recent experimental research." *Turbulence: Perspectives on flow and sediment transport.* Clifford, N., French, J.R. and Hardisty, J., eds. Wiley and Sons Ltd. New York, NY.

Bridge, J.S. And Jarvis, J. (1982). "The dynamics of a river bend: a study of flow and sedimentary processes." *Sedimentology*. 29, 499-541.

Darby, S.E. and Delbono, I. (2002). A model of equilibrium bed topography for meander bends with erodible banks. *Earth Surface Processes and Landforms.* 27, 1057-1085.

Dietrich, W.E., and Whiting, P.J. (1989). "Boundary shear stress and sediment transport in river meanders of sand and gravel." *River Meandering, Water Resour. Monogr. Ser. 12.* Ikeda, S. And Parker, G. Eds. American Geophysical Union. Washington D.C.

Jamieson, E., Post, G., Rennie, C.D. "Spatial variability of three dimensional Reynolds stresses in a developing channel bend", *Earth Surface Processes and Landforms*, in revision.

Nezu, I., and Nakagawa, H. (1993). *Turbulence in Open Channel Flows.* Brookfield, VT.: A.A. Balkema.

Post, G. (2007). "The Measurement of Reynolds Stresses in a Model River Bend using Acoustic Doppler Velocimeters." M.A.Sc.Thesis, Univ. of Ottawa, Ottawa, On.

Rhoads, B.L. and Welford, M.R. (1991). "Initiation of river meandering." *Progress in Physical Geography.* 15(2), 127-156.

Schvidchenko, A. B. and Pender, G. (2001). "Macroturbulent structure of open-channel flow over gravel beds." Water Resour. Res. 37, 709–719.

Willmarth, W.W. and Lu, S.S. (1972). "Structure of the Reynolds stress near the wall". *J. Fluid Mech.* 55(1) 65-92.

APPENDIX C: COMPUTED TOMOGRAPGY (CT)

C.1: Principles of Use and Operation

Instantaneous density images were collected using a medical grade CT scanner -- a technique that is increasingly being exploited by the scientific and engineering community as it offers three advantages over more conventional instrumentation, including: 1) it is non-intrusive and capable of measuring subtle density differences across a variety of media; 2) the spatial resolution of the measured density differences and the output images are unparalleled; 3) the resulting data is devoid of calibration errors (Ketcham & Carlson, 2001). While a costly and highly sophisticated piece of instrumentation, the principles of operation are surprisingly simple and based solely on the attenuation of x-ray intensity as it passes through a medium. This is largely a function of the elemental density in homogeneous media, or compound density in the case of heterogeneous media like particle gravity currents, and sample thickness. The basic equation to describe the degree of attenuation is summarized in Beer's law

$$I = I_o exp(\mu x) \ , \qquad \text{C.1.}$$

Where I_o, μ and x are the intensity of the emitted x-ray, the linear attenuation coefficient of the sampled material, and the thickness of the material, respectively (Duchesne et al., 2009). As such, the sample sits between a paired x-ray emitter and receiver that rotate around the sample to obtain a series of density strips, which subsequently are reconstructed into a cross-sectional image using proprietary software.

The CT scanner images used in this study are oriented perpendicular to the primary flow axis, providing a cross-sectional image of current density that consists of 512×512 voxels, which is the equivalent to a pixel, but also with a third dimension owing to the width of the receiver. The number of voxels remains constant regardless of the dimensions of the reconstructed image, as does its physical dimension perpendicular to the sensors (0.6 mm). As the flume's cross-sectional dimension is 300×300 mm, the volume of each voxel in the reconstructed image is $0.6 \times 0.6 \times 0.6$ mm.

Being a medical grade CT scanner, there is a legitimate concern about radiation exposure to the patient, and as a consequence there is an internal automatic shut-off the system to prevent over-exposure. This maximum exposure rate is a function of the energy of the emitted x-rays (I_o), where higher energies are needed to penetrate denser materials, in addition to longer exposure times. Consequently, setting the instrument's sampling frequency requires a balance between the x-ray energy needed to penetrate the current and an approximation of current duration to sample the full anatomy of the flow. In this study, current duration is limited by the volume of the slurry in the mixing tanks (~ 0.6 m^3) and resulted in flow durations of ~30 s, and so the optimal sampling frequency for adequate x-ray penetration while sampling the full anatomy of the current is ~2 Hz.

C.2: Data Treatment

Notwithstanding the potentially revolutionary insight afforded by CT imagery, artifacts are omnipresent in most CT images, and therein the potential to obscure or obfuscate the primary signal. This is especially problematic in the case of particle-driven gravity flows where artifact-generated density fluctuations are commonly an order of magnitude greater than the density contrast between the current and the ambient fluid; the maximum particle diameter used herein is 0.33 mm, substantially smaller (~50%) than the voxel dimension, and given flow velocities of ~0.6 m/s and the CT scanner's sampling frequency of 2 Hz, the spatio-temporal averaging effects of the CT scanner mean that it the sample volume is too large to resolve individual grains, and as a result, the output is a bulk average of the fluid and the grains.

In this study I identify two principal sources of image artifacts: 1) Poisson noise, which results from an excessive number of photons being attenuated before reaching the receiver, resulting in statistical errors during image reconstruction, and; 2) beam hardening, where low energy photons are disproportionately attenuated while passing through high density substances like the flume's acrylic walls, high density photons on the other hand are little affected (Boas & Fleischmann, 2012). These two processes introduce high and low frequency artifacts, respectively. As these are common problems, and recalling the rotational nature of the CT scan's operation, most studies attempt to mitigate these issues by focusing on the spherical component of the image. This allows for the density image to be converted from a Cartesian to a polar co-ordinate system, and then a Fourier transform used to identify and eliminate artifacts (Munch et al., 2009). However since the flume used here is square in cross-section, and the significant density difference between the flume (and its contents) and ambient air, the aforementioned artifact removal technique.

To compensate for these problems a novel technique was developed using the two-dimensional stationary wavelet transform (2D-SWT) to remove artifacts from the image. This technique works much like the continuous wavelet transform outlined in **Chapter 2**, except uses a smaller number of decomposition levels (2^n) to increase computational efficiency, and calculates spectral energy distributions for the horizontal, vertical and diagonal axes of each image pixel. This, then, makes it is possible to filter the image based on the frequency, as well as the spectral energy of each frequency by omitting them from the reconstructed image. A sensitivity analysis shows that the success of artifact removal depends on three factors: 1) choice of the mother wavelet; 2) maximum wavelet scale used in the decomposition; and 3) choice of filtering technique.

Since the principal source of image noise is from the flume itself, the sensitivity analysis is performed in each run and on the first set of images that are captured prior to the arrival of the current head. The calculated image reconstruction coefficients are then applied uniformly to each subsequent image in the dataset to maintain consistence in the reconstruction process. An example of the initial and filtered images is shown in Figure C-1. A few years following this work, a published report using a similar approach, and a suite of sensitivity analyses concluded that both our choice of mother wavelet and filtering technique are the most appropriate (see: Sahu & Choubey, 2014).

Following this procedure, images are converted from their native Houndsville units (HU), where the density of air and water are $-1000\ HU$ and $0\ HU$, respectively, to kg/m^3using the equation

$$\rho = 0.0257\left(\frac{HU + 1024}{1000}\right)^2 + 1.0209\left(\frac{HU + 1024}{1000}\right) - 0.0254\,. \quad \text{C.2.}$$

Details of this conversion process are detailed in Long and Montreuil (2011).

C.3: References

Boas, F. E., & Fleischmann, D. (2012). CT artifacts: causes and reduction techniques. *Imaging in Medicine, 4*(2), 229-240. doi: 10.2217/iim.12.13

Duchesne, M. J., Moore, F., Long, B. F., & Labrie, J. (2009). A rapid method for converting medical Computed Tomography scanner topogram attenuation scale to Hounsfield Unit scale and to obtain relative density values. *Engineering Geology, 103*(3-4), 100-105. doi: DOI 10.1016/j.enggeo.2008.06.009

Ketcham, R. A., & Carlson, W. D. (2001). Acquisition, optimization and interpretation of X-ray computed tomographic imagery: applications to the geosciences. *Computers & Geosciences, 27*(4), 381-400. doi: Doi 10.1016/S0098-3004(00)00116-3

Long, B., & Montreuil, S. (2011). Evolution of Ripple Field Architecture during Sediment Transport, as Measured by CT Scanning. In S. S. Ginsberg (Ed.), *Sediment Transport* (pp. 237-260): InTech.

Munch, B., Trtik, P., Marone, F., & Stampanoni, M. (2009). Stripe and ring artifact removal with combined wavelet--Fourier filtering. *Opt Express, 17*(10), 8567-8591. doi: 10.1364/oe.17.008567

Sahu, J., & Choubey, A. (2014). A Procedural Performance Comparison of Soft Thresholding Techniques for Medical Image Denoising. *International Journal of Computer Trends and Technology, 10*(5), 232-235. doi: 10.14445/22312803/ijctt-v10p141

C.4: List of Figures

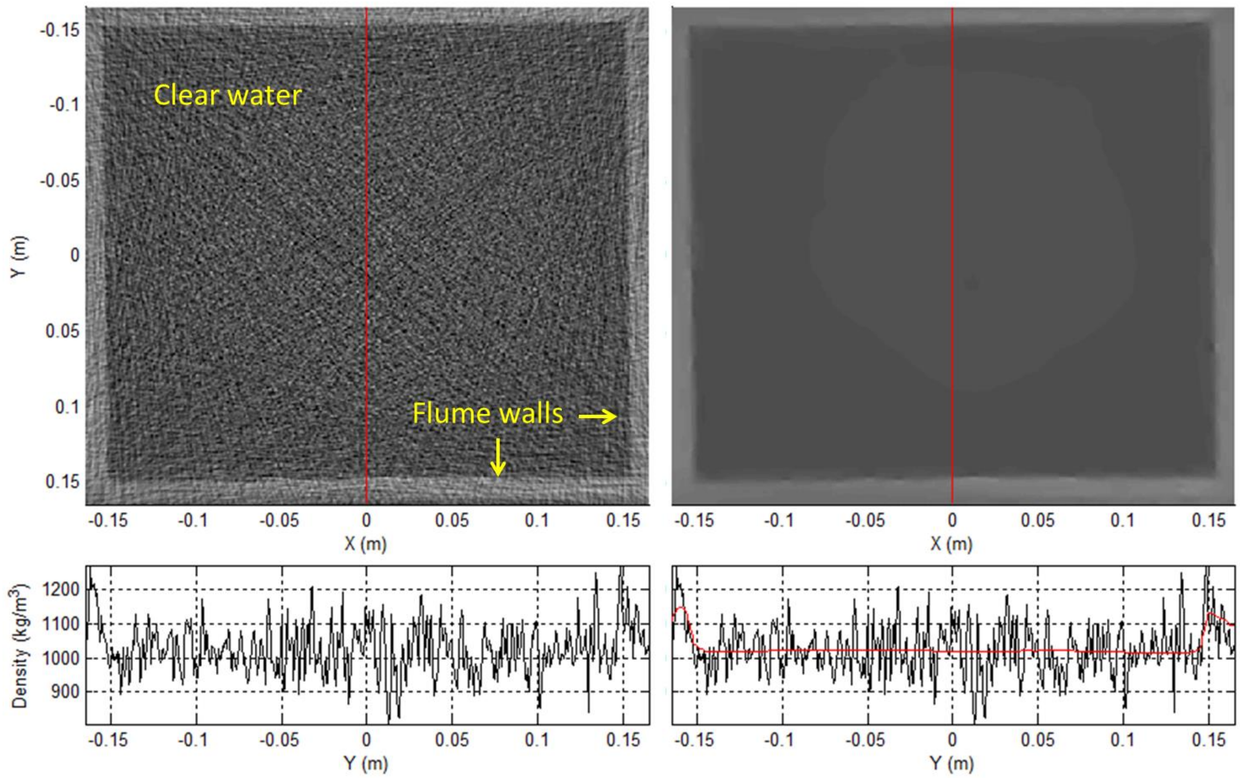

Figure C-1: Comparison of (left) raw density image from the CT scan and (right) de-noised image after applying the 2D-SWT filter. The red lines show the position of the density profiles at the bottom of the figure.

APPENDIX D: ULTRACONIC DOPLER VELOCIMETRY

D.1: Principles of Use and Operation

Three-dimensional velocity data were collected using an ultrasonic Doppler velocimetry profiler (UDVP-3D) by Signal Processing SA. Like conventional acoustic velocimetry, the UDVP-3D relies on the coherent pulse pair technique to derive fluid velocity (Lhermitte & Serafin, 1984; Miller & Rochwarger, 1972; Zedel & Hay, 2002; Zedel et al., 1996). Here, the velocity along the bistatic beam axis (u_b) is

$$u_b = \frac{c\left(\overline{d\theta/d\tau}\right)}{4\pi f_o} \text{ ,} \qquad \text{D.1.}$$

and the distance between the sensor and the centroid of the sampling volume is

$$D = \frac{c\tau_D}{2} \text{ ,} \qquad \text{D.2.}$$

where c is the speed of sound, τ the time lag between pulses, θ the Doppler phase shift between the received pulse pair, f_o the operating frequency of the instrument and τ_D the time lag between pulse emission and backscatter reception . The term $\overline{d\theta/d\tau}$ is calculated from the correlations of multiple pulse pairs by estimating the slope of the auto-covariance function at zero lag (Miller & Rochwarger, 1972). The UDVP-3D allows the user to specify duration of a single pulse, which controls sample volume thickness, and number of pulse pairs used in the calculation of $\overline{d\theta/d\tau}$, which defines the degree of confidence in estimations of u_b. Here, pulse duration was set at $2/f_o$ to maximize spatial resolution, and $\overline{d\theta/d\tau}$ was calculated using 9 unique pulse pairs per receiving transducer, and therefore 27 pulse pairs per instantaneous Cartesian velocity measurement. The key advantage of the UDVP-3D over most laboratory acoustic instruments is its lower operating frequency (f_o = 2MHz), which is less prone to signal attenuation and therefore ideal for sampling highly concentrated particle gravity flows.

The UDVP-3D itself consists of a central emitter and three passive receivers, but the user is able to pick the optimal transducer characteristics and probe geometry for the given application. Here, the goal was to minimize spatial and temporal averaging, while covering the full depth of the flume. For a given f_o, beamwidth is governed by transducer diameter, thus spatial averaging in the plane perpendicular to the emitter axis is reduced by minimizing the beamwidth of the emitting transducer, whereas maximizing the beamwidth of the receiving transducers results in a longer velocity profile. In these experiments, probe diameters of 10 mm and 5 mm, or beamwidths of 5.2° and 9.6° were used for the emitting and receiving transducers, respectively. Thus the diameter of the sampling volume in the plane perpendicular to the emitter's beam axis in the near-field (d_{nf}) where beam spreading is negligible is equivalent to the diameter of the emitting transducer, and the vertically averaged diameter in the far-field (d_{ff}) is

$$d_{ff} = d_{nf} + 2\left(D - D_{nf}\right)\tan\theta \ , \qquad \text{D.3.}$$

where θ is the beamwidth of the emitting transducer and D_{nf} is the distance between the emitting transducer and the transition from near-field to far-field beam characteristics, which is defined as

$$D_{nf} = f_o {d_{nf}}^2/4c \ , \qquad \text{D.4.}$$

The maximum sampling distance and velocities of the UDVP-3D are determined by the time lag between pulses (τ) such that reducing the time between pulses increases the maximum observable, or ambiguity velocity at the expense of total profile length (Pinkel, 1980). Maximum profile length (D_{max}) is defined as

$$D_{max} = \frac{c\tau}{2} \ , \qquad \text{D.5.}$$

and the ambiguity velocity ($u_{b\,max}$) is

$$u_{b\,max} = \pm\frac{c}{4\tau_r f_o} \ , \qquad \text{D.6.}$$

where τ_r is the time lag between received pulses and $u_{b\,max}$ is the maximum velocity along the bistatic beam axis. It is worth noting that the pulse emission frequency (τ^{-1}) that defines D_{max} is not equivalent to the pulse reception frequency (τ_r^{-1}) that defines $u_{b\,max}$ in the UDVP-3D since the receiving transducers act in series rather than parallel (see below). Additionally, while $u_{b\,max}$ is constant for all bistatic beam axes and sampling distances, the ambiguity velocity in Cartesian coordinates will vary with sampling position.

As previously noted, the velocity profiles of turbidity currents are similar to those of wall-bounded jets; thus unlike open channel flow, the high velocity core is located at the base rather than the top of the flow. Consequently, I opted for a downward looking probe orientation so that the Cartesian ambiguity velocities would increase with sampling distance and to minimize flow disturbance. The three receiving transducers were oriented radially around the emitting transducers (radius of 47 mm) at intervals of 120° (α) and 13° off of vertical along their radial axis; with this setup. The blanking distance between the emitter and the first sampling position (49 mm) is greater than the near-field region calculated from **equation D.4** (~35 mm), and therefore the sampling volume diameter increases from ~30 mm to ~53 mm between the first and last ($D \cong 300$ mm) sampling positions. Pulse emission frequency (τ^{-1}) was set to 792 Hz as this covered the entire depth of the flume while maximizing the ambiguity velocity ($\tau_r^{-1} = \tau^{-1}/3$; $u_{b\ max} \cong \pm 14.3$ cm/s) and after averaging the phase shift over 12 pulse pairs, instantaneous Cartesian velocities were acquired at a rate of ~22.1 Hz. Emission power and reception sensitivity of the transducers were adjusted through an iterative process so that only particle laden fluid resulted in Doppler reflections; this is the only way to identifying the arrival of the current head directly from the velocity data, however it also means I am measuring particle rather than fluid velocity. Although the experimental current lasted 45 seconds, the sampling duration was 90 seconds and was subsequently cropped from 10 seconds prior to the arrival of the head and 10 seconds after the passage of the tail. The extraneous portions at the beginning and end of the velocity data were maintained to minimize the cone of influence effects associated with the CWT.

D.2: Data Treatment

Data were first treated to ensure that the velocity data had not been phase-wrapped. This artifact occurs when the true particle velocity exceeds the ambiguity velocity; thus the Doppler phase shift in **equation D.6** exceeds $\pm\pi$ and the true phase shift is 2π greater than the recorded value, which is equivalent to $2u_{b\ max}$. (Rennie and Hay (2010)) encountered this problem and developed a novel algorithm to unwrap corrupted data by comparing the instantaneous beam velocities against the local mean, then adding the appropriate factor of $u_{b\ max}$ to correct the signal prior to converting from beam to Cartesian velocities. A similar approach was adopted here. Note that the default format of the UDVP-3D is Cartesian coordinates, thus measured velocities were converted to bistatic beam coordinates as the nature and extent of phase-wrapping may vary between the three receiving transducers.

A three-component bistatic beam coordinate system is resolved using a 3 × 3 transformation matrix (T_φ) that depends on probe configuration and the bistatic beam angle (φ), which varies with distance between the emitting transducer and the centroid of the sampling volume

$$\begin{bmatrix} u_{b_1} \\ u_{b_2} \\ u_{b_3} \end{bmatrix} = T_\varphi \begin{bmatrix} u_x \\ u_y \\ u_z \end{bmatrix} \quad , \qquad \text{D.7.}$$

where u_{b_1}, u_{b_1}, and u_{b_1} are the velocities along the three bistatic beam axes; u_x, u_v, and u_w represent velocities for the longitudinal, lateral and vertical directions, respectively. For the UDVP-3D configuration used in the present study, the transformation matrix is

$$T_\varphi = \begin{bmatrix} \cos\left(\alpha - \frac{5\pi}{6}\right)\sin\varphi & \sin\left(\alpha - \frac{5\pi}{6}\right)\sin\varphi & \cos\varphi \\ \cos\left(\alpha - \frac{\pi}{6}\right)\sin\varphi & \sin\left(\alpha - \frac{\pi}{6}\right)\sin\varphi & \cos\varphi \\ \cos\left(\alpha + \frac{\pi}{2}\right)\sin\varphi & \sin\left(\alpha + \frac{\pi}{2}\right)\sin\varphi & \cos\varphi \end{bmatrix} \quad , \qquad \text{D.8.}$$

where α is $4\pi/6$ (120°). Cartesian velocities can be calculated by deriving the inverse of the transformation matrix ($T_\varphi{}'$); for which it is helpful to expand **equation 8** into a common angle

$$T_\varphi = \begin{bmatrix} \left(-\cos\alpha\cos\frac{\pi}{6} + \sin\alpha\sin\frac{\pi}{6}\right)\sin\varphi & \left(-\sin\alpha\cos\frac{\pi}{6} - \cos\alpha\sin\frac{\pi}{6}\right)\sin\varphi & \cos\varphi \\ \left(\cos\alpha\cos\frac{\pi}{6} + \sin\alpha\sin\frac{\pi}{6}\right)\sin\varphi & \left(\sin\alpha\cos\frac{\pi}{6} - \cos\alpha\sin\frac{\pi}{6}\right)\sin\varphi & \cos\varphi \\ (-\sin\alpha)\sin\varphi & \cos\alpha\sin\varphi & \cos\varphi \end{bmatrix} \quad , \qquad \text{D.9.}$$

the inverse matrix is

$$
T'_{\varphi} = \begin{bmatrix} \dfrac{1/\cos\alpha - \sin\alpha\left(\sin\frac{\pi}{6}+1\right)/\cos\frac{\pi}{6} - \cos\alpha}{2\sin\varphi\tan\alpha\left(\sin\frac{\pi}{6}+1\right)} & \dfrac{1/\cos\alpha + \sin\alpha\left(\sin\frac{\pi}{6}+1\right)/\cos\frac{\pi}{6} - \cos\alpha}{2\sin\varphi\tan\alpha\left(\sin\frac{\pi}{6}+1\right)} & \dfrac{\cos\alpha - 1/\cos\alpha}{\sin\varphi\tan\alpha\left(\sin\frac{\pi}{6}+\right.} \\ \dfrac{-\sin\alpha\left(\sin\frac{\pi}{6}+1\right)/\cos\frac{\pi}{6} - \cos\alpha}{2\sin\varphi\left(\sin\frac{\pi}{6}+1\right)} & \dfrac{\sin\alpha\left(\sin\frac{\pi}{6}+1\right)/\cos\frac{\pi}{6} - \cos\alpha}{2\sin\varphi\left(\sin\frac{\pi}{6}+1\right)} & \dfrac{\cos\alpha}{\sin\varphi\left(\sin\frac{\pi}{6}+1\right)} \\ \dfrac{1}{2\cos\varphi\left(\sin\frac{\pi}{6}+1\right)} & \dfrac{1}{2\cos\varphi\left(\sin\frac{\pi}{6}+1\right)} & \dfrac{\sin\frac{\pi}{6}}{\cos\varphi\left(\sin\frac{\pi}{6}+1\right)} \end{bmatrix} \quad \text{D}
$$

It should be noted that the default orientation of u_w is positive away from the sensor (towards the bed) following the right-hand rule. This was converted into the conventional right-hand coordinate system with positive u_w oriented away from the bed prior to data presentation.

D.3: Transformation Matrix Derivation

The following re-arrangements are used to reduce all the varying angles in **equation D.8** to a single angle to aid in derivation of the inverse transformation matrix in **equation D.10**. First, the bracketed angles in **equation D.8** are expanded to give

$$
\begin{bmatrix} \left(\cos\alpha\cos\frac{5\pi}{6} + \sin\alpha\sin\frac{5\pi}{6}\right)\sin\varphi & \left(\sin\alpha\cos\frac{5\pi}{6} - \cos\alpha\sin\frac{5\pi}{6}\right)\sin\varphi & \cos\varphi \\ \left(\cos\alpha\cos\frac{\pi}{6} + \sin\alpha\sin\frac{\pi}{6}\right)\sin\varphi & \left(\sin\alpha\cos\frac{\pi}{6} - \cos\alpha\sin\frac{\pi}{6}\right)\sin\varphi & \cos\varphi \\ \left(\cos\alpha\cos\frac{\pi}{2} - \sin\alpha\sin\frac{\pi}{2}\right)\sin\varphi & \left(\sin\alpha\cos\frac{\pi}{2} + \cos\alpha\sin\frac{\pi}{2}\right)\sin\varphi & \cos\varphi \end{bmatrix}, \quad \text{D.11.}
$$

Recalling that $\cos(\pi/2) = 0$ and $\sin(\pi/2) = 1$, the thrid row can be simplified, yielding

$$
\begin{bmatrix} \left(\cos\alpha\cos\frac{5\pi}{6} + \sin\alpha\sin\frac{5\pi}{6}\right)\sin\varphi & \left(\sin\alpha\cos\frac{5\pi}{6} - \cos\alpha\sin\frac{5\pi}{6}\right)\sin\varphi & \cos\varphi \\ \left(\cos\alpha\cos\frac{\pi}{6} + \sin\alpha\sin\frac{\pi}{6}\right)\sin\varphi & \left(\sin\alpha\cos\frac{\pi}{6} - \cos\alpha\sin\frac{\pi}{6}\right)\sin\varphi & \cos\varphi \\ -\sin\alpha\sin\varphi & \cos\alpha\sin\varphi & \cos\varphi \end{bmatrix}, \quad \text{D.12.}
$$

Finally, the remaining $\frac{5\pi}{6}$ angles can be re-arranged into a common angle of $\frac{\pi}{6}$, giving the matrix we are trying to find the inverse of, as seen in **equation D.9**. Now it is possible to find the inverse of the transform matrix; putting **equation D.9** into the standard format for a transform, we begin with:

$$\begin{bmatrix} \left(-\cos\alpha\cos\frac{\pi}{6}+\sin\alpha\sin\frac{\pi}{6}\right)\sin\varphi & \left(-\sin\alpha\cos\frac{\pi}{6}-\cos\alpha\sin\frac{\pi}{6}\right)\sin\varphi & \cos\varphi \\ \left(\cos\alpha\cos\frac{\pi}{6}+\sin\alpha\sin\frac{\pi}{6}\right)\sin\varphi & \left(\sin\alpha\cos\frac{\pi}{6}-\cos\alpha\sin\frac{\pi}{6}\right)\sin\varphi & \cos\varphi \\ -\sin\alpha\sin\varphi & \cos\alpha\sin\varphi & \cos\varphi \end{bmatrix}\begin{bmatrix} 1 & 0 & 0 \\ 0 & 1 & 0 \\ 0 & 0 & 1 \end{bmatrix}, \quad \text{D.13.}$$

where the goal to manipulate the LHS matrix until it is identical to the RHS matrix at present, at which point the RHS matrix is the inverse. We begin by adding row 2 to row 1, which gives

$$\begin{bmatrix} 2\sin\alpha\sin\frac{\pi}{6}\sin\varphi & -2\cos\alpha\sin\frac{\pi}{6}\sin\varphi & 2\cos\varphi \\ \left(\cos\alpha\cos\frac{\pi}{6}+\sin\alpha\sin\frac{\pi}{6}\right)\sin\varphi & \left(\sin\alpha\cos\frac{\pi}{6}-\cos\alpha\sin\frac{\pi}{6}\right)\sin\varphi & \cos\varphi \\ -\sin\alpha\sin\varphi & \cos\alpha\sin\varphi & \cos\varphi \end{bmatrix}\begin{bmatrix} 1 & 1 & 0 \\ 0 & 1 & 0 \\ 0 & 0 & 1 \end{bmatrix}, \quad \text{D.14.}$$

Next we divide $(row\ 1)/2$, and then subtract row 1 from row 2, giving

$$\begin{bmatrix} \sin\alpha\sin\frac{\pi}{6}\sin\varphi & -\cos\alpha\sin\frac{\pi}{6}\sin\varphi & \cos\varphi \\ \cos\alpha\cos\frac{\pi}{6}\sin\varphi & \sin\alpha\cos\frac{\pi}{6}\sin\varphi & 0 \\ -\sin\alpha\sin\varphi & \cos\alpha\sin\varphi & \cos\varphi \end{bmatrix}\begin{bmatrix} 0.5 & 0.5 & 0 \\ -0.5 & 0.5 & 0 \\ 0 & 0 & 1 \end{bmatrix}, \quad \text{D.15.}$$

To clear up the third column on the LHS matrix, we divide all rows by $\cos\varphi$

$$\begin{bmatrix} \sin\alpha\sin\frac{\pi}{6}\tan\varphi & -\cos\alpha\sin\frac{\pi}{6}\tan\varphi & 1 \\ \cos\alpha\cos\frac{\pi}{6}\tan\varphi & \sin\alpha\cos\frac{\pi}{6}\tan\varphi & 0 \\ -\sin\alpha\tan\varphi & \cos\alpha\tan\varphi & 1 \end{bmatrix}\begin{bmatrix} \frac{1}{2\cos\varphi} & \frac{1}{2\cos\varphi} & 0 \\ -\frac{1}{2\cos\varphi} & \frac{1}{2\cos\varphi} & 0 \\ 0 & 0 & \frac{1}{\cos\varphi} \end{bmatrix}, \quad \text{D.16.}$$

Next we subtract row 3 from row 1, which after tidying up the LHS gives

$$\begin{bmatrix} \sin\alpha\tan\varphi\left(\sin\frac{\pi}{6}+1\right) & -\cos\alpha\tan\varphi\left(\sin\frac{\pi}{6}+1\right) & 0 \\ \cos\alpha\cos\frac{\pi}{6}\tan\varphi & \sin\alpha\cos\frac{\pi}{6}\tan\varphi & 0 \\ -\sin\alpha\tan\varphi & \cos\alpha\tan\varphi & 1 \end{bmatrix}\begin{bmatrix} \frac{1}{2\cos\varphi} & \frac{1}{2\cos\varphi} & -\frac{1}{\cos\varphi} \\ -\frac{1}{2\cos\varphi} & \frac{1}{2\cos\varphi} & 0 \\ 0 & 0 & \frac{1}{\cos\varphi} \end{bmatrix}, \quad \text{D.17.}$$

and dividing row 1 and row 2 by $\sin\frac{\pi}{6}+1$ and $\cos\frac{\pi}{6}$, respectively to get

$$\begin{bmatrix} \sin\alpha\tan\varphi & -\cos\alpha\tan\varphi & 0 \\ \cos\alpha\tan\varphi & \sin\alpha\tan\varphi & 0 \\ -\sin\alpha\tan\varphi & \cos\alpha\tan\varphi & 1 \end{bmatrix}\begin{bmatrix} \frac{1}{2\cos\varphi\left(\sin\frac{\pi}{6}+1\right)} & \frac{1}{2\cos\varphi\left(\sin\frac{\pi}{6}+1\right)} & -\frac{1}{\cos\varphi\left(\sin\frac{\pi}{6}+1\right)} \\ -\frac{1}{2\cos\varphi\cos\frac{\pi}{6}} & \frac{1}{2\cos\varphi\cos\frac{\pi}{6}} & 0 \\ 0 & 0 & \frac{1}{\cos\varphi} \end{bmatrix}, \quad \text{D.18.}$$

Now we add row 1 to row 3 to remove the variables from the third row of the LHS matrix

$$\begin{bmatrix} \sin\alpha\tan\varphi & -\cos\alpha\tan\varphi & 0 \\ \cos\alpha\tan\varphi & \sin\alpha\tan\varphi & 0 \\ 0 & 0 & 1 \end{bmatrix} \begin{bmatrix} \frac{1}{2\cos\varphi\left(\sin\frac{\pi}{6}+1\right)} & \frac{1}{2\cos\varphi\left(\sin\frac{\pi}{6}+1\right)} & -\frac{1}{\cos\varphi\left(\sin\frac{\pi}{6}+1\right)} \\ -\frac{1}{2\cos\varphi\cos\frac{\pi}{6}} & \frac{1}{2\cos\varphi\cos\frac{\pi}{6}} & 0 \\ \frac{1}{2\cos\varphi\left(\sin\frac{\pi}{6}+1\right)} & \frac{1}{2\cos\varphi\left(\sin\frac{\pi}{6}+1\right)} & \frac{\sin\frac{\pi}{6}}{\cos\varphi\left(\sin\frac{\pi}{6}+1\right)} \end{bmatrix}, \quad \text{D.19.}$$

and divide rows 1 and 2 by $\tan\varphi$, which after cleaning up the terms in the RHS matrix gives

$$\begin{bmatrix} \sin\alpha & -\cos\alpha & 0 \\ \cos\alpha & \sin\alpha & 0 \\ 0 & 0 & 1 \end{bmatrix} \begin{bmatrix} \frac{1}{2\sin\varphi\left(\sin\frac{\pi}{6}+1\right)} & \frac{1}{2\sin\varphi\left(\sin\frac{\pi}{6}+1\right)} & -\frac{1}{\sin\varphi\left(\sin\frac{\pi}{6}+1\right)} \\ -\frac{1}{2\sin\varphi\cos\frac{\pi}{6}} & \frac{1}{2\sin\varphi\cos\frac{\pi}{6}} & 0 \\ \frac{1}{2\cos\varphi\left(\sin\frac{\pi}{6}+1\right)} & \frac{1}{2\cos\varphi\left(\sin\frac{\pi}{6}+1\right)} & \frac{\sin\frac{\pi}{6}}{\cos\varphi\left(\sin\frac{\pi}{6}+1\right)} \end{bmatrix}, \quad \text{D.20.}$$

Next, multiply row 2 by $\tan\alpha$

$$\begin{bmatrix} \sin\alpha & -\cos\alpha & 0 \\ \sin\alpha & \sin\alpha\tan\alpha & 0 \\ 0 & 0 & 1 \end{bmatrix} \begin{bmatrix} \frac{1}{2\sin\varphi\left(\sin\frac{\pi}{6}+1\right)} & \frac{1}{2\sin\varphi\left(\sin\frac{\pi}{6}+1\right)} & -\frac{1}{\sin\varphi\left(\sin\frac{\pi}{6}+1\right)} \\ -\frac{\tan\alpha}{2\sin\varphi\cos\frac{\pi}{6}} & \frac{\tan\alpha}{2\sin\varphi\cos\frac{\pi}{6}} & 0 \\ \frac{1}{2\cos\varphi\left(\sin\frac{\pi}{6}+1\right)} & \frac{1}{2\cos\varphi\left(\sin\frac{\pi}{6}+1\right)} & \frac{\sin\frac{\pi}{6}}{\cos\varphi\left(\sin\frac{\pi}{6}+1\right)} \end{bmatrix}, \quad \text{D.21.}$$

and subtract row 1 from row2. After cleaning up the LHS and RHS of the equation, this gives

$$\begin{bmatrix} \sin\alpha & -\cos\alpha & 0 \\ 0 & \frac{1}{\cos\alpha} & 0 \\ 0 & 0 & 1 \end{bmatrix} \begin{bmatrix} \frac{1}{2\sin\varphi\left(\sin\frac{\pi}{6}+1\right)} & \frac{1}{2\sin\varphi\left(\sin\frac{\pi}{6}+1\right)} & -\frac{1}{\sin\varphi\left(\sin\frac{\pi}{6}+1\right)} \\ \frac{-\tan\alpha\left(\sin\frac{\pi}{6}+1\right)-\cos\frac{\pi}{6}}{2\sin\varphi\left(\sin\frac{\pi}{6}+1\right)\cos\frac{\pi}{6}} & \frac{\tan\alpha\left(\sin\frac{\pi}{6}+1\right)-\cos\frac{\pi}{6}}{2\sin\varphi\left(\sin\frac{\pi}{6}+1\right)\cos\frac{\pi}{6}} & \frac{1}{\sin\varphi\left(\sin\frac{\pi}{6}+1\right)} \\ \frac{1}{2\cos\varphi\left(\sin\frac{\pi}{6}+1\right)} & \frac{1}{2\cos\varphi\left(\sin\frac{\pi}{6}+1\right)} & \frac{\sin\frac{\pi}{6}}{\cos\varphi\left(\sin\frac{\pi}{6}+1\right)} \end{bmatrix}, \quad \text{D.22.}$$

To eliminate the terms from the second column of the LHS matrix, we first divide row 1 and multiply row 2 by $\cos\alpha$, which after simplification gives

$$\begin{bmatrix}\tan\alpha & -1 & 0\\ 0 & 1 & 0\\ 0 & 0 & 1\end{bmatrix}\begin{bmatrix}\dfrac{1/\cos\alpha}{2\sin\varphi\left(\sin\frac{\pi}{6}+1\right)} & \dfrac{1/\cos\alpha}{2\sin\varphi\left(\sin\frac{\pi}{6}+1\right)} & -\dfrac{1/\cos\alpha}{\sin\varphi\left(\sin\frac{\pi}{6}+1\right)}\\ \dfrac{-\sin\alpha\left(\sin\frac{\pi}{6}+1\right)/\cos\frac{\pi}{6}-\cos\alpha}{2\sin\varphi\left(\sin\frac{\pi}{6}+1\right)} & \dfrac{\sin\alpha\left(\sin\frac{\pi}{6}+1\right)/\cos\frac{\pi}{6}-\cos\alpha}{2\sin\varphi\left(\sin\frac{\pi}{6}+1\right)} & \dfrac{\cos\alpha}{\sin\varphi\left(\sin\frac{\pi}{6}+1\right)}\\ \dfrac{1}{2\cos\varphi\left(\sin\frac{\pi}{6}+1\right)} & \dfrac{1}{2\cos\varphi\left(\sin\frac{\pi}{6}+1\right)} & \dfrac{\sin\frac{\pi}{6}}{\cos\varphi\left(\sin\frac{\pi}{6}+1\right)}\end{bmatrix}, \quad \text{D.23}$$

and then we add row 2 to row 1 to obtain

$$\begin{bmatrix}\tan\alpha & 0 & 0\\ 0 & 1 & 0\\ 0 & 0 & 1\end{bmatrix}\begin{bmatrix}\dfrac{1/\cos\alpha-\sin\alpha\left(\sin\frac{\pi}{6}+1\right)/\cos\frac{\pi}{6}-\cos\alpha}{2\sin\varphi\left(\sin\frac{\pi}{6}+1\right)} & \dfrac{1/\cos\alpha+\sin\alpha\left(\sin\frac{\pi}{6}+1\right)/\cos\frac{\pi}{6}-\cos\alpha}{2\sin\varphi\left(\sin\frac{\pi}{6}+1\right)} & \dfrac{\cos\alpha-1/\cos\alpha}{\sin\varphi\left(\sin\frac{\pi}{6}+1\right)}\\ \dfrac{-\sin\alpha\left(\sin\frac{\pi}{6}+1\right)/\cos\frac{\pi}{6}-\cos\alpha}{2\sin\varphi\left(\sin\frac{\pi}{6}+1\right)} & \dfrac{\sin\alpha\left(\sin\frac{\pi}{6}+1\right)/\cos\frac{\pi}{6}-\cos\alpha}{2\sin\varphi\left(\sin\frac{\pi}{6}+1\right)} & \dfrac{\cos\alpha}{\sin\varphi\left(\sin\frac{\pi}{6}+1\right)}\\ \dfrac{1}{2\cos\varphi\left(\sin\frac{\pi}{6}+1\right)} & \dfrac{1}{2\cos\varphi\left(\sin\frac{\pi}{6}+1\right)} & \dfrac{\sin\frac{\pi}{6}}{\cos\varphi\left(\sin\frac{\pi}{6}+1\right)}\end{bmatrix} \quad \text{D}$$

Finally, row 1 is divided by $\tan\alpha$. After simplifying the terms, the RHS matrix gives the inverse of the transformation matrix provided in **equation D.10**.

D.4: References

Lhermitte, R., & Serafin, R. (1984). Pulse-to-Pulse Coherent Doppler Sonar Signal Processing Techniques. *Journal of Atmospheric and Oceanic Technology, 1*(4), 293-308. doi: 10.1175/1520-0426(1984)001<0293:ptpcds>2.0.co;2

Miller, K., & Rochwarger, M. (1972). A covariance approach to spectral moment estimation. *IEEE Transactions on Information Theory, 18*(5), 588-596. doi: 10.1109/tit.1972.1054886

Pinkel, R. (1980). Acoustic Doppler Techniques. In F. Dobson, L. Hasse & R. Davis (Eds.), *Air-Sea Interaction* (pp. 171-199). USA: Springer.

Rennie, C. D., & Hay, A. (2010). Reynolds Stress Estimates in a Tidal Channel from Phase-Wrapped ADV Data. *Journal of Coastal Research, 26*(1), 157-166. doi: 10.2112/08-1090.1

Zedel, L., & Hay, A. E. (2002). A three-component bistatic coherent Doppler velocity profiler: Error sensitivity and system accuracy. *Ieee Journal of Oceanic Engineering, 27*(3), 717-725. doi: 10.1109/Joe.2002.1040953

Zedel, L., Hay, A. E., Cabrera, R., & Lohrmann, A. (1996). Performance of a single-beam pulse-to-pulse coherent Doppler profiler. *Ieee Journal of Oceanic Engineering, 21*(3), 290-297. doi: 10.1109/48.508159

APPENDIX E: GRAIN SIZE ANALYSIS

LS Particle Size Analyzer

31 Jan 2011 15:53

Beckman Coulter LS 13 320

File name:	F:\Donnees granulo\INRS\Labo\Bell-Mackenzie\530\bell-mackenzie_530_administra_ 9 Dec 2008_10-10_06 bell-mackenzie_530_administra_ 9 Dec 2008_10-10_06.$ls		
File ID:	bell-mackenzie		
Sample ID:	530		
Operator:	administrateur		
Run number:	6		
Comment 1:	INRS-ETE		
Comment 2:	Fred		
Optical model:	Fraunhofer.rf780f		
Residual:	0.72%		
LS 13 320	Dry Powder System		
Start time:	10:09 9 Dec 2008	Run length:	34 seconds
Average Vacuum:	14.3" H2O		
Obscuration:	7%		
Software:	5.03	Firmware:	2.02

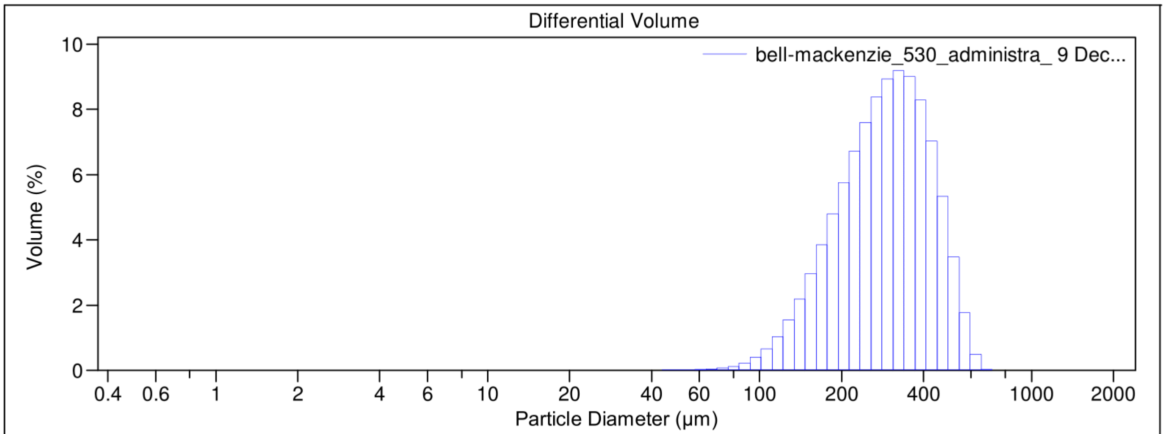

Volume Statistics (Arithmetic) bell-mackenzie_530_administra_ 9 Dec 2008_10-10_06.$ls

Calculations from 0.375 µm to 2000 µm

Volume:	100%		
Mean:	302.9 µm	S.D.:	111.6 µm
Median:	293.0 µm	Variance:	12464 μm^2
Mean/Median ratio:	1.034	C.V.:	36.9%
Mode:	324.4 µm	Skewness:	0.390 Right skewed
		Kurtosis:	-0.382 Platykurtic

<10%	<25%	<50%	<75%	<90%
163.7 µm	217.0 µm	293.0 µm	379.4 µm	458.8 µm

Figure E-1: Grain size analysis of the 330 µm sand.

LS Particle Size Analyzer

31 Jan 2011 15:53

Beckman Coulter LS 13 320

File name:	F:\Donnees granulo\INRS\Labo\Bell-Mackenzie\505\bell-mackenzie_505_administra_ 9 Dec 2008_10-08_05 bell-mackenzie_505_administra_ 9 Dec 2008_10-08_05.$ls		
File ID:	bell-mackenzie		
Sample ID:	505		
Operator:	administrateur		
Run number:	5		
Comment 1:	INRS-ETE		
Comment 2:	Fred		
Optical model:	Fraunhofer.rf780f		
Residual:	0.55%		
LS 13 320	Dry Powder System		
Start time:	10:08 9 Dec 2008	Run length:	48 seconds
Average Vacuum:	13.7" H2O		
Obscuration:	9%		
Software:	5.03	Firmware:	2.02

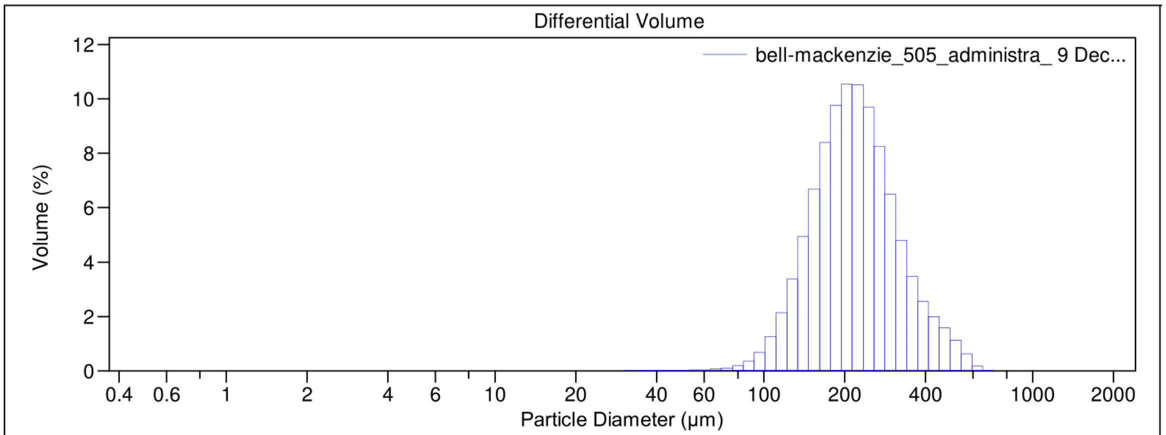

Volume Statistics (Arithmetic) bell-mackenzie_505_administra_ 9 Dec 2008_10-08_05.$ls

Calculations from 0.375 µm to 2000 µm

Volume:	100%		
Mean:	233.7 µm	S.D.:	90.90 µm
Median:	215.8 µm	Variance:	8263 $µm^2$
Mean/Median ratio:	1.083	C.V.:	38.9%
Mode:	203.5 µm	Skewness:	1.233 Right skewed
		Kurtosis:	1.903 Leptokurtic

<10%	<25%	<50%	<75%	<90%
138.1 µm	170.6 µm	215.8 µm	275.6 µm	354.8 µm

Figure E-2: Grain size analysis of the 230 µm sand.

LS Particle Size Analyzer

31 Jan 2011 15:54

Beckman Coulter LS 13 320

File name:	F:\Donnees granulo\INRS\Labo\Bell-Mackenzie\705\bell-mackenzie_705_administra_ 9 Dec 2008_10-06_04 bell-mackenzie_705_administra_ 9 Dec 2008_10-06_04.$ls		
File ID:	bell-mackenzie		
Sample ID:	705		
Operator:	administrateur		
Run number:	4		
Comment 1:	INRS-ETE		
Comment 2:	Fred		
Optical model:	Fraunhofer.rf780f		
Residual:	0.54%		
LS 13 320	Dry Powder System		
Start time:	10:05 9 Dec 2008	Run length:	60 seconds
Average Vacuum:	13.6" H2O		
Obscuration:	9%		
Software:	5.03	Firmware:	2.02

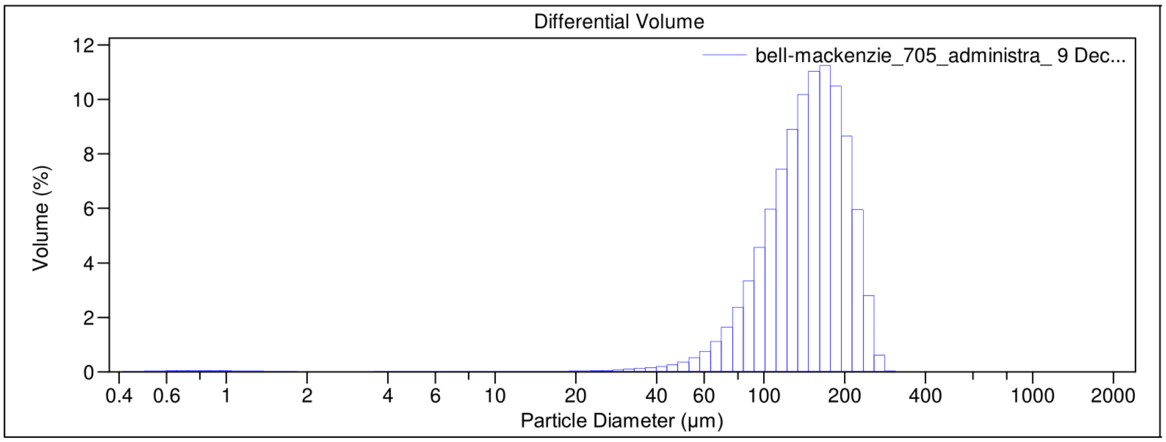

Volume Statistics (Arithmetic)		bell-mackenzie_705_administra_ 9 Dec 2008_10-06_04.$ls	
Calculations from 0.375 µm to 2000 µm			
Volume:	100%		
Mean:	148.0 µm	S.D.:	48.75 µm
Median:	147.8 µm	Variance:	2376 μm^2
Mean/Median ratio:	1.001	C.V.:	32.9%
Mode:	168.9 µm	Skewness:	-0.118 Left skewed
		Kurtosis:	-0.083 Platykurtic

<10%	<25%	<50%	<75%	<90%
86.82 µm	114.4 µm	147.8 µm	182.8 µm	211.9 µm

Figure E-3: Grain size analysis of the 150 µm sand.